BIOACTIVE, SELF-FITTING SCAFFOLDS PREPARED FROM SILOXANE-BASED SHAPE MEMORY POLYMERS

A Dissertation

by

FELIPE ORLANDO BELTRAN

Submitted to the Graduate and Professional School of
Texas A&M University
in partial fulfillment of the requirements for the degree of

DOCTOR OF PHILOSOPHY

Chair of Committee,	Melissa A. Grunlan
Co-Chair of Committee,	Patrick J. Shamberger
Committee Members,	Akhilesh K. Gaharwar
	W. Brian Saunders
Head of Department,	Ibrahim Karaman

December 2021

Major Subject: Materials Science and Engineering

ABSTRACT

Thermoresponsive shape memory polymer (SMP) scaffolds afford conformal “self-fitting” into irregularly shaped craniomaxillofacial (CMF) bone defects. Grunlan and co-workers previously reported SMP scaffolds based on biodegradable poly(ε-caprolactone) (diacrylate) (PCL-DA). Later, to enhance the rate of degradation, semi-interpenetrating network (semi-IPN) scaffolds were formed with PCL-DA and thermoplastic poly(L-lactic acid) (PLLA) (75:25 wt%, respectively). Bioactivity (i.e., the ability to induce the formation of a layer of hydroxyapatite, HAp), a property integral to promoting bone regeneration, was imparted by coating scaffolds with polydopamine (PD). However, as the scaffolds erode, the PD coating is lost as is bioactivity. Furthermore, the impact of ethylene oxide (EtO) sterilization on such PD-coated scaffolds was not assessed. Grunlan and co-workers have previously observed that hydrogels containing siloxane-based polymers were bioactive. While PCL-based scaffolds had been previously prepared with a siloxane-based co-macromer, the bioactivity was not assessed.

In the first study, PD-coated PCL-DA and PCL-DA/PLLA semi-IPN scaffolds were EtO sterilized. Morphological features, *in vitro* bioactivity, PCL crystallinity, PLLA crystallinity, and crosslinking were all preserved. Subsequently, shape memory properties, compressive moduli, and *in vitro* degradation behaviors were also unchanged.

In the second study, to achieve self-fitting scaffolds with innate bioactivity, PCL/polydimethylsiloxane (PDMS) co-matrices were formed with three types of macromers to systematically alter PMDS content and crosslink density. $\mathrm{PCL_{90}}$-DA was combined with a *linear*-$\mathrm{PDMS_{66}}$-dimethacrylate (DMA) macromer, and a *star*-$\mathrm{PDMS_{66}}$-tetramethacrylate (TMA) macromer at 90:10, 75:25, and 60:40 wt % ratios. Scaffolds were also prepared with an acrylated (AcO) triblock macromer (AcO-$\mathrm{PCL_{45}}$-*b*-$\mathrm{PDMS_{66}}$-*b*-$\mathrm{PCL_{45}}$-OAc) (65:35 wt % ratio). All

PCL/PDMS scaffolds displayed bioactivity *in vitro*, leading to significant increases in moduli. Furthermore, degradation rates increased with PDMS content.

Lastly, the impact of siloxane polymer hydrophobicity on the bioactivity of PCL-based scaffolds was investigated. Scaffolds were prepared by combining PCL_{90}-DA with either with linear macromers: $PDMS_{66}$-DMA or polymethylhydrosiloxane$_{66}$-dimethacrylate ($PMHS_{66}$-DMA) (90:10, 75:25, and 60:40 wt % ratios). These PMHS-containing scaffolds exhibited further increased degradation and mineralized in just two weeks. Scaffolds were also cultured with human mesenchymal stem cells (hMSCs) to assess osteoinductivity. Compared to PCL-DA scaffolds, both PCL-DA/PDMS-DMA and PCL-DA/PMHS-DMA scaffolds had increased cell viability and proliferation as well as expressed higher osteogenic protein markers.

DEDICATION

To My Parents and Grandmother

Your patience, guidance, and faith in me are the reasons I am here today. You have done more than I could ever ask for and provided an environment that I could learn and thrive in.

I say it often but truly, thank you. I love you.

ACKNOWLEDGEMENTS

I would first like to thank my committee chair, Prof. Melissa Grunlan. Although I had different academic background, Prof. Grunlan's confidence and leadership encouraged me to reach my goals. I am forever indebted to her for the support and guidance during this crucial phase in my career. I would also like to thank my co-chair, Prof. Patrick Shamberger and committee members, Prof. Akhilesh Gaharwar, and Prof. Brian Saunders for the time and support they have provided during my doctoral studies.

Thank you to the Department of Materials Science and Engineering, including friends, colleagues, faculty and staff. Within the Grunlan lab, I could not have achieved this without the friendship and support of Dr. Lindsay Woodard, Dr. Kristen Means, Dr. Jakkrit Suriboot, Dr. Bryan Ngo, Dr. Michael Frassica, Dr. Michaela Pfau, Dr. Ping Dong, Alec Marmo and Connor Demott. I owe a special thanks to the undergraduates who contributed greatly to this work including Chris Houk, Ashley Hicks, and Whitney Sloan.

Additionally, I must thank my family and friends. To my mom and dad, thank you for never giving up and allowing me to reach my dreams, I owe all I am to you. To my family including my step-father Bjorn, cousin Erik, and grandmother Abi, it would have been impossible to complete this without your constant encouragement. To my best friend Luis, your support and willingness to lend an ear has been invaluable to my success, you are truly my brother. To my pets, Tesla, Oak, and Luna your constant companionship has taught me lessons that I will cherish forever. Finally, Olivia, your love has been the fuel to drive me forward and I am so grateful for the sacrifices you have made for me. I am nervous but excited for the future and I can wait to get started.

CONTRIBUTORS AND FUNDING SOURCES

Contributors

This work was supervised by a dissertation committee consisting of Professor Melissa A. Grunlan [advisor] as well as Professor Patrick J. Shamberger of the Department of Materials Science and Engineering, Professor Akhilesh K. Gaharwar of the Department of Biomedical Engineering, and Professor W. Brian Saunders of the Department of Small Animal Clinical Sciences.

The use of the Microscopy and Imaging Center at Texas A&M University for SEM and SEM-EDS is acknowledged. All *in vitro* cell culture data was completed by the lab of Dr. Mariah Hahn of the Department of Biomedical Engineering at Rensselaer Polytechnic Institute, including Dr. Ahmad Arabiyat and Robert Culibrk. The use of BioRender software is acknowledged.

All other work for the dissertation was completed by the student, under advisement of Professor Melissa A. Grunlan of the Department of Biomedical Engineering.

Funding Sources

Graduate study was supported by the NSF Lewis Stokes Alliance for Minority Participation (LSAMP) and the OGAPS Pathways to Doctoral Fellowship from Texas A&M University. This work was made possible in part by the National Institute of Dental and Craniofacial Research (NIDCR) under 1R01DE025886-01A1 and the Texas A&M Engineering Experiment Station (TEES). Its contents are solely the responsibility of the authors and do not necessarily represent the views of the institutions.

TABLE OF CONTENTS

LIST OF FIGURES

LIST OF TABLES

1. BIOACTIVITY FOR BONE REPAIR: MATERIALS + METHODS

1.1. Overview

Bioactivity is a critical property in producing a successful bone regenerative device. Bioactive devices are capable of promoting mineralization of hydroxyapatite (HAp; $Ca_{10}(PO_4)_6(OH)_2$) on its surface when exposed to calcium and phosphate ionic rich environments such as human blood plasma. In turn, HAp formations have been acknowledged as key promoters in osteogenic differentiation (i.e osteoconductivity) as well as in material-bone bonding to surround tissue (i.e. osteointegration). Thus, any bone regenerative device that is not bioactive will suffer from negative outcomes in neotissue formation. While certain biomaterials used for bone devices are innately bioactive (e.g. bone grafts, decellularized bone matrices, bioceramics), new generations of polymeric biomaterials have a distinct lack in bioactivity. Fortunately, there are various methods to available to impart bioactivity on such polymeric devices. These techniques range from coatings, surface modifications, external additive (e.g. allografts fragments, bioceramics) composites, and most recently, forming co-matrices with bioactive siloxane polymers. Dependent on device application requirements, certain bioactive granting methodologies are more practical due to properties changes they may contribute. However, extensive research continues to bolster the available catalog of bioactivity granting techniques.

1.2. Introduction

As an important form of hard tissue in our body, bones are critical for mechanical stability, protection, hemopoieses, and storage of inorganic minerals.[1] While capable of impressive innate regeneration, bone struggles in repairing large, complex segmental defects (i.e. critically-sized). These defects are often the result of traumatic injury or surgical excision, while others are congenital in nature such as orofacial cleft (cleft palate). The demand for treatment options has led to bone being the second largest transplanted tissue with ~2 million transplants annually.[2] Research into the development of bone treatment devices have been the focus of numerous published works in the field of biomaterials and engineering. In contrast to replacement devices of the past (i.e. titanium fixation plates) newer generation of devices are regenerative in nature, facilitating in native neo-tissue formation. While there are substantial benefits, bone regeneration is an intricate, highly involved process and designing a material to promote healing is challenging.

In the past, bone-focused biomedical devices sought to replace damaged bone, known as bone substitutes. One such substitutes are metallic implants comprised of titanium or stainless steel.[3] These implants take the form of screws, bone plates, stability rods, or compression plates. Metallic implants are used in orthopedic replacements (hip or knee), vertebral fusion, and cranial fixation plates. Limitations of metallic implants often involve revisitation surgery due to implant failure. One common issue is that of aseptic loosening (~60-70%) resulting in a failure to integrate with surrounding tissue.[4] Additionally, in high movement (e.g. synovial joints) or load bearing (e.g. femoral rods) sites, wear particulate debris can lead to cytotoxicity and can stimulate adverse host response.[5] Furthermore, metallic implants often cite stress shielding leading to adjacent bone

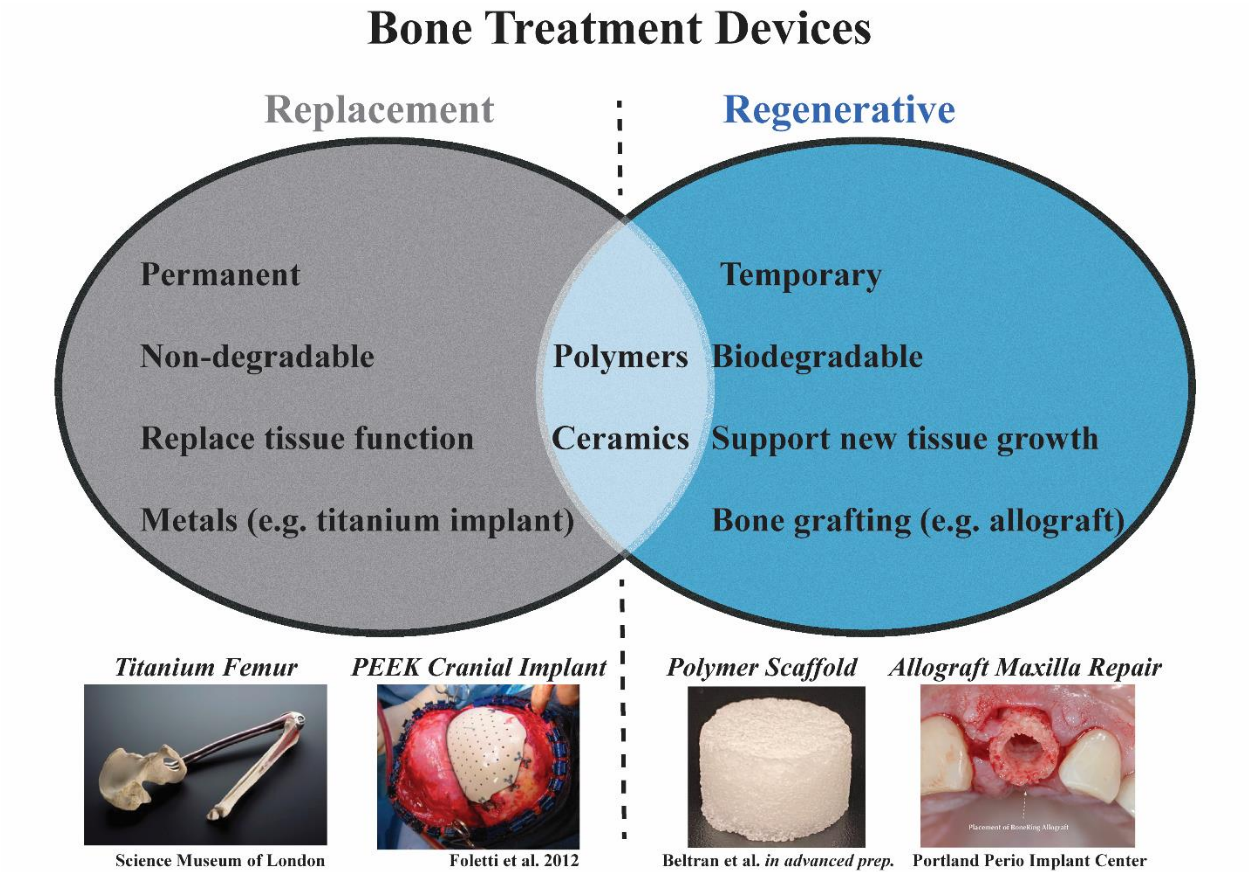

Figure 1-1. Bone treatment devices, replacement *versus* regenerative.

remodeling and osteopenia (reduction in bone density) as a primary concern.[6] Stress shielding may result from massive differences in compressive modulus between titanium (~50 GPa) or stainless steel (~51 GPa) to bone (~4 GPa cancellous; ~15 GPa cortical).[7] While having their limitations, metallic implants are suitable when patients cannot natively grow tissue whether due to age, massive defect size, or radiological damage, all of which are common in bone cancer patients.

Recent development into bone substitutes as produced polymer-based replacements such as polyether ether ketone (PEEK).[8] Due to an aromatic backbone, high levels of crystallinity (~35-45%)[9], and high thermal properties (melt transition temp. T_m ~345 ºC; glass transition temp. T_g

140 ºC)[10] PEEK has suitable mechanical properties (compressive modulus ~4 GPa)[7] making it an excellent replacement to bone. Furthermore, similarity in compressive modulus to bone reduces stress shielding effects. To date, PEEK has been used in various osseous replacement treatments for orthopedic, spinal,[11] dental,[12] and craniomaxillofacial.[8, 13, 14] Additionally, PEEK has reported lower failure rates than analogous titanium implants. However, the largest benefit of PEEK is ease of precise fabrication through CAD/CAM software, allowing for unique, complex device designs.[15, 16] This has led to 3D printed porous PEEK implants allowing for neotissue ingrowth into pores of implant, resulting in an integrative strategy.[17] While improving on metallic implants, PEEK is known to be expensive[18] and require high temperature printing (~400 ºC).[15, 16]

While bone substitutes are still relevant in today's medical field, recent advancements in biomedical engineering focus on regenerative treatments (**Figure 1-1**).[19] These therapeutic treatments function to drive healing of native osseous tissue through structural support, drug delivery, and may contain osteogenic agents. Such devices including tissue scaffolds[20] and hydrogels[2] have been developed utilizing both organic and synthetically-derived materials. Regenerative materials include natural and synthetic polymers, tissue grafts, and bioceramics. These devices, known as regenerative biomaterials, have been utilized for bone applications as well as other systems such as skin[21] and vascular grafting.[22] Ideal regenerative biomaterials should be biocompatible, non-cytotoxic, minimal immune response, and support new tissue formation. Furthermore, devices such as tissue scaffolds are porous, allowing cellular proliferation within the scaffold. Regenerative function additionally requires devices must also be biodegradable to support new tissue growth, with cytocompatible degradation products. Finally, in bone-focused devices, bioactivity must be present for bonding to adjacent osseous tissue and promoting new bone growth.[23]

1.3. Bioactivity

Bioactivity is defined as the ability to induce the formation of hydroxyapatite (HAp; $Ca_{10}(PO_4)_6(OH)_2$).[24-27] Thus, absence of bioactivity limits regenerative potential of bone regenerative devices. This is namely due to the role of HAp in promoting osteogenic differentiation (i.e osteoconductivity) as well as bonding to surround tissue (i.e. osteointegration).[28, 29] HAp is readily found in the extracellular matrix (ECM) of healthy bone tissue along with collagen (primarily type I), proteoglycans, and glycoproteins.[30-32] While composition of bone is location-dependent,[30] HAp plays a crucial role in its structural integrity. In particular, rigid HAp is responsible for providing bone's mechanical stability while collagen fibers aid in resisting tensile stresses. In physiological conditions, collagen fibers deposited in mesh-like formations within ECM, providing an environment in which HAp crystals nucleate through self-assembly.[33] These crystals are then incorporated further in bonding to existing bone or digested by bone cells for remodeling purposes. In response, HAp has been incorporated into various biomaterials[34-38] to improve osteoconductivity such as 3D printed HAp/poly(ε-caprolactone) (PCL) and HAp/poly(propylene fumarate) (PPF)[39] as well as HAp/poly(lactic-*co*-glycolic acid) (PLGA).[40] These investigations reported enhanced cell viability and proliferation as well as micro-computed tomography (CT)/histological data indicating substantial bone growth compared to non-HAp containing materials.[39, 40] Bioactive materials are capable of innately forming HAp when exposed to physiological fluid, rather than being fabricated with it. Due to its rigid nature, certain devices may lose functionality when HAp is incorporated rather than innately formed over time (i.e. shape memory tissue scaffolds). Furthermore, innately mineralizing devices bring the advantage of promoting HAp formation throughout its lifespan. This is suggested to enhance bioactive material's osteoconductivity, with greater bonding to adjacent bone tissue.

1.4. Bone: Composition and protein markers

While location specific, in general bone is comprised of both organic and non-organic mineral components with generic weight percentages of ~70% inorganic, ~25% organic, and ~5% water. As previously noted, the inorganic segments are mainly mineralized HAp with collagen type I and non-collagenous proteins making up organic components (~90% and ~10%, respectively). Furthermore, bone contains four distinct cell types: osteoclasts, osteoblasts, osteocytes, and bone lining cells (**Figure 1-2**, **Table 1-1**).[41, 42] Osteoclasts are large multinuclear

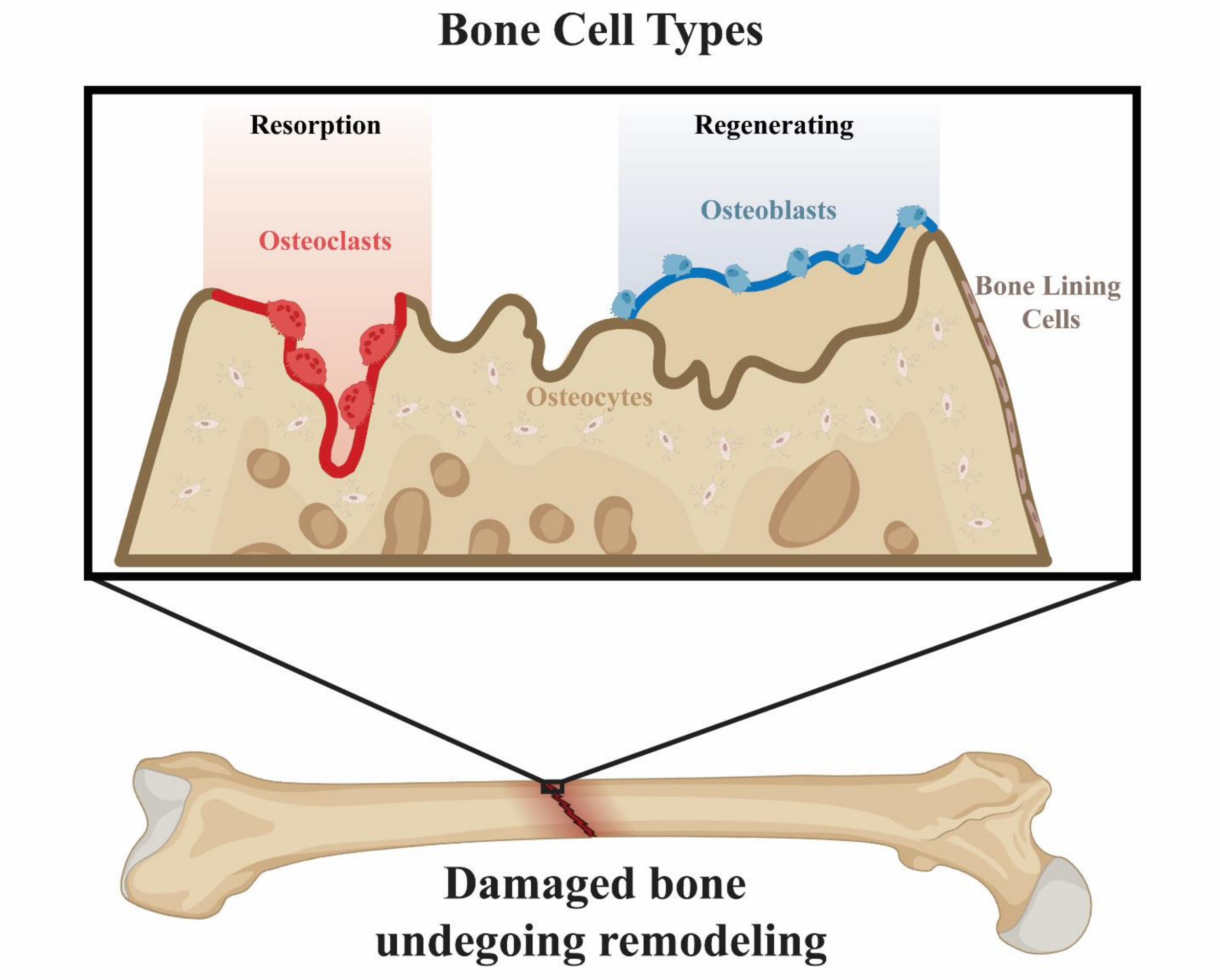

Figure 1-2. Types of bone cells and their roles during remodeling process after sustaining an injury.

cells whose main function is resorption of bone ECM during remodeling in response to signals from tissue damage or changes in mechanical stresses. These changes in stress may be resulting from failure of diseased bone or growth of new tissue. Resorption of ECM is done through acidic degradation of inorganic components and enzymatic digestion of organic components. Osteoblasts are cuboidal mononuclear cells whose primary function is synthesizing the organic components of the ECM. This includes collagen type I, proteoglycans, and other non-collagenous proteins. Bone remodeling involves osteoclast undergoing phagocytosis of both organic and inorganic components of ECM with osteoblasts forming new tissue (**Figure 1-2**). A coupling mechanism through protein signaling ensures that the amount of new bone laid down is equivalent to bone resorbed. Osteocytes are mature, post-proliferative osteoblasts entrapped within the ECM that play a role alongside osteoclasts in remodeling. They are the longest-lived and most prolific of the bone cells, comprising ~90% of all bone cells. Additionally, it has been reported that osteocytes sense mechanical stresses and release responsive growth factors in better instructing future remodeling. Bone lining cells are flattened, elongated cells lining the surface of bone ECM. Similarly to osteocytes, bone lining cells are mature osteoblasts whose main function is the protect the ECM from foreign agents and unnecessary osteocyte resorption.

In addition to cell types, key osteogenic protein markers are often testing for *in vitro* cellular analysis to confirm bioactive osteogenesis (**Table 1-1**).[43-49] Runx2, a transcription factor, is known to induce the differentiation of multipotent mesenchymal stem cells (MSCs) into osteoblasts. BMP4 is a prominent signaling protein form development of various organ systems and is reported to participate in osteoblastic differentiation. SPARC, also known as osteonectin (ON), are matricellular glycoproteins that functions as a signaling protein in bone remodeling as well as a regulator in malignant bone proliferation. COL1A1 is the major protein component of type I collagen. OPN, found in various bone cells, is reported to play role in regulating bone mass through proliferation, migration, and maintaining of osteoblasts/osteoclasts. VEGF is critical in angiogenesis, which for a highly vascular organ system as bone, is critical for the growth and sustainably of new tissue. RANKL signals osteoclast formation through environmental indicators such as diseased or damaged bone, thus aiding in bone resorption.

Table 1-1: Bone cells and osteogenic protein markers

Bone Cell Types	**Function**
Osteoclasts	Bone resorption, essential in remodeling damaged bone.[41]
Osteoblasts	Bone forming/repairing, key in laying down ECM.[41]
Osteocytes	Inactive osteoblasts within ECM.[41]
Bone lining cells	Inactive elongated, flattened osteoblasts lining surface of bone, showing little activity.[41, 42]
Osteogenic Protein Markers	**Function**
Runt-related transcription factor 2 (Runx2)	Essential for osteoblastic differentiation and skeletal morphogenesis.[45]
Bone morphogenetic protein 4 (BMP4)	Osteoblastic differentiation and bone forming.[49]
Secreted protein acidic and rich cystenine (SPARC)	Bone formation/remodeling and regulating metastasis.[46]
Collagen 1 alpha 1 (COL1A1)	Main collagenous protein in bone ECM.[48]
Osteopontin (OPN)	Bone metabolism and maintaining homeostais.[47]
Vascular endothelial growth factor (VEGF)	Vascular development and angiogenesis.[44]
Receptor activator of NF-κB ligand (RANKL)	Osteoclastic differentiation factor.[43]

1.5. Biomaterials for bone regeneration: Osteoinductive platforms

Bone-focused biomaterials can be divided into two broadly defined groups: 1) organically-derived and 2) synthetic.[50] Organically-derived biomaterials include bone grafts and demineralized bone matrix transplants. Due to their organic nature, these biomaterials represent ideal osteoinductive platforms but sourcing is often difficult and costly. Synthetic materials (i.e. bioceramics and polymers) have fewer issues in sourcing and have the advantage of tailored properties. This allows synthetic biomaterials to be customized to exact specifications of morphology, resorption rate, or mechanical requirements for unique bone defects. As mentioned, bioactivity plays a key role in osteoconductivity and osteointegration through mineralization of HAp. When designing a synthetic biomaterial for bone regeneration, in addition to tuning properties mentioned above, special attention should be given to bioactivity.

Bone grafting. The most prominent organically-derived biomaterials are bone grafts. Bone grafts are external bones transplanted into defect sites for purpose of stimulating healing. Grafts have an advantage over other biomaterials being osseous tissue and having similar properties (e.g. mechanical) and composition to surrounding tissue. This technique is regenerative, with grafts being used in remodeling as a source of inorganic (i.e. HAp) and organic (i.e. collagen) building blocks for osteoblastic bone forming.[51] The gold standard grafting material is autologous grafts or autografts.[29] Bone autografting is the process by which osseous donor tissue is harvested from one site (healthy) and transplanted to another site (afflicted) in the same patient. The benefits of autografting are ideal histocompatibility and superior osteoinductivity. However, autografting has limitations in regards to its harvesting process such as donor site morbidity, surgeries, limited supply of viable donor tissue, and increased risk of infection.[29] Furthermore, complications during implantation such as lack of conformally fitting rigid grafts into irregular defect sites has led to premature graft resorption.[52-56] Another common grafting technique is allografting or donor tissue from a separate donor patient.[29] Similarly to autografting, limitations arise of lack of fitting rigid grafts into defect with additional complications in locating suitable donors along with an increased risk of immune rejection. Popular donor bone tissue sites are tiba and iliac crest. Cancellous (i.e. trabecular) bone is the often-preferred auto/allografting material but cortical (i.e. compact) bone is commonly applied as small chips or in a graft/blood mixture for smaller, non-mechanically load bearing defect sites. Finally, clinicians report success with xenografting, grafting tissue from different species than the host. Species such as bovine[57, 58] or porcine[57, 59] are often used as donors. Advantages of xenografts are high donor availability and somewhat similar properties (e.g. mechanical, ECM composition) as host human bone. However, complications arise from risk of disease transmission, higher chance of host immune response, highly variable resorption rates, and reduction in osteoinductive properties due to strict manufacturing and processing requirements.[60]

Demineralized bone matrix. A form of allografting, demineralized bone matrices (DBMs) have branched into a unique form of organic biomaterial.[61] The first reported human-derived DBM was transplanted for a long bone and lumbar spine defect repair in 1965 by Dr. Marshall R. Urist.[62] Since then, DBMs have been utilized in regenerative applications for appendicular,[63] axial,[64] and craniofacial bone defects.[65] Since 1991,[66] DBMs have seen great success in the commercial space, with various products such as AlloFuse® (AlloSource®), Osteosponge® (XTANT Medical), and Grafton™ (Medtronic).[67] As opposed to rigid grafting, DBMs come in porous strips, gels, granules as well as injectable putties.[66] This allows DBMs to be injected into irregular defect sites that would be challenging for rigid grafts. Processing for DBM follows 1) harvesting bone from donor (similar to allografts) followed by 2) decalcification of ECM. Decalcification is predominantly conducted utilizing an acidic solution to strip ECM of nonorganic components (HAp).[61] This process leaves a bone matrix consisting of organic ECM (collagen type I and non-collagenous proteins) with minimal HAp remaining. Once transplanted into defect sites, DBMs function as organic component storage sites for osteoclasts and osteoblasts to use in remodeling as well as structural support.[61, 67] Additionally, osteoinductivity is enhanced through osteogenic protein factors that are remnant from original allograft or added prior to transplantation. Those factors added after are unique to product lines with osteogenic media or cell seeding methodologies being proprietary.[67] Limitations have been reported by loose DBM particles leaving wound site and entering unintended areas.[67] Furthermore, DBMs are not suitable for load bearing sites without supporting fixation structures.

Bioceramics. A gold standard synthetic bioactive material is the glass-ceramic Bioglass 45S5 (Bioglass®; GSK Health Partner) developed in the late 1960s by Dr. Larry L. Hench.[68] It was designed utilizing silica glass (45 wt% SiO_2) as a base materials with additives within glass structure. Additives (24.5 wt% CaO, 24.5wt% Na_2O, and 6.0 wt% P_2O_5) were included as they mimic naturally occurring minerals and have molecular proportions of calcium to phosphorus similar to HAp.[68] When exposed to an aqueous environment, the surface layer dissolves then recondenses as a silica/calcium/phosphorus rich gel layer. This -Si-O- rich environment produced mineralization of HAp, suspected by cation (e.g. Ca^{2+}) chelation by oxygen electron pairs, in the matter of hours.[69-71] Following, HAp induces osteoblast/clast differentiation, with the gel being used in mineral resorption and depositing of new bone.[68] Bioglass has been used in solid grafting and fabricated as porous scaffolds as well as granules to fill in bone segmental gaps.[72] However, low fracture resistance makes it less applicable in load-bearing areas. This limitation is further heightened when bioceramics are fabricated as porous scaffolds. As the first bioactive material, Bioglass shifted the direction of bone regeneration away from organic grafting and toward synthetic biomaterials. Since its discovery, other bioceramics (e.g. Monocalcium phosphate monohydrate and octacalicum phosphate) have been designed to produce higher bioactivity with modification to properties such as resorption rate and mechanical behavior.[73] Leveraging the effect of silicon ceramics, investigators have investigated nanosilicates with the ability to induce mineralization.[74] Nanosilicates demonstrated high cytocompatibility, as well as effective bioactivity to induce differentiation of hMSCs into osteogenic lineages in absence of growth factors.[75, 76] Furthermore, bioceramics have been incorporated with other biomaterials (e.g. polymers[77]) to combat low fracture resistance while increasing bioactivity.

Polymers. The discovery of the first fully synthetic polymer (Bakelite) by Leo Baekeland in 1907[78] heralded the "Age of Polymers" and changed the course of material science. Following in 1949, Sir Nicholas Harold developed intraocular lenses from synthetic poly(methyl methacrylate) (PMMA).[79] Since then, polymers have been widely used for biomedical applications. While polymers are classified as non-organically derived biomaterials, some biomedical polymers are naturally-occurring. Examples of synthetic polymers are polycaprolactone (PCL), poly(lactic acid) (PLA), poly (L-lactic acid) (PLLA), and polyethylene glycol (PEG), while natural polymers examples are chitosan, hyaluronan, and collagen.[80] An extensive catalog of polymers has contributed to wide application range (e.g. drug delivery,[81] tissue regeneration,[2] bone replacement[11-14]) for polymeric biomaterials. Furthermore, polymers have been fabricated into structures such as hydrogels, tissue scaffolds, injectables, and as composites with bioceramics.[77] While considerations for polymeric biomaterials are application based, general criteria include non-cytotoxicity, biocompatibility, and if relevant, have non-toxic degradation products. In terms of regenerative devices, biodegradable polymer tissue scaffolds have reported success in healing bone defects.[82] These scaffolds have the advantage in control over pore size and porosity (*via* fabrication technique) as well as mechanical, chemical, and degradative behaviors (*via* polymer composition). Scaffold fabrication techniques include 3D printing, solvent cast particulate leaching (SCPL), gas foaming, and electrospinning.[83] Common polymers seen in bone tissue scaffolds include PCL, PLA, PEG, and PPF.[83] Tissue scaffolds are designed to act as lattices for bone cell ingrowth (i.e. porous) while having relative resorption rates to promote new tissue growth. While a significant advancement in the field of regenerative bone treatment, polymeric tissue scaffolds tend to have limitations in lack of bioactivity. Thus, to achieve bioactivity, these materials must be modified further to induce HAp mineralization.

1.6. Methods for achieving bioactivity in polymeric biomaterials

As mentioned, bioactivity directly impacts the osteoconductivity and osteointegration of a material. Thus, great importance on achieving bioactivity is placed on regenerative bone devices. While organically-derived (i.e. grafts and DBMs) and select synthetic (i.e. bioceramics) biomaterials are natively bioactive, in general, polymeric biomaterials lack this functionality.

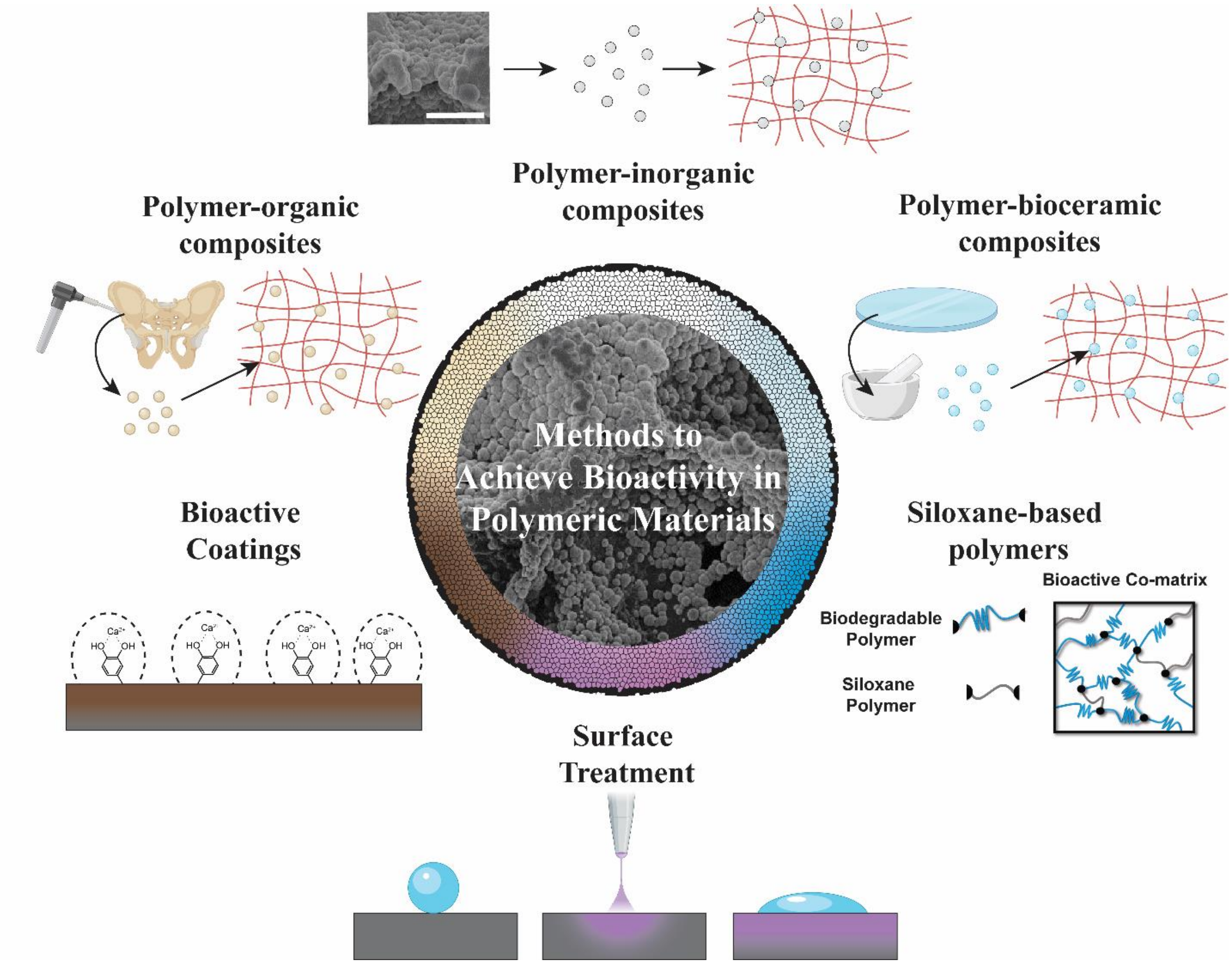

Figure 1-3. Methods to achieve bioactivity in polymeric biomaterials. Scale bar = 75 µm.

Thus, work to make these materials bioactive has investigated modifying polymers with external post-fabrication techniques (e.g. coatings, surface –treatment), as a composite material with other biomaterials (e.g. polymer-organic, polymer-inorganic, and polymer-bioceramics), and polymer network variations (**Figure 1-3**).

Bioactive coatings. To achieve bioactivity, certain polymeric devices have been coated with biologically inspired polydopamine (PD). Derived from ocean-dwelling mussels who can tightly adhere to both organic or inorganic substrates, researchers have designed dopamine coatings with similar functionality. Binding of PD coatings to surfaces achieved through oxidized dopamine polymerization under alkaline aqueous conditions.[84] PD coating has been applied to a wide range of substrates to improve wettability and reduce protein adhesion.[85] Furthermore, PD-coated materials have reported HAp mineralization when submerged in simulated body fluid (SBF). This is suggested to be a result of cationic metal chelation from ionic solution to polar catechol or amine functional groups from PD. The robust and bioactive nature of PD coatings has led to application on bone regenerative polymer devices such as PCL and PCL/PLLA tissue scaffolds. However, while tightly-adhering to surfaces, PD coatings have been reported to erode from surfaces over time. This is especially apparent in hydrolytically degradable bone tissue scaffolds where resorption is critical to regeneration. This further raises questions to the bioactive capabilities of PD coating over time.

Surface treatment. Another treatment that has been shown to grant bioactivity is surface modifying plasma treatment.[86] This technique utilizes an electric current passing through a gas (e.g. O_2, N_2) causing the gas to ionize. The highly volatile species within the plasma radiation then reacts and cleaves bonds on a material's surface.[87] This leads to surfaces with considerable amounts of polar functional groups, such as carbonyls and hydroxyls groups, as seen in work with

PMMA.[88] In turn, these polar groups increase surface wettability and chelate cations from surroundings leading to HAp nucleation. However, surface plasma treatment is known to be temporary, with surface restructuring reducing polar groups.[87] Thus, plasma treatment is limited by lack of long-term retention of bioactivity. Additionally to surface chemistry changes, plasma treatment causes physical changes by increasing surface roughness and area. Other techniques to increase surface roughness are sandblasting, acid etching, and micropatterning.[89] While surface roughness alone will not lead to mineralization in non-bioactive materials, it has been shown to increase HAp mineralization rate for those that are.[89, 90]

Polymer-organic composites. To enhance bioactivity, polymers have been modified by organically-derived materials to form polymer-organic composites. Due to the regenerative significance of grafting (i.e. auto, allo, and xeno), an effort to combine with polymeric materials was made to offset individual material limitations. One such investigation reported an injectable polyurethane (PU)/allograft composite as a bone fracture filler.[91] While injectable PU has been used to successfully produce tissue scaffolds, lack of bioactivity and degradability has limited utilization. Thus, allograft particles within the injection fluid was suspected to increase bioactivity and osteoconductivity. PU/allograft injectables were subjected to *in vivo* evaluations and found to have increased biodegradation. Furthermore, histological analysis showed enhanced cellular infiltration and new bone formation compared to solely PU scaffolds.[91] As suspected, rigid bone grafts amplified the mechanical modulus of PU scaffolds as well. In another study, a xenograft additive of bovine collagen type I was incorporated on PCL to form PCL/collagen scaffolds.[92] These scaffolds were seen to promote Runx2 and RANKL when compared to PCL control scaffolds. As collagen is the main component of the organic ECM, investigators had suspected such amplified levels of osteogenic protein express they observed. While a useful composite to promote bioactivity, certain grafting material (i.e. auto and allo) still have difficulty in sourcing, whereas xenografting still raises concerns of host immune response.

Polymer-inorganic composites. The relevance of forming HAp has been stated to be a key criterion in forming an osteoinductive platform for bone growth. While innately forming HAp (i.e. bioactivity) is the focus of many studies, other investigations incorporate HAp, or tricalcium phosphate (TCP), with polymers as polymer-inorganic composites to achieve bioactivity. As both HAp and TCP are natively found in bone (i.e. inorganic ECM components), they are excellent bioactive agents for inducing further HAp mineral nucleation, promoting differentiation of bone cells, and can be used as inorganic banks in bone remodeling.[93] However, by themselves they suffer from brittle mechanical properties. As a composite with polymers, benefits from both material types have led to successful bone regenerative devices. As a result, researchers have developed polymer tissue scaffolds with HAp or TCP embedded within such as the case of PLLA scaffolds with nanoparticles of HAp. The resulting composite maintained the processing tunability of PLLA scaffolds (e.g. control of porosity, pore size and morphology) with HAp granting bioactivty.[94, 95] In a separate study, PCL scaffolds coated with HAp expressed higher levels of ostegentic protein markers (i.e. Runx2 and RANKL) than non-coated versions.[92] Another investigation looks PLLA/TCP scaffolds and found that *in vivo* models observed increased new bone growth by volume when compared to PLLA only scaffolds.[96] Further advantages of polymer-inorganic composites stem from enhancements to biodegradation rates and mechanical behavior, based on polymer to inorganic content.[97] Both of these properties play a critical role in resorption/remodeling, stability, and osteogenic differentiation. However, development of polymer-inorganic composite materials is often limited by phase separation resulting from aggregation of inorganic components within the polymer.[97] Aggregated sections can lead to nonhomogenous mechanical, degradative, and bioactive distribution. This is issue becomes especially apparent in higher inorganic content composites.

Polymer-bioceramic composites. In a similar material category as polymer-inorganic composites, another approach utilizes inorganic bioceramics. As mentioned, siloxane-based bioceramics are a class of biomaterial that are highly bioactive, however difficulty in processing and high brittleness limits their application uses. Thus, an approach combining polymers and bioceramics has led to new field of biomaterial, polymer-bioceramic composites. Typically, bioceramics are incorporated as surface modifications or fillers in polymeric bone scaffolds. One example is that of PPF with Bioglass nanoparticles.[98] Such composite was reported to have substantially higher Runx2 and OCN protein expression *in vitro* after a 4 week timepoint than PPF control groups. Investigators cited Bioglass as the promoting osteogenic factor in these studies. As suspected, bioceramics increase the mechanical properties of combined polymer materials due to rigid nature, while polymer networks manage any imparted brittle behavior.[98, 99] Furthermore, due the bioceramics increased wettability and susceptibility to hydrolysis, polymer-bioceramic composites degrade at faster rates than other polymeric or polymer-composite biomaterials. Additionally, nanosilicates have been incorporated in poly(ethylene oxide terephthalate) (PEOT)/poly(butylene terephthalate) (PBT) (PEOT/PBT) and 3D printed into porous scaffolds. Results illustrated successful fabrication with enhancements to mechanical modulus. Another type of polymer-bioceramic composite are ceramic scaffolds coated by polymers. An example is on reports of Bioglass scaffolds coated by poly(3-bydroxybutyrate) (P3HB).[100] In such case, P3HB coating had a positive effect on compression strength of bioceramic scaffold, increased work required to fracture the material.[74] This report suggests that the bioactive behavior of bioceramics can be preserved with polymer coatings acting as a toughening agent.

Siloxane-based polymers. While coatings, surface modifications, and composites have been critical to granting bioactivity to polymeric biomaterials in the past, one recent study investigated the potential of modifying polymer networks with a bioactive polymer. Researchers were studying bone regenerative tissue scaffolds prepared from PCL-diacrylate (DA).[101, 102] These scaffolds were designed to address irregular shaped craniomaxillofacial (CMF) bone defects though shape memory property of cross-linked PCL networks. However, PCL-DA scaffolds were not bioactive, requiring PD coatings that were susceptible to erosion during degradation. Thus, a new method to achieve bioactivity was required to increase osteoconductive potential of the device. While exploring options in gaining bioactivity it was determined that plasma treatment would only temporarily grant bioactive capabilities. This is not ideal for "off-the-shelf" scaffolds that may be stored for unspecified timeframes and required to maintain functionality as to be used at a moment's notice. Polymer composites were also dismissed as rigidity imparted from bone fragments, HAp/TCP, or bioceramics would compromise shape memory function of PCL-DA scaffolds. However, inspiration was taken from bioceramics and by their -Si-O- content and its role in HAp mineralization. This led investigators to look at a medically relevant polymer with similar chemical composition, polydimethylsiloxane (PDMS). While utilization of PDMS as a bioactive agent is not well reported on, studies on ruptured silicone-containing breast implants[103] and intraocular lenses (IOLs)[104] have suggested silicones as the culprits behind unwanted HAp formation. Leveraging these results, investigators prepared PCL-DA/PDMS-dimethacrylate (DMA) co-matrix networked tissue scaffolds to evaluate possible bioactive response.[105] It was reported that scaffolds with PDMS exhibited HAp mineralization when submerged in 1X SBF after 4 weeks, opposed to non-mineralizing PCL-DA control groups. Furthermore, it was suggested by investigators that the hydrophobic nature of PDMS may reduce its bioactive capabilities. Once more, researchers looked for inspiration at past bioactive materials to see trends in high levels of wettability (i.e. hydrophilicity) among bioceramics whose mineralization times can range from hours to a few days.[68] Thus, to mimic these trends and further probe bioactive capacity of siloxane polymers, investigators combined PCL-DA with polyhydromethylsiloxane dimethacrylate (PMHS-DMA). It was believed that removal of a methyl pendant group would in turn reduce hydrophobicity and lead to faster rates of mineralization. As suspected, PCL-DA/PMHS-DMA scaffolds not only mineralized HAp, but it was reported that deposits formed at 2 weeks as opposed to 4 weeks in PCL-DA/PDMS-DMA groups. This work was a significant advancement for shape memory tissue scaffolds as all previous bioactive agents would limit shape memory function, while PDMS or PMHS reported no changes to scaffold function. Additionally, one further effect of siloxane polymers on PCL-DA scaffolds was increased rates of degradation, which was suggested to aid in scaffold resorption *in vivo*.[105] While discovering siloxane polymers impart bioactivity when cross-linked with PCL-DA, investigators also explored their effect on osteogenic potential *in vitro* (i.e. cellular) and *in vivo* (i.e. rat models). Cellular analysis of PCL-DA/PDMS-DMA and PCL-DA/PMHS-DMA scaffolds reported excellent cell viability, morphology, and proliferation. Furthermore, siloxane-containing scaffolds exhibited increases to osteogenic protein markers (i.e. BMP-4, OPN, VEGF, and RANKL) and mineralization staining (i.e. Alizarin Red S) when compared to PCL-DA controls with osteogenic enhancing medium. This led investigators to believe that siloxane polymers are excellent promoters to new bone growth. *In vivo* testing of PCL-DA/PDMS-DMA scaffolds were conducted in Wister rat models both in non-critically (i.e. 6 mm) and critically sized defects (i.e. 8 mm) for 4 and 12 weeks, respectively. In both cases, PDMS-containing scaffolds exhibited comparable bone growth (by volume and surface area) to an empty sham defect control indicative of non-hinderance to tissue regeneration. Following, mechanical push-out tests were conducted to assess osteointegration to adjacent bone. When compared to autografts, PDMS-containing groups exhibited increased max load for push-out indicating that siloxane scaffolds had higher intergradation than host-derived autografts. Results from *in vitro* and *in vivo* testing were significant as they suggest that siloxane scaffolds were capable bioactive and osteoinductive platforms for cranial bone repair. The discovery of bioactivity granted through siloxane polymers may lead to future methods to achieve bioactivity. As no single technique to grant bioactivity is appropriate for every situation, future research may produce a catalog of bioactive endowing methodologies suitable for specific bone regenerative device requirements.

1.7. Testing Methods

To assess bioactivity investigators have utilized acellular (i.e. SBF) and cellular (i.e. cell culture) i*n vitro* analysis. Following, mineralization deposits or osteogenic markers are analyzed to determine chemical composition and expression relativity, respectively.

Simulated body fluid. Developed by Dr. Tadashi Kokubo in 1991,[106] simulated body fluid (SBF) was created as an alternative to utilizing organically-derived fluids for bioactivity testing. This acellular, synthetic fluid was designed to have similar ion concentration (e.g. Mg^{2+}, Ca^{2+}, Na^+, and K^+) to that of human blood plasma (denoted as 1X). Additionally, pH of SBF is close to physiological conditions (~7.4) and should be utilized at body temperature (~36.5 ºC). Once prepared, biomaterials are immersed in SBF, allowed to mineralize, then removed to determine bioactivity. Kokubo first developed SBF to test bioactivity in bioceramics and since been recognized by the biomaterials community as useful tool in predicting bioactivity in other materials.[89] Certain studies have investigated utilizing SBF at different to normal (i.e. 1X) ion concentrations (i.e. 1.5X[107] and 10X[108]) as means of accelerating mineralization or predicting bioactive behavior in an environment with fluctuating ion stability. Once materials are removed from SBF they need to be future analyzed to characterize mineralization deposit.

Scanning electron microscopy. Scanning electron microscopy (SEM) has been widely used in material science to visualize material surfaces at magnifications higher than traditional microscopy techniques. SEM functions by producing an image as a result of interactions with a fired incident electron beam and a sample's surface.[109] In the field of bioactive materials, SEM has application in visualizing surface modifications (i.e. surface roughness) but is frequently used to search for HAp deposits.[105, 110, 111] However, for accurate identification of mineralization type, SEM should be operation in conjunction with energy-dispersive X-ray spectroscopy (EDS). SEM-EDS utilizes unique, element-specific characteristic X-rays to determine total elemental composition of a sample.[112] Briefly, an incident electron beam collides and ejects an electron in the inner (i.e. low energy) shell of an atom. This "electron hole" will then be filled by an electron from a higher energy with excess energy being release as an X-ray. As energy differences between two shells is unique for any atomic structure, EDS can accurately construct an elemental spectrum for a given material. As calcium phosphorous minerals are all similar in appearance, EDS is used to identify HAp by a Ca to P molar ratio of ~1.67.[111]

X-ray diffraction. Another tool used in HAp identification is X-ray diffraction analysis (XRD).[113-115] As HAp are crystalline, XRD can be used to identify correct mineral formation. XRD functions by irradiating a crystalline material with incident X-rays then measuring the scattering angles and intensities of exiting X-rays. From this data, XRD can determine if crystals are HAp due to unique diffraction signature.

Mineralization staining. Stanning for mineralization can be utilized to test for bioactivity after SBF or cell culture. Alizarin Red S ($C_{14}H_7NaO_7S$) is a sodium salt used as a staining agent to assess through mineralization through binding with calcium located within HAp.[116, 117] In the presence of calcium, Alizarin Red S will react and precipitate as an orange/red pigment. Thus, gross inspect combined with relative pigment intensity can help investigators determine bioactivity and its extent in a material. Another analytic staining procedure is Von Kossa staining.[118, 119] Utilizing a silver nitrate solution, Von Kossa staining replaces calcium ions bound to phosphates with silver ions. This will cause mineral deposits to be stained grey/black based on concentration of calcium-phosphate containing HAP. Similarly to Alizarin Red S, inspection and relative intensity can assist in quantifying bioactivity.

Osteogenic protein analysis. While bioactivity relates to a material's ability to mineralization HAp, cell culturing provides insight on differentiation pathways and cell-induced HAp formation. While methodology of cell culturing is highly dependent on testing parameters, majority of bone regenerative devices are seeded by bone marrow-derived mesenchymal stem cells (B-MSCs).[120] B-MSCs are pluripotent, signifying that they are capable of terminally differentiating into various bone cells (i.e. osteocytes, osteoblasts, and osteoclasts). After seeding B-MSCs on a material, they are cultured for a given timeframe and processed to determine osteogenic potential of the material. As previously discussed, key markers for osteogenesis are Runx2, BMP-4, SPARC, etc. To determine relative expression of these markers a technique known as Western Blotting (WB) assays are implemented.[121] WB generally function as such: a protein complex matrix is obtained from a cell culture, then gel electrophoresis to separates proteins with respect to molecular weight. The separated proteins are then transferred onto a membrane with protein blocking buffer (preventing non-specific binding) and probed using a primary antibody to detect an osteogenic protein of interest.

1.8. Conclusions

In summary, bioactivity is crucial in designing a bone regenerative device. For a device to be classified as bioactive, it must be able to mineralize hydroxyapatite (HAp) when subjected to an ionic environment (e.g. simulated body fluid, human blood plasma). In turn, bioactivity is acknowledged as a key promoter in cellular osteogenic differentiation and new bone growth. Among bone regenerative biomaterials, polymers often have the unique challenge in lack of innate bioactivity Herein, we have highlighted numerous approaches to grant bioactivity in polymeric devices. These methods include bioactive coatings, surface modifications, composites, and most recently, incorporation of siloxane polymers. While no one methodology is appropriate for all device requirements, further developments into these categories has produced a vast catalog of suitable techniques. Given the potential impact of bioactivity in producing successful regenerative devices, continued research into novel methodologies for the production of osteogenic platforms is a critical endeavor.

2. SUITABILITY OF ETO STERILIZATION FOR POLYDOPAMINE-COATED, SELF-FITTING BONE SCAFFOLDS

2.1. Overview

Irregularly shaped craniomaxillofacial (CMF) defects may be advantageously treated by “self-fitting” shape memory polymer (SMP) scaffolds, namely those prepared from poly(ε-caprolactone)diacrylate (PCL-DA) networks and PCL-DA/poly(L-lactic acid) (PLLA) (75:25 wt%) semi-interpenetrating polymer networks (semi-IPNs). In addition to achieving good scaffold-tissue contact, a polydopamine (PD) coating can be leveraged to enhance bioactivity for improved osseointegration. Sterilization with ethylene oxide (EtO) represents a logical choice due to its low operating temperature and humidity. Herein, for the first time, the impact of EtO sterilization on the material properties of PD-coated SMP scaffolds was systematically assessed. Morphological features (i.e., pore size and pore interconnectivity), and *in vitro* bioactivity were preserved as were PCL crystallinity, PLLA crystallinity, and crosslinking. These latter features led to sustained shape memory properties, and compressive modulus. EtO-sterilized, PD-coated scaffolds displayed similar *in vitro* degradation behaviors versus analogous non-sterilized scaffolds. This included maintenance of compression modulus following 28 days of exposure to non-accelerated degradation conditions.

∗ Reprinted with permission from “Suitability of EtO sterilization for polydopamine-coated, self-fitting bone scaffolds” by C.J., Beltran, F.O., and Grunlan, M.A., 2021. *Poly. Deg. Stab*, Copyright [2021] Elsevier Ltd.

2.2. Introduction

Craniomaxillofacial (CMF) defects present a challenge for surgical repair due to their typically irregular geometries. While autografting is currently the gold standard, difficulty in shaping rigid grafts may lead to insufficient contact with adjacent tissue and subsequent graft resorption.[53, 55, 56] Bone substitutes (e.g., cements and putties) display shrinkage during *in situ* cure, often with significant exotherms, thereby also compromising tissue contact. To address the critical need for conformal shaping in bone defect regeneration, we have reported thermosensitive shape memory polymer (SMP) scaffolds able to "self-fit" into irregularly shaped defects.[102, 122] These are based on biodegradable poly(ε-caprolactone) (diacrylate) (PCL-DA, M_n ~10k g mol^{-1}) wherein the netpoints are formed by crosslinks and the crystalline lamellae ($T_{m,PCL}$ or "T_{trans}" ~55 °C) serve as the switching segments. Self-fitting is achieved by briefly subjecting the scaffold to warm air or saline (~55 °C), inducing a malleable state that allows the scaffold to be press-fit into the defect.[101] The scaffold therein expands to the defect edges (via shape recovery) and subsequently returns to its original rigid state within the defect (via shape fixity). To promote osteogenesis and neotissue infiltration, such SMP scaffolds are readily prepared via solvent-casting particulate leaching (SCPL) to yield the desired pore size and excellent pore interconnectivity.[101, 102] Due to the slow degradation rate of PCL-DA,[123-126] semi-interpenetrating network (semi-IPN) SMP scaffolds were formed with PCL-DA and thermoplastic poly(L-lactic acid) (PLLA) (M_n ~10k g mol^{-1}) at 75:25 wt%.[127, 128] These semi-IPN scaffolds resulted in not only a marked increase in degradation rate, but also increased the compressive moduli (E) from ~13 MPa to ~21 MPa. In addition to the conformal fitting afforded by SMP scaffolds, bioactivity (i.e., the ability to induce the formation of a thin surface layer of carbonated hydroxyapatite, HAp)[24-26] would further promote osseointegration and bone regeneration. Readily formed as tens of nm thick coatings on a variety of substrates, polydopamine (PD) coatings are known to promote the formation of HAp both *in vitro* and *in vivo*.[129-135] Thus, PCL-DA and PCL-DA/PLLA SMP scaffolds were coated with polydopamine and displayed formation of HAp *in vitro* as well as increased osteoinductivity of seeded mesenchymal stem cells (MSCs).[102, 136]

Necessary for both *in vitro* (e.g., cell culture), *in vivo* studies, and ultimately, clinical use, the method of device sterilization must be carefully selected to avoid negatively impacting material properties.[137] In the case of the PD-coated SMP scaffolds, owing to the susceptibility of polyesters to hydrolytic degradation and a softening temperature of ~55 ºC (i.e., $T_{m,PCL}$), sterilization must be absent of humidity and significant heat ($T < 55$ ºC). Ethylene oxide (EtO) sterilization fulfills these requirements in addition to being reliable and cost-effective.[138] In contrast, γ-irradiation of polyesters has the potential produce an extensive decrease in molecular weight, substantially altering thermomechanical and degradation properties.[139-146] The use of UV-ozone sterilization is known to induce photo-oxidative cleavage of polyesters.[147] Reports on the use of EtO sterilization of polyesters generally demonstrate a lack of discernable impact on material properties.[148-151] However, some reports note some changes to morphology of porous or electrospun polyester scaffolds[152-158] as well as some instances of accelerated degradation rates.[148, 156] The surface hydrophobicity of PLLA and PCL were observed to slightly increase following EtO sterilization, attributed to the reaction of EtO with COOH or C-OH chain ends.[149, 159] However, while PD-coated materials have been subjected to EtO sterilization,[160] there is an absence of characterization of the impact on properties.

Herein, we sought to determine if EtO sterilization impacted the thermomechanical, degradation, and surface properties of PD-coated SMP scaffolds: PCL-DA (***Series A***) and semi-IPN PCL-DA/PLLA (75:25 wt%) (***Series B***) (**Figure 2-1**). To do so, each series were

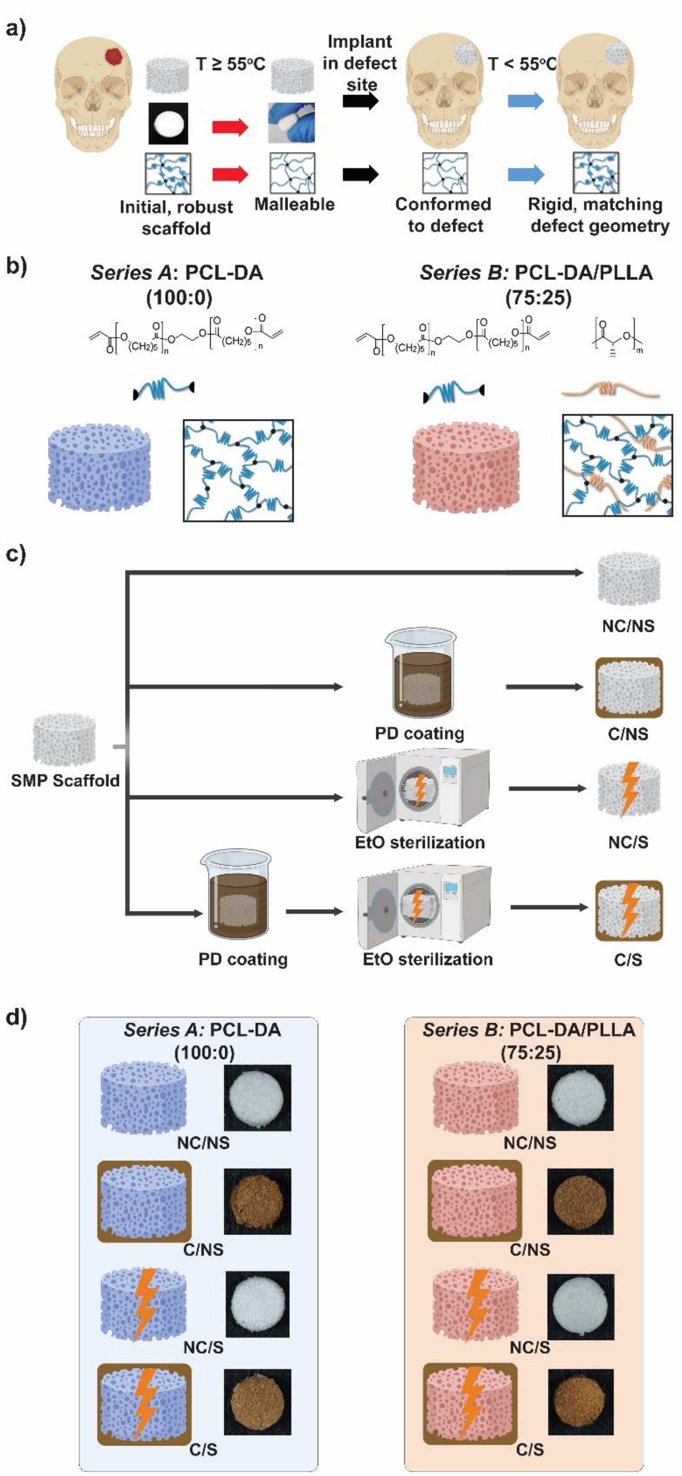

Figure 2-1. (a) Compositions of ***Series A*** (PCL-DA) and ***Series B*** (semi-IPN PLC-DA/PLLA, 75:25 wt %). (b) Self-fitting of SMP scaffolds in irregular bone defects. (c) Polydopamine (PD)-coating and/or EtO sterilization of series subgroups. (d) Four subgroups for each series: non-coated/non-sterilized (***NC/NS***), non-coated/sterilized (***NC/S***), coated/non-sterilized (***C/NS***), and coated/sterilized (***C/S***).

systematically separated into four subgroup categories: non-coated/non-sterilized (***NC/NS***), non-coated/EtO-sterilized (***NC/S***), PD-coated/non-sterilized (***C/NS***), and PD-coated/EtO-sterilized (***C/S***). EtO sterilization operating parameters of ~30-35 °C ($T < T_{m,PCL}$) and ~35% relative humidity (RH) were employed. The morphological, thermal, shape memory, mechanical, and degradation properties of scaffold subgroups were evaluated. Surface properties were also assessed to determine impact of EtO sterilization on the PD coating, namely surface wettability and bioactivity.

2.3. Materials and Methods

2.3.1. Materials

1-Vinyl-2-pyrrolidinone (NVP), 2,2-dimethoxy-2-phenylacetophenone (DMP), 4-dimethylaminopyridine (DMAP), acryloyl chloride, anhydrous magnesium sulfate ($MgSO_4$), calcium chloride ($CaCl_2$), dopamine hydrochloride, ethylene glycol, hydrochloric acid (HCl), L-lactide, magnesium chloride hexahydrate ($MgCl_2•6H_2O$), polycaprolactone diol (PCL-diol; M_n ~ 10k g/mol), potassium carbonate (K_2CO_3), potassium chloride (KCl), potassium phosphate dibasic trihydrate ($K_2HPO_4•3H_2O$), phosphate buffered saline (PBS), sodium bicarbonate ($NaHCO_3$), sodium chloride (NaCl), sodium hydroxide (NaOH), sodium sulfate (Na_2SO_4), stannous 2-ethylhexanoate, triethylamine (Et_3N), tris(hydroxymethyl)aminomethane (tris), and solvents were obtained from Sigma-Aldrich. Reagent-grade CH_2Cl_2 and NMR-grade $CDCl_3$ were dried over 4 Å molecular sieves prior to use.

2.3.2. Synthesis

All reactions were conducted in oven-dried (120 °C) glassware with Teflon covered magnetic stir bars to agitate reaction mixtures and under positive nitrogen (N_2) pressure. Chemical structures (including M_n) were confirmed with ^{1}H NMR spectroscopy (Inova 500 MHz spectrometer operating in the Fourier transform mode and a $CDCl_3$ standard). The purified polymer's thermal properties were characterized using differential scanning calorimetry (DSC, TA Instruments Q100) as described below.

PCL_{90}-DA was prepared as previously reported.[102, 105] Terminal hydroxyl groups of PCL-diol (M_n ~10k g/mol) were converted to photosensitive acrylate (OAc) groups by reacting with acryloyl chloride.[101] ^{1}H NMR and DSC analyses agreed with that previously reported: M_n ~10k g mol^{-1}; >90% acrylation; $T_{m,PCL}$ = ~53 °C; % crystallinity = ~48%. PLLA (M_n ~15k g mol^{-1}) was prepared per prior reports.[161] ^{1}H NMR and DSC analyses agreed with that previously reported: M_n ~15k g mol^{-1}; $T_{g,PLLA}$ = ~45 ºC; $T_{m,PLLA}$ = ~155 °C; % crystallinity = ~50%.

2.3.3. SMP Scaffold Fabrication

Porous scaffolds were fabricated using solvent-casting particulate leaching (SCPL).[102, 162] Fused salt templates, to achieve scaffold pore interconnectivity, were prepared in 20 mL scintillation vials (*I.D.* = 25 mm) with sieved NaCl (10.0 g, 460 ± 70 µm) and 7.5 wt.% deionized (DI) water. The mixture was stirred with a spatula, packed with a blunt glass rod, sealed vials centrifuged (15 min, 3220 *x g*), opened vials air-dried (~1 hr), and lastly dried *in vacuo* (room temperature, RT; overnight, ON; 30 in. Hg). Macromer solutions were prepared by dissolving PCL-DA (***Series A***) or PCL-DA and PLLA (75:25 wt%) (***Series B***) in DCM (0.15 g total per mL DCM). The photoinitiator solution (10 wt% DMP in NVP) was added at 15 vol%. After vortexing, ~5 mL of a macromer solution was added to each fused salt template (contained within the vial), sealed vials centrifuged (10 min, 1260 *x g*), opened vials exposed to UV light for ~3 mins (UV-Transilluminator, 6 mW cm^{-2}, 365 nm), and then air-dried ON. The salt template was extracted by soaking open vials in a water:ethanol solution (1:1 vol:vol) for 5 days, removing the scaffold from the vial after 2 days, with daily solution changes. The resulting cylindrical scaffolds were air-dried ON followed by drying *in vacuo* (RT, 4 hr, 30 in. Hg).

For both ***Series A*** and ***Series B***, specimens were designated for each subgroups: non-coated/non-sterilized (***NC/NS***), coated/non-sterilized (***C/NS***), non-coated/sterilized (***NC/S***), and coated/sterilized (***C/S***) (**Figure 2-1**). For "non-coated" (***NC***) scaffolds, the above cylindrical specimens (*d* ~12 mm) were heat treated (~180 °C, 15 min, 30 in. Hg), allowed to cool, biopsy punched (Integra Miltex) to *d* ~6 mm, and lastly horizontally sliced into 2 mm thick discs (Vibratome, Leica VT1000 S), discarding top and bottom sections (~2 mm). In the case of "coated" (***C***) specimens, coating with polydopamine was achieved similar to prior reports.[102, 136] Cylindrical scaffolds were heat treated (~180 °C, 15 min, 30 in. Hg), cooled, and sliced into 2 mm discs (*d* ~12 mm x *t* ~ 2 mm). Discs were then degassed with a syringe to allow the solution with the pore surfaces. Next, discs were submerged for 16 hr in a dopamine hydrochloride solution (2 mg mL^{-1} in 10 mM tris buffer; pH = 9.5) with continued motion atop a shaker table (150 rpm) for oxygenation. The coated scaffolds were subsequently placed in a Büchner funnel, thoroughly rinsed with DI water, dried *in vacuo* (RT, ON, 30 in. Hg), and then punched to 6 mm. For all non-coated and coated scaffolds, final specimen dimensions were *d* ~6 mm x *t* ~2 mm.

2.3.4. SMP Film Fabrication

Macromer precursor solutions were likewise prepared to fabricate equivalent films to evaluate surface wettability and sol content. Vortexed solutions were pipetted into circular silicone molds (*l* ~45 mm x *w* ~22 mm x *t* ~2 mm; McMaster Carr) secured via binder clips between glass slides. The solvent-swollen films were removed from the molds, air dried ON, dried *in vacuo* (RT, 4 hr, 30 in. Hg), submerged in a water/ethanol (1:1 vol:vol) mixture (3 hr), and then air-dried ON. Both ***Series A*** and ***Series B*** specimens were also designated for each subgroups (i.e., ***NC/NS***,

C/NS, ***NC/S***, and ***C/S***). For "non-coated" (***NC***) film specimens were heat treated (~180 °C, 15 min, 30 in. Hg), allowed to cool, and biopsy punched (Integra Miltex) to 6 mm. Final film specimen dimensions were *d* ~6 mm x *t* ~ 1.1 mm. In the case of "coated" (***C***) film specimens, coating with polydopamine was achieved similar to prior reports.[102] Films were heat treated (~180 °C, 15 min, 30 in. Hg), and allowed to cool to RT. Specimens were then submerged for 16 hr in a dopamine hydrochloride solution (2 mg mL^{-1} in 10 mM tris buffer, pH = 9.5, 150 rpm), thoroughly rinsed with DI water, dried *in vacuo* (RT, ON, 30 in. Hg), and then punched to ~6 mm. For all uncoated and coated films, final specimen dimensions were *d* ~6 mm x *t* ~1.1 mm.

2.3.5. EtO Sterilization

"Sterilized" (***S***) scaffold and film specimens (i.e., ***NC/S*** and ***C/S***) were subjected to EtO sterilization (Anderson, Anprolene® AN74i/x). Per manufacturer specifications, the unit operates at temperatures of ~30-35 °C and ~35% relative humidity (RH) (Humidichip®). Specimens (5-10 discs) were placed into a single peel self-seal sterilization pouch (Medline Industries, *l* ~90 mm x *w* ~230 mm) along with an EtO exposure indicator strip (Steris®; VerifyTM Laminated EO Integrator). The pouch was then placed into a sterilization liner bag. To the liner bag was added a glass ampoule of liquid EtO (encased in a gas release bag) and 2-3 biological indicator strips (Steritest® Biological Control). Next, the liner bag was vacuum purged inside the sterilizer compartment. After completing a purge cycle, the glass ampoule was manually broken and the sterilization cycle was set for 24 hr. At the end of the cycle, specimens were removed from the liner bag, and biological indicator strips were used to confirm the samples were effectively sterilized. Specimens were maintained at RT in the peel pack until testing.

2.3.6. SMP Scaffold and Film Characterization

Pore Size. Scaffold pore interconnectivity and pore size were evaluated by scanning election microscopy (SEM, JEOL JCM 5000 Neoscope, accelerating voltage B10 kV). Scaffold cross-sections were coating by Au-Pt (~4 nm). Images (N = 4) were analyzed using analysis software (Image J). Measurements (N = 30) were taken across various pores along a diagonal midline to determine average pore size.

T_m and %crystallinity. For SMP scaffolds, T_m and % crystallinity values were determined by DSC. Specimens (~15 mg, N = 3) were sealed in hermetic pans and heated from RT to 200 °C at a rate of 5 °C min^{-1}. Values were taken from a second DSC cycle to remove any thermal history. T_m was determined from the maximum point of the endothermic melt peak, and enthalpy change (ΔH_m) was calculated from the peak area (TA Universal Analysis software). Percent crystallinity was determined by equation (1):

$$\%\,\chi_c = \frac{\Delta H_m - \Delta H_c}{\Delta H_m^0 * w} * \ 100 \tag{1}$$

Where, ΔH_c is the enthalpy of crystallization from the exothermic cold crystallization peak and $\Delta H°_m$ as the enthalpy of fusion of theoretical 100% crystalline PCL (139.5 J g^{-1})[163] or PLLA (93.0 J g^{-1}),[164] and w the mass fraction of the corresponding polymer (e.g., w = 0.75 for PCL or 0.25 for PLLA in the case of semi-IPN scaffolds).

Shape fixity and recovery. Dynamic mechanical analysis (DMA, TA Instruments Q800) was used to quantitatively assess shape recovery (R_r) and shape fixity (R_f) over two cycles (C). Scaffold specimens (N = 3) were subjected to the following protocol: (1) Following equilibration at 60 °C for 5 min, compress to maximum strain (ε_m = 50%) at a rate of 50% min^{-1}, (2) hold at ε_m for 5 min, and then cool to 25 °C to fix the temporary shape, (3) remove the load, and immediately measure the ultimate strain (ε_u), (4) reheat to 60 °C to recover the permanent shape, measure the recovered strain (ε_p), and start the next cycle. The first cycle (C = 0) is referred to as the "pre-cycle" and is followed by C = 1. After shape recovery (C = 0), the specimen was cooled to RT and the new dimensions of the pre-cycled specimen was recorded and used for the subsequent cycle (C = 1). R_f and R_r for the first (C = 0) and second (C = 1) cycles were calculated using equations (2) and (3):

$$R_f(C) = \frac{\varepsilon_u(C)}{\varepsilon_m} \tag{2}$$

$$R_r(C) = \frac{\varepsilon_m - \varepsilon_p(C)}{\varepsilon_m - \varepsilon_p(C-1)} \tag{3}$$

$\varepsilon_u(C)$ is the ultimate strain in the stress-free state. ε_m is the maximum compressive strain (50%). $\varepsilon_p(C\text{-}1)$ and $\varepsilon_p(C)$ are the final strains of the specimens after two consecutive cycles in the stress-free state during the shape-recovery process. For the pre-cycle (C = 0), $\varepsilon_p(-1)$ equals "zero".

Compressive modulus. Scaffold specimens (N = 8 per time point and condition) underwent static compression testing (Instron 5944) at RT. Specimens were testing without subjecting to degradation (i.e., t = 0) as well as at t = 28 days following exposure to non-accelerated degradation conditions (described below). Prior to testing, degraded specimens were thoroughly rinse with DI water and dried *in vacuo* (RT, ON, 30 in. Hg). Specimens were subjected to constant strain (1.5 mm min^{-1}) up to 85% strain. No "t = 0" specimen fractured during testing. Compressive modulus (E) was calculated from the initial linear region of the stress-strain curve (≤ 10% ε).

Sol content. Film specimens (N = 3) were weighed and each submerged in 10 mL of CH_2Cl_2 within a 20 mL scintillation vial. Sealed vials were placed atop a shaker table (48 hr, 150 rpm) and subsequently rinsed with CH_2Cl_2, air dried ON, dried *in vacuo* (RT, 4 hr, 30 in. Hg), and weighed. The initial and final weights of film specimens were used to determine the % sol content.

Surface wettability. Surface wettability of films was characterized with static water contact angle (θ_{static}) measurements using a goniometer (CAM-200, KSV Instruments) equipped with an autodispenser, video camera, and drop-shape analysis software (Attention Theta). A sessile DI water droplet (5 µL) was applied to a film and θ_{static} measured at 2 min. The reported θ_{static} values are an average and standard deviation of three measurements made on different regions of the same film.

Bioactivity. Simulated body fluid (SBF, 1X) was prepared as described by Kokubo.[165] Scaffold specimens ($N = 6$ per time point) were immersed 20 mL SBF within a scintillation vial and maintained in a water bath at 37 °C for 14 days. Specimens were removed, thorough rinsed with DI water, and dried *in vacuo* (RT, 12 hr, 30 in. Hg). Cross-section specimens were prepared by sectioning with a stainless-steel blade and sputtered coated with Au-Pt (~4 nm). Scanning electron microscopy (SEM, JEOL JCM-5000 Neoscope, accelerating voltage of 10 kV) was used to visualize HAp formation.

Accelerated degradation. Scaffold degradation studies were performed under base-catalyzed conditions (0.2 M NaOH) per ASTM F1635. Scaffold specimens ($N = 3$ per time point) were weighed (W_i), and each submerged in 10 mL of the basic solution in a sealed scintillation vial maintained in an incubator (VWR Benchtop Shaking Incubator Model 1570) at 37 °C and 60 rpm. Specimens were removed at each of the four designated time points (24, 72, 120, and 168 hr), thoroughly rinsed with DI water, blotted, dried *in vacuo* (RT, ON, 30 in. Hg), and final specimen dry weight (W_d) recorded. Percent mass remaining was determined by equation (4):

$$\%\, Mass\ remaining = \frac{W_d}{W_i} * 100 \qquad \textbf{(4)}$$

Non-accelerated degradation and water uptake. Degradation studies were likewise performed as above but under neutral (i.e., non-accelerated) conditions in PBS (pH = 7.4) at a 28 day time point. In addition to calculating % mass remaining (equation 4), "% water uptake" was also determined as follows. Scaffold specimens (N = 3) were initially weighed (W_i) and then immersed 20 mL of PBS in sealed scintillation vials maintained in an incubator (37 °C, 60 rpm). At 28 days, the specimen was removed from the solution and weighed (W_w) (i.e., without blotting or drying). Specimens were subsequently dried *in vacuo* ON (RT; 30 in. Hg) and immediately weighed (W_d). Percent water uptake (i.e., % water within wet scaffold by mass) was calculated using equation (5):

$$\%\, Water\ uptake\ = \frac{W_w - W_d}{W_w} * 100 \tag{5}$$

2.3.7. Statistical Analyses

All results are presented as mean ± standard deviation calculated using GraphPad. Sample means were compared using ANOVA followed by Tukey's post-hoc test where $p < 0.05$ was considered statistically significant.

2.4. Results and Discussion

To assess the potential impact of EtO sterilization on PD-coated SMP scaffolds, both PCL-DA (***Series A***) and PCL-DA/PLLA semi-IPN (***Series B***) were prepared as 4 subgroups: non-coated/non-sterilized (***NC/NS***), non-coated/EtO-sterilized (***NC/S***), PD-coated/non-sterilized (***C/NS***), and PD-coated/EtO-sterilized (***C/S***) (**Figure 2-1**). As SMP scaffolds having a T_{trans} (i.e., $T_{m,PCL}$) of ~55 ºC and comprised of polyesters susceptible to hydrolysis, the EtO sterilization operating parameters of ~30-35 °C and ~35% RH were hypothesized to preserve morphological, thermal, shape memory, mechanical, and degradation properties. Surface wettability and

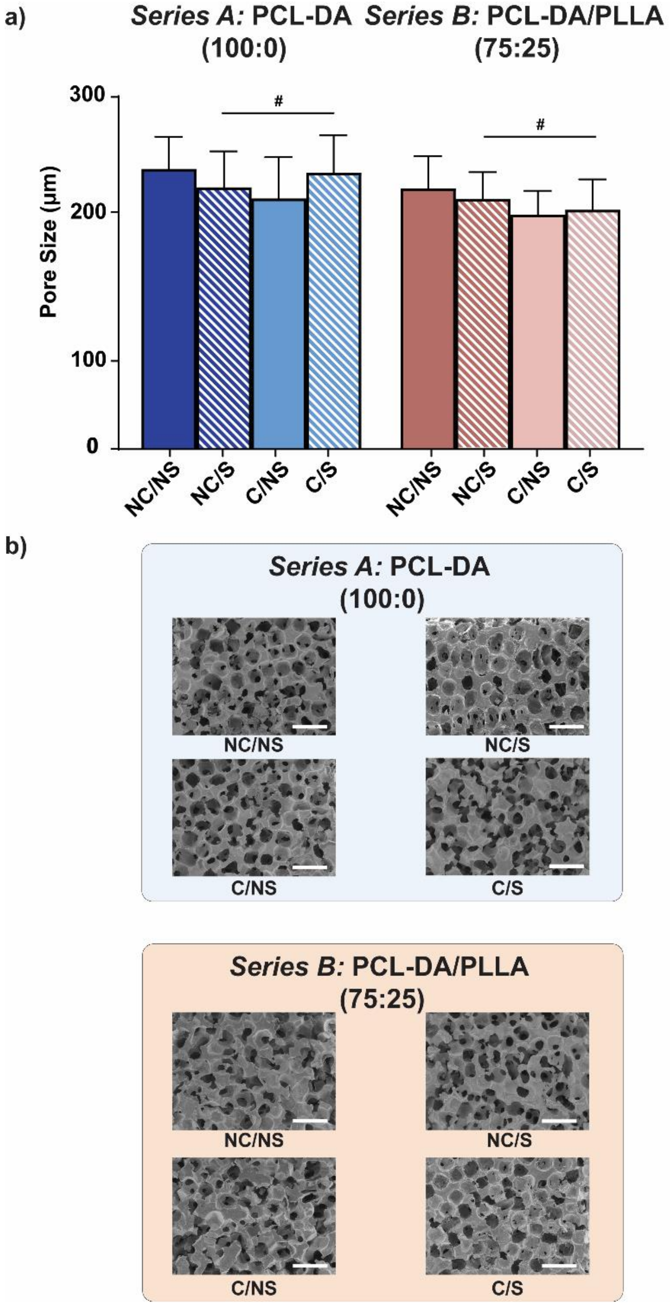

Figure 2-2. (a) Average pore sizes for scaffolds. (b) SEM images of scaffolds. Scale bars = 500 µm. #$p > 0.05$.

bioactivity were also assessed to determine impact of EtO sterilization on PD-coated scaffolds. Prior to sterilization, coated scaffolds (***C/NS***), exhibited the characteristic brown color associated with PD coatings.[130] Following sterilization, no observable change in the coloration of coated scaffolds (***C/S***) was observed (**Figure 2-1**).

2.4.1. Morphology

SMP scaffolds were readily prepared with SCPL, wherein sieved salt size establishes targeted average pore size and the fused salt template yields interconnected pores. These features are paramount to bone regeneration in terms of osteogenesis and neotissue infiltration, respectively.[25-27] The average pore size of EtO sterilized PD-coated scaffolds (***C/S***) remained unchanged versus other scaffolds (**Figure 2-2**, **Table A-1**). SEM imaging also confirm maintenance of scaffold pore interconnectivity following EtO sterilization.

2.4.2. PCL T_m, % crystallinity, and shape memory behavior

The "self-fitting" ability of the SMP scaffolds is based on the shape memory character of PCL, stemming from the crystalline lamellae ("switching segments", T_m ~55 ºC) that permits thermal softening and expansion (i.e., shape recovery) within an irregular defect. Loss of PCL

Table 2-1: Scaffold shape fixity (R_f) and shape recovery (R_r) of cycles 0 (i.e., pre-cycle) & 1.

	Cycle 0		**Cycle 1**	
***Series A* (100:0)**	R_{f1}	R_{r1}	R_{f2}	R_{r2}
NC/NS	99.3 ± 1.7	71.0 ± 4.0	100.4 ± 0.7	100.2 ± 0.4
NC/S	99.4 ± 0.5	88.4 ± 12.5	99.6 ± 0.3	99.6 ± 0.3
C/NS	100.8 ± 0.7	99.0 ± 3.5	100.3 ± 1.0	100.3 ± 1.0
C/S	99.9 ± 0.8	90.8 ± 5.8	100.1 ± 0.6	100.1 ± 0.6
***Series B* (75:25)**	R_{f1}	R_{r1}	R_{f2}	R_{r2}
NC/NS	100.7 ± 0.6	84.0 ± 15.6	99.7 ± 0.6	99.8 ± 0.4
NC/S	104.8 ± 5.3	81.4 ± 4.0	100.3 ± 0.5	99.2 ± 0.6
C/NS	100.3 ± 0.5	92.8 ± 3.3	100.3 ± 0.5	99.7 ± 0.3
C/S	100.6 ± 0.5	95.7 ± .0	100.3 ± 0.6	99.5 ± 0.0

crystallinity would compromise the self-fitting behavior of these scaffolds as well as alter mechanical and degradation properties. For both PCL-DA (***Series A***) and PCL-DA/PLLA semi-IPN (***Series B***), PD-coated scaffolds sterilized by EtO (***C/S***) showed no significant change in PCL % crystallinity (~43%) and $T_{m,PCL}$ (~55 ºC) (**Table A-2**). Both shape fixity (R_f) (i.e., the ability of the scaffold to retain a temporary shape when $T < T_{trans}$) and shape recovery (R_r) (i.e., the ability of the scaffold to return to its original shape when $T > T_{trans}$) were quantified over two cycles (**Table 2-1**). Attributed to the preserved PCL crystallinity, PD-coated scaffolds sterilized by EtO (***C/S***) displayed similarly high values (~100%, $C = 1$) of R_f and R_r compared to non-coated (***NC***) and non-sterilized (***NS***) scaffolds. Scaffolds showed an increase in R_r values from the first ($C = 0$) to the second cycle ($C = 1$).[166-168] This is consistent with our reports and of others, and attributed to the first shape memory cycle (i.e., pre-cycle) removing residual strain imparted by fabrication, thereby improving subsequent shape recovery.[102, 162]

2.4.3. Compressive Modulus

A reduction in SMP scaffold rigidity following EtO sterilization may lead to a reduction in structural support during bone regeneration. This would be expected with a loss of crystallinity and/or crosslinking PCL-DA. As noted above, PCL crystallinity was maintained for EtO-sterilized, PD-coated scaffolds (***C/S***). Additionally, for ***Series B***, PLLA % crystallinity (~35%) and $T_{m,PLLA}$ (~162 ºC) were maintained (**Table A-2**). Following sterilization, there was also no increase in sol content, indicating that PCL-DA crosslinks were not disrupted (**Table A-3**). As expected, compressive modulus (E) values of scaffolds were maintained (~12-15 MPa ***Series A*** groups, and

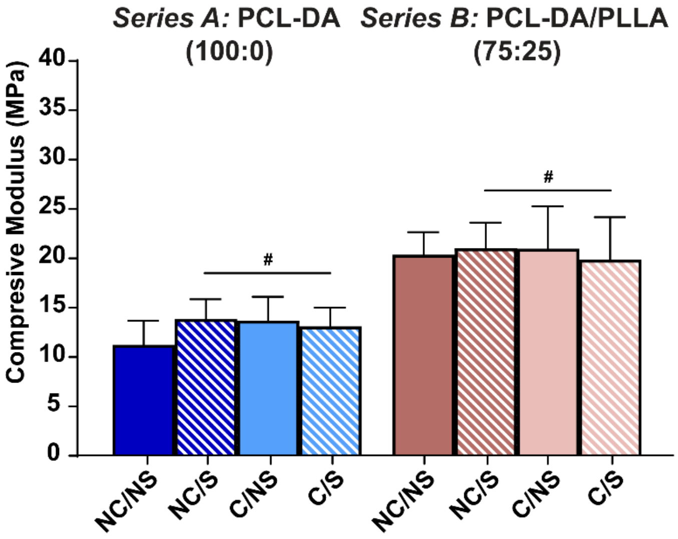

Figure 2-3. Compressive modulus (E) values for scaffolds. #$p > 0.05$ versus corresponding ***NC/NS***.

~20-23 MPa for ***Series B*** groups) regardless of PD-coating or sterilization (**Figure 2-3, Table A-4, Figure A-1**).

2.4.4. Surface wettability and bioactivity

PD coatings contain catechol and amine groups that increase surface hydrophilicity as well as induce the formation of HAp.[169-172] Essential to their osseointegration and regenerative capacity, EtO sterilization must not substantially alter the surface properties of PD-coated SMP scaffolds. Prior to sterilization, PD-coated scaffolds (***C/NS***) expectedly exhibited substantially greater hydrophilicity (i.e., lower θ_{static} values) versus the corresponding non-coated scaffolds (***NC/NS***). For ***Series A***, following EtO sterilization, non-coated (***NC/S***) as well as PD-coated scaffolds (***C/S***) exhibited somewhat greater hydrophobicity (i.e., higher θ_{static} values) versus corresponding non-sterilized scaffolds (***NC/NS*** and ***C/NS***, respectively) (**Figure 2-4, Table A-5**). This slight increase in surface hydrophobicity is consistent with prior reports.[149, 159] However, for ***Series B***, a

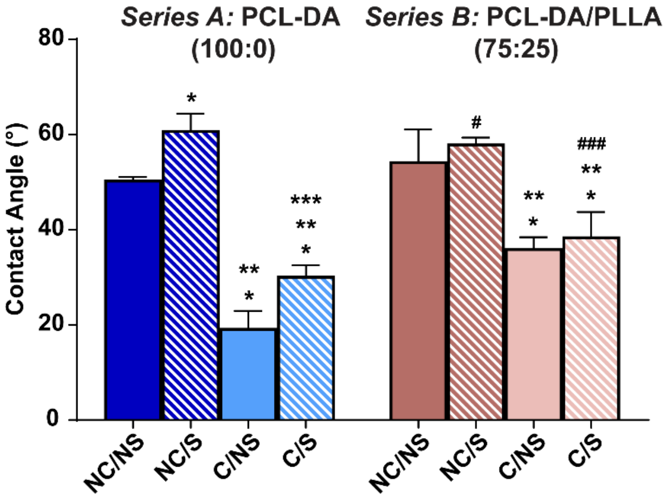

Figure 2-4. θ_{static} of SMP films. *$p < 0.05$ vs corresponding ***NC/NS***, **$p < 0.05$ vs corresponding ***NC/S***, ***$p < 0.05$ vs corresponding ***C/NS***, ###$p > 0.05$ vs corresponding ***C/NS***.

statistically significant increase in surface hydrophobicity was not observed for sterilized scaffolds (***NC/S*** and ***C/S***) versus non-sterilized scaffolds (***NC/NS*** and ***C/NS***, respectively).

The maximize bone regeneration and integration, retention of the bioactivity associated the PD coating must be retained following EtO sterilization of coated scaffolds. Bioactivity was assessed by evaluating the formation of HAp following immersion of PD-coated scaffolds in SBF (1X, 14 days) on SEM images of cross-sections (**Figure A-2**). For both ***Series A*** and ***B***, EtO-sterilized PD-coated scaffolds (***C/S***) retained the ability to mineralize.

2.4.5. Degradation and water uptake

Following EtO sterilization, the degradation behavior PD-coated scaffolds must not be significantly altered in order to yield expected resorption rates and associated changes in mechanical integrity. Degradation behavior was first evaluated under accelerated (basic) conditions (**Figure 2-5a**). Differences in mass remaining was closely evaluated at the final time point (168 hr) (**Figure 2-5b** and **c**, **Table A-6**). Expectedly, due to the known phase separation effects for the semi-IPNs,[128, 162, 173] ***Series A*** scaffolds degraded more slowly versus ***Series B*** scaffolds. While PD-coated scaffolds were more hydrophilic than corresponding non-coated scaffolds (**Figure 2-4, Table A-5**), coated scaffolds degraded somewhat more slowly. This may be attributed to the PD coating acting as barrier to water infiltration and subsequent polyester bond hydrolysis. For non-coated scaffolds, no differences were observed for EtO sterilized (***NC/NS***)

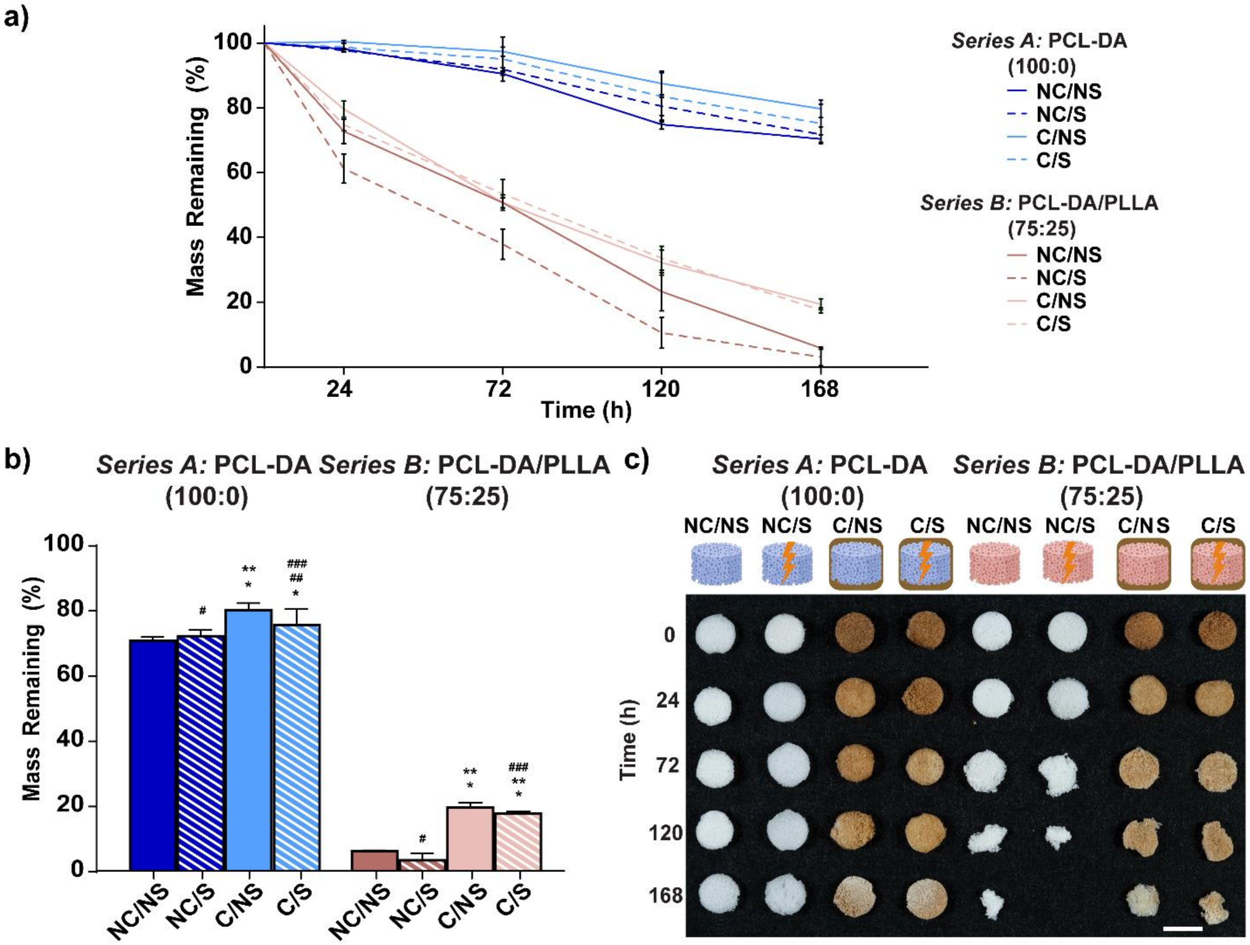

Figure 2-5. (a) % Mass remaining under accelerated conditions (0.2 M NaOH, 37 ºC, 60 rpm) over a period of 168 hr, (b) % mass remaining at 168 hr, and (c) photo-series of scaffold specimens at 168 hr. Scale bar = 1 cm. $*p < 0.05$ vs corresponding ***NC/NS***, $**p < 0.05$ vs corresponding ***NC/S***, #$p > 0.05$ vs corresponding ***NC/NS***, ##$p > 0.05$ vs corresponding ***NC/S***, and ###$p > 0.05$ vs corresponding ***C/NS***.

versus non-sterilized (***NC/NS***) specimens. An absence of change was likewise observed for sterilized PD-coated scaffolds (***C/S***) versus non-sterilized (***C/NS***) scaffolds.

Base-catalyzed conditions, while affording more rapid screening of degradation behavior, is known to impact degradation kinetics of polyesters.[174] Thus, degradation behavior was also evaluated using pH neutral conditions (PBS). After 28 days, minimal mass loss was expectedly observed (< ~3%), with no differences in mass remaining among specimens, including for EtO-sterilized, PD-coated scaffolds (***C/S***) (**Figure A-3**, **Table A-7**). Water uptake may be used to probe hydrolytic degradation trends when mass loss is minimal.[127] After 28 days, no significant differences in water uptake was observed among ***Series B*** scaffolds (**Figure A-4**, **Table A-8**). For ***Series A***, PD-coated scaffolds demonstrated greater % water uptake versus non-coated scaffolds; this may be attributed to the greater hydrophilicity of coated scaffolds. However, for ***Series A***, EtO-sterilized PD-coated scaffolds (***C/S***) did not change water uptake versus the non-sterilized PD-coated scaffold (***C/NS***). As another potential indicator of change to degradation behavior, the compressive modulus (E) of scaffolds was also assessed at this 28 day time point (**Figure A-5**, **Table A-9**). For ***Series A***, no significant changes in E were observed among all scaffolds. In the case of ***Series B***, EtO-sterilized PD-coated scaffolds (***C/S***) also exhibited no change in E versus non-sterilized PD-coated scaffold (***C/NS***). In total, the results from degradation studies point to significant change in the degradation behavior of EtO-sterilized PD-coated scaffolds (***C/S***).

2.5. Conclusions

Based on their ability to conformally fit into irregular defects and their bioactivity, PD-coated SMP scaffolds based on PCL-DA networks and PCL-DA/PLLA (75:25 wt%) semi-IPNs have unique potential to treat CMF bone defects. The impact of EtO sterilization of PD-coated scaffolds on integral scaffold properties was assessed. PCL-DA (***Series A***) and PCL-DA/PLLA semi-IPN (***Series B***) scaffolds were prepared as 4 subgroups: non-coated/non-sterilized (***NC/NS***), non-coated/EtO-sterilized (***NC/S***), PD-coated/non-sterilized (***C/NS***), and PD-coated/EtO-sterilized (***C/S***). For all scaffolds, no change to morphology (i.e., pore interconnectivity and pore size) was observed. This can be attributed to the low operating temperature (~30-35 °C) of the EtO sterilization that is lower than that of the $T_{m,PCL}$ (~55 ºC). PCL crystallinity was also maintained for all scaffolds, resulting in retention of shape memory behavior. For each series, the compressive modulus was also retained, and was linked to a lack of change to PCL crystallinity, PLLA crystallinity (***Series B***), and acrylate crosslinking (as indicated by sol content measurements). Following EtO sterilization, for ***Series A***, PD-coated specimens (***C/S***) were slightly more hydrophobic, but remained appreciably more hydrophilic versus non-coated, sterilized specimens (***NC/S***). In the case of ***Series B***, no changes in surface hydrophilicity were observed. Thus, the known effect of EtO sterilization increasing hydrophobicity were overall rather minor for these SMPs. Moreover, following sterilization, coated scaffolds (***C/S***) likewise mineralized when exposed to SBF (1X). Given the low humidity (35% RH) of the employed EtO sterilization, changes to scaffold degradation behavior were not expected. Under basic (accelerate conditions), at the final time point of 168 hr for a given series, similar mass remaining was observed for sterilized PD-coated scaffolds (***C/S***) versus prior to sterilization (***C/NS***). Similar mass loss among scaffolds of a given series was likewise under non-accelerated conditions for 28 days. Furthermore, under these conditions, similar water uptake as well as compressive modulus values was observed for sterilized PD-coated scaffolds (***C/S***) versus those prior to sterilization (***C/NS***). In total, this work establishes the suitability of EtO sterilization of PD-coated SMP scaffolds prepared from polyesters. Retention of key properties points to maintenance of their ability to promote self-fitting behavior, neotissue infiltration, bioactivity, rigidity, and degradation behavior following sterilization.

3. BIOACTIVE SILOXANE-CONTAINING SHAPE MEMORY POLYMER (SMP) SCAFFOLDS WITH TUNABLE DEGRADATION RATES

3.1. Overview

A materials-guided, regenerative approach to heal cranial defects requires a scaffold that cannot only achieve conformal fit into irregular geometries but also has bioactivity and suitable resorption rates. We have previously reported "self-fitting" shape memory polymer (SMP) scaffolds based on poly(ε-caprolactone) diacrylate (PCL-DA) that shape recover to fill irregular defect geometries. However, PCL-DA scaffolds lack innate bioactivity and degrade very slowly. Polydimethylsiloxane (PDMS) has been shown to impart innate bioactivity and to modify degradation rates when combined with organic crosslinked networks. Thus, this work reports the introduction of PDMS segments to form PCL/PDMS SMP scaffolds. These were prepared as co-matrices with three types of macromers to systematically alter PDMS content and crosslink density. Specifically, PCL_{90}-DA was combined with *linear*-$PDMS_{66}$-dimethacrylate (DMA) or 4-armed *star*-$PDMS_{66}$-tetramethacrylate (TMA) macromers at 90:10, 75:25, and 60:40 wt % ratios. Additionally, a triblock macromer (AcO-PCL_{45}-*b*-$PDMS_{66}$-*b*-PCL_{45}-OAc), having a 65:35 wt% ratio PCL:PDMS, was used. Scaffolds exhibited pore interconnectivity and uniform pore sizes and further maintained excellent shape memory behavior. Degradation rates increased with PDMS content and reduced crosslink density, with phase separation contributing to this effect. Irrespective of PDMS content, all PCL/PDMS scaffolds exhibited the formation of carbonated hydroxyapatite (HAp) following exposure to to simulated body fluid (SBF). While inclusion of

---

∗ Reprinted with permission from "Bioactive Siloxane-containing Shape-memory Polymer (SMP) Scaffolds with Tunable Degradation Rates" by Beltran, F.O., Houk, C.J., and Grunlan, M.A., 2021. *ACS Biomater. Sci. Eng.*, 7, 4, 1631-1639 Copyright [2021] by American Chemical Society.

PDMS expectedly reduced scaffold modulus and strength, mineralization increased these properties and, in some cases, to values exceeding or similar to the PCL-DA which did not mineralize.

3.2. Introduction

Craniomaxillofacial (CMF) bone defects present a unique challenge for repair due to irregular geometries. While autografting remains the gold standard, difficulty shaping and positioning the rigid graft frequently leads to a lack of good contact to adjacent tissue and subsequent graft resorption.[52-56] Regenerative engineering is a promising approach, but requires a scaffold that could readily achieve a conformal fit within irregular defects. *In situ* forming synthetic scaffolds suffer from brittle mechanical properties, inadequate porosity, exothermic cures, and post-cure shrinkage leading to poor tissue contact.[175-177] Shape memory polymers (SMPs) have received attention for their use in a variety of medical device applications.[178-181] We have previously proposed thermoresponsive shape memory polymers (SMPs) as self-fitting scaffolds for the repair of irregular bone defects.[102] Based on biodegradable poly(ε-caprolactone)diacrylate (PCL-DA), the crystalline lamellae (T_m or "T_{trans}" ~55 °C) serve as the switching segments while the netpoints are formed by crosslinks. Upon exposure to warm air or saline (~55 °C), the porous PCL-DA scaffolds become malleable such that they can be press-fit into irregular geometries, with shape recovery driving its expansion to fill the defect and shape fixity locking it into its new shape. Fabrication with a fused salt template produced SMP scaffolds with pore sizes in the range known to promote osteogenesis (~200 to ~350 μm) and pore interconnectivity necessary for neotissue infiltration.[182-184] Moreover, increased rates of biodegradation and mechanical strength were achieved with semi-interpenetrating network (semi-IPN) designs based on PCL-DA and thermoplastic poly(L-lactic acid) (PLLA).[127, 128] In a material-guided approach to regeneration, scaffold properties alone (i.e. without exogenous growth factors) elicit bone formation. Thus, the scaffold should also be bioactive, inducing the formation of a carbonated hydroxyapatite (HAp) at the surface for bonding to adjacent bone.[25, 26, 185] In this regard, the lack of innate bioactivity of PCL-DA and PCL-DA/PLLA SMP scaffolds limits their regenerative potential. Thus, a tens of nm-thick bioactive polydopamine coating was applied to PCL-DA scaffolds and shown to promote mineralization as well as mesenchymal stem cell (MSC) osteogenesis.[102, 186] However, application of the polydopamine coating requires additional fabrication steps and the coating is largely lost as the scaffold begins to erode. Thus, an approach that would render innate bioactivity throughout PCL-based SMP scaffolds would improve the regenerative potential.

Materials-driven approaches to confer bioactivity have generally relied on inorganic, hydrophobic silicon- and calcium phosphate-containing fillers (e.g. bioglasses, nanosilicates, β-tricalcium phosphates, and HAp).[187-191] However, incorporation of such fillers into the SMP scaffold would confer undesirable brittleness and may compromise shape memory behavior. Previously, we demonstrated that polydimethylsiloxane methacrylate (PDMS-MA) – a hydrophobic, silicon-based polymer – imparted bioactivity when incorporated into poly(ethylene glycol) diacrylate (PEG-DA) hydrogel scaffolds.[192-195] The low glass transition temperature (T_g ~ -120 ° C) of PDMS avoided the conferment of brittleness. In another study, SMP scaffolds were formed from acrylated triblock macromers, AcO-PCL$_n$-*b*-PDMS$_m$-*b*-PCL$_n$-OAc (m = 20, 37, 66, or 130 and n = 40).[196] These scaffolds degraded more quickly with increasing PDMS content (and faster than the PCL-DA control), but the accompanied higher pore size prohibited a conclusive correlation. Based on prior work with PCL-DA/PLLA scaffolds, the origin of accelerated degradation is hypothesized to be phase separation that facilitates water uptake.[128, 173] However, neither phase separation nor bioactivity was explored in the aforementioned report. Based on the prior studies, we hypothesized that PCL/PDMS scaffolds would exhibit bioactivity and accelerated degradation in a PDMS dose-dependent fashion.

Herein, towards enhancing the regenerative capacity of self-fitting SMP scaffolds, PDMS was incorporated to form PCL/PDMS co-matrix scaffolds to yield innate bioactivity and accelerated degradation rates. A series of PCL/PDMS scaffolds were prepared with siloxane macromers of varying PDMS architecture (to vary crosslink density) and PDMS content **(Figure 3-1)**. PCL$_{90}$-DA was systematically combined with either *linear*-PDMS$_{66}$-dimethacrylate (DMA) or 4-armed *star*-PDMS$_{66}$-tetramethacrylate (TMA) macromers at 90:10, 75:25, and 60:40 wt %

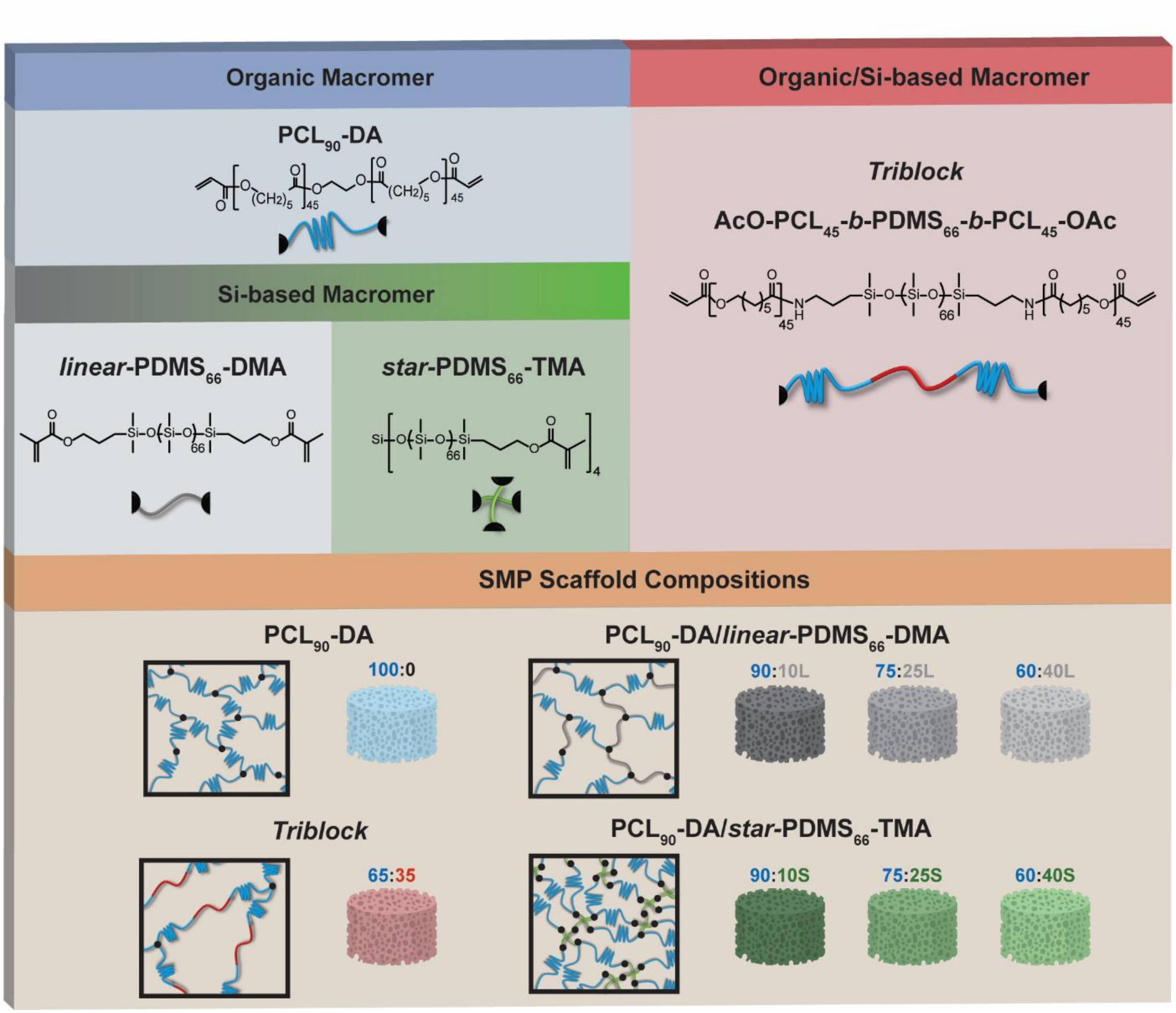

Figure 3-1. Macromers used to form self-fitting SMP scaffolds with varying wt % ratios of PCL to PDMS. Schematics are generalized representations of crosslinked network.

ratios. Additionally, a triblock macromer (AcO-PCL_{45}-*b*-$PDMS_{66}$-*b*-PCL_{45}-OAc), having a 65:35 wt% ratio PCL:PDMS, was also used. A PCL-DA scaffold (100:0 wt%) served as a control. Scaffolds were prepared using a solvent-casting, particulate leaching (SPCL) protocol[102, 128] to produce similar pore sizes as well as pore interconnectivity. Scaffolds were characterized in terms of calculated molecular weight between crosslinks (M_c), pore size, PCL crystallinity, shape memory behavior, and compressive mechanical properties as well as *in vitro* degradation (accelerated and non-accelerated conditions) and bioactivity. Bioactivity was assessed by exposure to 1X simulated body fluid (SBF).[165] The impact of scaffold mineralization on mechanical properties was also assessed. PCL/PDMS scaffold properties were related to M_c, PDMS content, and PCL/PDMS phase separation.

3.3. Materials and Methods

3.3.1. Materials

Poly(ε-caprolactone) diol (PCL_{90}-diol; M_n ~10k g/mol), trimethylamine (Et_3N), acryloyl chloride, 4-dimethylaminopyridine (DMAP), 2,2-dimethoxy-2-phenylacetophenone (DMP), 1-vinyl-2-pyrrolidinone (NVP), potassium carbonate (K_2CO_3), sodium hydroxide (NaOH), potassium hydroxide (KOH), sodium chloride (NaCl), octamethylcyclotetrasiloxane (D_4), triflic acid, hexamethyldisilazane (HMDS), ε-caprolactone, stannous 2-ethylhexanoate, sodium chloride (NaCl), sodium bicarbonate ($NaCO_3$), potassium chloride (KCl), dipotassium hydrogen phosphate trihydrate ($K_2HPO_4 \cdot 3H_2O$), magnesium chloride hexahydrate ($MgCl_2 \cdot 6H_2O$), calcium chloride ($CaCl_2$), sodium sulfate (Na_2SO_4), phosphate buffered saline (PBS; pH 7.4) and tris(hydroxymethyl)aminomethane were obtained from Sigma-Aldrich. Anhydrous magnesium sulfate ($MgSO_4$) was obtained from Thermo Fisher Scientific. Tetramethyldisiloxane (tetra-SiH), tetrakis(dimethylsiloxy)siloxane (tetrakis-SiH), platinum-divinyltetramethyldisiloxane complex in xylene (Karstedt's catalyst) and were obtained from Gelest. Reagent-grade dichloromethane (CH_2Cl_2) and NMR-grade $CDCl_3$ were dried over 4 Å molecular sieves prior to use.

3.3.2. Synthesis

All reactions were conducted in oven-dried (120 ºC) glassware with Teflon- covered magnetic stir bars to agitate reaction mixtures. Reactions were run under positive nitrogen (N_2)

pressure. Chemical structures (including M_n) were confirmed with ^{1}H NMR spectroscopy (500 MHz spectrometer operating in the FT mode with $CDCl_3$ as the standard). The purified macromers' thermal properties were characterized using differential scanning calorimetry (DSC, TA Instruments Q100) as described below.

PCL-DA. PCL_{90}-diol (M_n = ~10k g/mol; Sigma Aldrich) was functionalized with terminal acrylate groups (OAc) to form PCL_{90}-DA as previously reported.[102] Briefly, PCL-diol (20.0 g, 2.0 mmol) was dissolved in CH_2Cl_2 (120 mL) with DMAP (6.6 mg) as the catalyst. Triethylamine (0.56 mL, 4.0 mmol) and acryloyl chloride (0.65 mL, 8.0 mmol) were sequentially added dropwise to the flask, and the reaction was stirred at room temperature (RT) for 30 min. The crude polymer was purified to obtain PCL-DA (~80% yield). ^{1}H NMR and DSC analyses agreed with that previously reported. M_n ~10k g/mol; >90% acrylation; $T_{m,\mathrm{PCL}}$ = ~53 ºC; PCL % crystallinity = ~48%.

Linear-PDMS$_{66}$-SiH. Linear-PDMS$_{66}$-SiH (i.e. having silane end groups) (M_n = ~5k g/mol) was prepared according to a modified previous report.[194] Briefly, D_4 (60.0 g, 202.7 mmol) and tetra-SiH (1.6 g, 12.3 mmol) underwent acid-catalyzed ring-opening polymerization (ROP) in the presence of triflic acid (120 μL, 1.35 mmol) overnight (ON) at RT. The reaction was quenched with HMDS (282 μL, 1.35 mmol) with stirring for 1 hr. The solution was filtered (Ashless, Grade 42) and the product vacuum dried ON to yield a colorless liquid (~72% yield). M_n = ~4125 g/mol; ^{1}H NMR: ^{1}H NMR (δ, ppm): 0.11 (bm, 411H, $SiCH_3$), 3.56 (m, 2H, Si*H*); $T_{g,\mathrm{PDMS}}$ = -120 ºC.

Linear-PDMS$_{66}$-DMA. Linear-PDMS$_{66}$-DMA (i.e. having methacrylate end groups) (M_n = ~5k g/mol) was prepared by Karstedt's-catalyzed hydrosilylation of terminal silane groups of *linear-PDMS$_{66}$-SiH* with allyl methacrylate according a protocol previously reported.[194] *Linear-PDMS$_{66}$-SiH* (7.0 g, 1.4 mmol), allyl methacrylate (0.38 g, 3.1 mmol), toluene (35 mL), and

Karstedt's catalyst (50 μL) were combined and maintained at 90 ºC for 12 hr. The catalyst was removed from the reaction mixture by refluxing with activated charcoal for 6 hr. Following filtration, volatiles were removed under reduced pressure to isolate the product as a colorless liquid (~72% yield). M_n = ~4651 g/mol; ~82 % acrylation; ^{1}H NMR (δ, ppm): 0.12 (bm, 421H, Si*CH_3*), 0.62 (m, 4H, -Si*CH_2*CH_2CH_2), ~1.74 (m, 4H, -SiCH_2*CH_2*CH_2), 1.98 (m, 6H, -C(CH_2)(*CH_3*), 4.22 (m, 6H, -SiCH_2CH_2*CH_2*), 5.58 (m, 2H, -C(*CH_2*)(CH_3)) and 6.27 (m, 2H, -C(*CH_2*)(CH_3)); $T_{g,\mathrm{PDMS}}$ = -120 ºC.

Star-PDMS$_{66}$-SiH. Star-PDMS$_{66}$-SiH (i.e. having silane end groups) was synthesized according to a prior report.[194] Briefly, D_4 (60.0 g, 202.7 mmol) and tetrakis-SiH (4.1 g, 12.3 mmol) underwent acid-catalyzed ROP in the presence of triflic acid (120 μL, 1.35 mmol) ON at RT. Following quenching with HMDS (282 μL, 1.35 mmol) was added as a neutralization agent, stirring for 1 hr at RT, after which the solution was filtered (Ashless, Grade 42) and vacuum dried ON to isolate the final produce (~78% yield). M_n = ~4334 g/mol; ^{1}H NMR (δ, ppm): 0.04-0.27 (bm, 420H, Si*CH_3*), 4.9 (m, 4H, Si*H*); $T_{g,\mathrm{PDMS}}$ = ~ -120 ºC.

Star-PDMS$_{66}$-TMA. Star-PDMS$_{66}$-TMA (i.e. 4-arm star architecture, having methacrylate end groups) was prepared by Karstedt's-catalyzed hydrosilylation of terminal silane groups of *star-PDMS$_{66}$-SiH* with allyl methacrylate according a prior report.[194] *Star-PDMS$_{66}$-SiH* (7.0 g, 1.4 mmol), allyl methacrylate (0.76 g, 6.2 mmol), toluene (35 mL), and Karstedt's catalyst (50 μL) were combined and were maintained at 90 ºC for 12 hr. The catalyst was removed from the reaction mixture by refluxing with activated charcoal for 6 hr. Following filtration, volatiles were removed under reduced pressure to isolate the product as a colorless liquid (~73% % yield). M_n = ~4827 g/mol; ~81% acrylation; ^{1}H NMR (δ, ppm): 0.02-0.17 (bm, 442H, Si*CH_3*), 0.51 (m, 8H, -Si*CH_2*CH_2CH_2), 1.65 (m, 8H, -SiCH_2*CH_2*CH_2), 1.97 (m, 12H, -C(CH_2)*CH_3*), 4.14 (m, 8H, -

$SiCH_2CH_2\mathit{CH_2}$), 5.62 (m, 4H, -C($\mathit{CH_2}$)CH_3), and 6.18 (m, 4H, -C($\mathit{CH_2}$)CH_3); $T_{g,\mathrm{PDMS}}$ = -120 ºC.

Synthesis of AcO-PCL$_{45}$*-b-PDMS*$_{66}$*-b-PCL*$_{45}$*-OAc*. The triblock macromer (M_n = 10k g/mol) was synthesized as previously reported.[197] Briefly, NH_2-PDMS$_{66}$-NH_2 (i.e. having terminal aminopropyl groups) was prepared by the base-catalyzed ROP of D_4 in the presence of bis(3-aminopropyltetramethyldisiloxane) and KOH. Next, NH_2-PDMS$_{66}$-NH_2 (5.6 g, 1.1 mmol) was reacted with ε-caprolactone (9.4 g, 82.3 mmol), and stannous 2-ethylhexanoate (0.04 g, 0.01 mmol) to yield the HO-PCL$_{45}$-*b*-PDMS$_{66}$-*b*-PCL$_{45}$-OH. Lastly, the hydroxyl end groups were acrylated by reacting with acryloyl chloride to yield AcO-PCL$_{45}$-*b*-PDMS$_{66}$-*b*-PCL$_{45}$-OAc (~81% yield). The ^{1}H NMR spectra and thermal analysis were each in agreement with that previously reported. M_n ~15k g/mol; >90% acrylation; $T_{m,\mathrm{PCL}}$ = ~53 ºC; PCL % crystallinity = ~48%.

3.3.3. SMP Scaffold Fabrication

Porous scaffolds were fabricated via solvent-cast particulate leaching (SCPL) method with a fused salt template to achieve pore interconnectivity.[102] NaCl particles were sieved to two sizes: 459 ± 69 μm (with a sieve with 425 μm openings) and 355 ± 50 μm (with a sieve having 425 μm openings followed by a sieve with 355 μm openings). The average size of each group was determined with scanning electron microscopy (SEM; JEOL 6400 SEM, 10kV accelerating voltage) images ImageJ® software. Sieved salt (10 g) was placed in a 20 mL scintillation glass vial (I.D. = 25 mm) and deionized (DI) water (7.5 wt %) added in four portions via manually mixing with a spatula. The hydrated salt was pressed down to the bottom of the vial with a blunt glass rod, and the capped vial then centrifuged (3220 x *g*, 15 min). The open vials were then air-dried (RT, 1 hr), and then vacuum dried (RT, 12 hr, 36 in. Hg).

Precursor solutions were prepared with the designated macromer(s) (0.15 g per mL CH_2Cl_2) and 15 vol % of a photoinitiator solution (10 wt % DMP in NVP). The wt% ratios of PCL-DA to *linear*-PDMS-DMA or *star*-PDMS-TMA were 90:10, 75:25, and 60:40. Precursor solutions were also formed exclusively with PCL-DA (i.e. 100:0 wt % ratio of PCL to PDMS) as well as with AcO-PCL_{45}-*b*-$PDMS_{66}$-*b*-PCL_{45}-OAc (i.e. 65:35 wt% ratio of PCL to PDMS).[20] Following vortexing, a designated precursor solution (~6 mL) was promptly added to a fused salt template. In order to achieve a similar final scaffold pore size in the targeted range (200-350 µm), the template salt size was selected to account for the extent of shrinkage that occurred with the final annealing step. Thus, salt templates (~459 µm salt) were used for precursor solutions based on PCL-DA and PCL-DA in combination with *linear*-PDMS-DMA or *star*-PDMS-TMA. For AcO-PCL_{45}-*b*-$PDMS_{66}$-*b*-PCL_{45}-OAc precursor solutions, salt templates (~355 µm salt) were utilized. The vials were centrifuged (1260 x *g*, 10 min) and exposed to UV light (UV-Transilluminator; 6 mW/cm^2, 365 nm) for 3 min. After air-drying (RT, 12 hr), the SMP scaffolds were removed from the vials. To remove the salt template, scaffolds were soaked in a water/ethanol mixture (1:1 vol:vol) for 4 days with daily solution changes. Upon removal from the vial and air-drying (RT, 12 hr), the resulting cylindrical monolith was annealed (85 °C, 1 hr, 36 in. Hg). After 48 hr at RT, the cylinder (avoiding the top and bottom portions) was were sliced into three specimens (*t* ~2 mm) (Vibratome, Leica VT 1000 S) and subsequently biopsy punched (Integra Miltex) to reduce the diameter (*d* ~ 6 mm). Thus, final scaffold specimen dimensions were *d* ~6 mm x *t* ~ 2 mm.

3.3.4. SMP Film Fabrication

Analogous SMP solid films were prepared. Precursor solutions were prepared with the designated macromer(s) (0.15 g per mL CH_2Cl_2) and 15 vol % of a photoinitiator solution (10 wt

% DMP in NVP). The wt% ratios of PCL-DA to *linear*-PDMS-MA or *star*-PDMS-TMA were 90:10, 75:25, and 60:40. Precursor solutions were also formed exclusively with PCL-DA (i.e. 100:0 wt % ratio) as well as AcO-PCL_{45}-*b*-$PDMS_{66}$-*b*-PCL_{45}-OAc (i.e. 65:35 wt% ratio of PCL to PDMS).[20] The precursor solutions were pipetted into individual circular silicone molds (45 mm diameter x 2 mm height; McMaster-Carr) sandwiched between two glass slides and exposed to UV light (UV-Transilluminator; 6 mW cm^2, 365 nm) for 3 min (1.5 min per side). The resulting solvent-swollen discs were removed from the molds carefully, air dried (RT, 12 hr), and vacuum dried (RT, 4 hr, 36 in. Hg) to remove solvent. Uncrosslinked material was removed by soaking the discs in ethanol (3 hr). The discs were subsequently air-dried (RT, 12 hr) and annealed *in vacuo* (85 °C, 1 hr, 36 in. Hg). After 48 hr at RT, specimens were harvested using 5 mm biopsy punch. Thus, final dimensions of film discs were *d* ~5 mm x *t* ~1.1 mm.

3.3.5. SMP Scaffold Characterization

Average molecular weight between crosslinks (Mc). M_c values of the various wt % and architectures PDMS co-matrices were calculated by **(1)**.

$$\mathrm{M}_c = (a * M_{PCL}) + (b * M_{PDMS}) \qquad \textbf{(1)}$$

Where M_{PCL} is the molecular weight of PCL-DA between crosslinks (10k g/mol), M_{PDMS} is the molecular weight of PDMS between crosslinks (5k g mol^{-1} for *linear*-PDMS-DMA, and 2.5k g mol^{-1} for *star*-PDMS-TMA), and *a* and *b* the mass fraction of PCL and PDMS, respectively. As calculated values of M_c decreased, relative crosslink density was considered to increase and vice versa.

Pore size and morphology. Scaffold pore size and pore interconnectivity were evaluated via SEM. Scaffold cross-sections were subjected to Au−Pt coating (~4 nm). From the SEM images

($N = 8$) (JEOL 6400; 10kV accelerating voltage), the average pore size was determined from pores measured along each image midline with ImageJ software.

PCL crystallinity. The PCL melting temperature (T_m) and % crystallinity of each scaffold composition was determined by differential scanning calorimetry (DSC, TA Instruments Q100). Specimens (~15 mg, $N = 3$) were each sealed in hermetic pans and heated from RT to 200 °C at a rate of 5 °C/min. Values were taken from the second DSC cycle to remove any thermal history. From the endothermic PCL melt peak, T_m was determined from the maximum point and enthalpy change (ΔH_m) were calculated from the peak area (TA Universal Analysis software). PCL percent crystallinity (% χ_c), with a correction factor included to account for the varying PCL wt% among the compositions, was calculated by **(2)**:

$$\% \chi_c = \frac{\Delta H_m - \Delta H_c}{\Delta H_m^0 * w} * 100 \qquad \textbf{(2)}$$

where ΔH°_m as the enthalpy of fusion of theoretical 100% crystalline PCL (139.5 J/g),[163] and w the mass fraction of the PCL (e.g. $w = 0.90$ for PCL for the 90:10 PCL-DA:*linear*-PDMS$_{66}$-DMA).

Shape memory behavior. Shape memory properties were quantified via strain-controlled cyclic-thermal mechanical compression tests over two cycles (C) (TA Instrument Q800 DMA). Specimens (d ~ 6 x t ~ 2 mm; $N = 3$) were subjected to the following sequence: (1) after equilibrating at 60 °C for 10 min, compress to a maximum strain ($\varepsilon_m = 50\%$) at a rate of 50 %/min, (2) hold at ε_m for 5 min and then cool to 25 °C to fix the temporary shape, (3) remove the load and immediately measure ε_u, and (4) reheat to 60 °C to recover the permanent shape, measure the recovered strain (ε_p), and to start the next cycle. The first cycle ($C = 0$) is referred to as the "pre-cycle" and is followed by $C = 1$. After shape recovery ($C = 0$), the specimen was cooled to RT and the new dimensions of the pre-cycled specimen was recorded and used for the subsequent cycle C

= 1). The shape fixity (R_f) and shape recovery (R_r) for the first ($C = 0$) and second ($C = 1$) cycles were calculated using the following equations **(3)** and **(4)**:

$$R_f(\mathrm{C}) = \frac{\varepsilon_u(C)}{\varepsilon_m} \quad \textbf{(3)}$$

$$R_r(\mathrm{C}) = \frac{\varepsilon_m - \varepsilon_p(C)}{\varepsilon_m - \varepsilon_p(C-1)} \quad \textbf{(4)}$$

$\varepsilon_u(C)$ is the ultimate strain in the stress-free state in the fixing process. ε_m is the maximum compressive strain (50%). $\varepsilon_p(C - 1)$ and $\varepsilon_p(C)$ are the final strains of the specimen after the two successive cycles in the stress-free state during the shape recovery process. For pre-cycles ($C = 0$), $\varepsilon_p(-1)$ equals “zero”.

Accelerated degradation. Specimens ($d \sim 6$ x $t \sim 2$ mm, $N = 3$ per time point) were each immersed in 10 mL of 1 M NaOH in a sealed 20 mL glass scintillation vial and maintained atop a rocker table (37 °C, 60 rpm). At 24, 48, 72, and 96 hr, the designated specimens were removed, thoroughly rinsed with DI water, and dried *in vacuo* (RT, 12 hr, 36 in. Hg). The mass of the dried specimen was recorded and compared to their initial mass to determine % mass loss. Specimens were used for a single time point (i.e. not used for subsequent time points).

Non-accelerated Degradation. Specimens ($d \sim 6$ x $t \sim 2$ mm, $N = 3$ per time point) were each immersed in 10 mL of PBS (pH = ~ 7.4) in a sealed 20 mL glass scintillation vial and maintained atop a rocker table (37 °C and 60 rpm). At 3, 6, 9, 12, 15, 18, 21, and 24 months, the designated specimens were taken from solution, thoroughly rinsed with DI water, and dried *in vacuo* (RT; 12 hr; 36 in. Hg). The mass of the dried specimen was recorded and compared to their initial mass to determine % mass loss. Specimens were used for a single time point (i.e. not used for subsequent time points).

Bioactivity. SBF (1X) was prepared as described by Kokubo.[165] Specimens (*d* ~ 6 x *t* ~ 2 mm, *N* = 3) were each placed in a sealed centrifuge tube containing 20 mL of SBF and submerged at 37 °C. After 30 days, specimens were removed, thoroughly rinsed with DI water, dried *in vacuo* (RT, 12 h, 36 in. Hg), and sectioned with a stainless-steel blade to expose the cross-section. Specimens were subjected to Au-Pt sputter coating (~7 nm). FEI Q600 SEM-Energy Dispersive X-ray Spectroscopy (EDS) was utilized to visualize and identify possible mineralization of a calcium phosphate deposition of HAp via elemental molar composition analysis.

Compressive mechanical properties. Specimens (*d* ~ 6 x *t* ~ 2 mm, *N* = 5) underwent static compression tests (Instron 5944) at RT. A constant strain rate (1.5 mm/min) was up to 85% strain. From the resulting stress−strain curves, modulus (*E*) was determined from the slope in the initial linear region (< ~10% ε). Compressive strength (*CS*) was determined from the stress at 85% strain. These values were measured also on scaffolds following 30 days exposure to SBF followed by drying *in vacuo* (RT, ~24 hr, 30 in. Hg).

3.3.6. SMP Film Characterization

Sol content. Weighed film discs (*d* ~5 mm x *t* ~1.1 mm, *N* = 3) were each submerged in 10 mL CH_2Cl_2 in a 20 mL scintillation vial. Sealed vials were placed atop a shaker table (48 hr, 150 rpm) and subsequently rinsed with CH_2Cl_2, air dried (RT, ON), dried *in vacuo* (RT, ~24 hr, 30 in. Hg), and weighed. The initial and final weights of specimens were used to determine % sol content.

Phase separation. Differences in phase separation (i.e. miscibility) were observed from SEM images of the surfaces and cross sections (*N* = 3). Specimens were subjected to Au-Pt sputter coating (~7 nm), and images obtained (JEOL 6400 SEM, 10kV accelerating voltage).

3.3.7. Statistical Analyses

Data were reported as a mean ± standard deviation. Values were compared in GraphPad Prism via ANOVA followed by a t-test where a p-value of < 0.05 was considered statistically significant.

3.4. Results and Discussion

3.4.1. Fabrication

PCL/PDMS scaffolds were successfully prepared using a SCPL protocol. To confirm adequate crosslinking of macromers to form co-matrices, sol contents of the analogous films were measured (**Table A-10**). Both the PCL-DA control (100:0) and PCL/PDMS compositions produced similarly low sol contents (~10-12%). SEM images of scaffolds revealed that pore interconnectivity was achieved, attributed to the fused salt template employed in the SCPL (**Figure A-6**). In order to compare scaffold properties based on chemical compositions, a consistent average pore size was sought. Thus, a smaller average sized sieved salt average size was used to fabricate the triblock 65:35 scaffold due to its relatively decreased extent of shrinkage during the final annealing step. The PCL-DA and PCL/PDMS scaffolds all exhibited similar pore sizes (~230 µm) which is also within the targeted range to support osteogenesis[182-184] (**Figure A-7**). Moreover, following self-fitting of a representative scaffold into a model irregular defect, most pores remained rather open along the edge (i.e. the portion in contact with the mold perimeter) (**Figure A-8**).

3.4.2. M_c, PCL crystallinity, and shape memory behavior

Given the expected impact on shape memory behavior, degradation, and mechanical properties, the molecular weight between crosslinks (M_c) as well as PCL crystallinity were determined (**Table 3-1**). Co-matrix scaffold M_c values decreased (i.e. crosslink density increased)

Table 3-1. Compositions, % crystallinity, T_m, M_c, Shape Fixity, and Shape Recovery

Matrix Composition	**M_c (g mol^{-1})**	**% crystallinity**	**T_m (°C)**	**R_r (%) (C = 1)**	**R_f (%) (C =1)**
PCL-DA 100:0	10,000	47.7 ± 3.2	54.3 ± 1.6	97.47 ± 0.4	100.9 ± 1.0
PCL-DA/*linear*-PDMS-DMA 90:10L	9,500	48.1 ± 2.1	56.1 ± 1.1	94.3 ± 2.2	100.8 ± 0.8
PCL-DA/*linear*-PDMS-DMA 75:25L	8,750	52.9 ± 0.9	55.1 ± 1.3	98.7 ± 0.8	101.4 ± 2.9
PCL-DA/*linear*-PDMS-DMA 60:40L	8,000	54.1 ± 1.1	55.3 ± 1.2	96.3 ± 0.5	101.1 ± 0.5
PCL-DA/*star*-PDMS-TMA 90:10S	9250	47.2 ± 1.5	54.9 ± 1.6	98.9 ± 0.4	103.5 ± 1.1
PCL-DA/*star*-PDMS-TMA 75:25S	8,125	49.1 ± 2.4	53.4 ± 1.1	97.1 ± 0.9	102.6 ± 2.1
PCL-DA/*star*-PDMS-TMA 60:40S	7,000	55.1 ± 1.2	55.6 ± 1.8	91.1 ± 1.4	101.9 ± 2.2
***Triblock* 65:35**	15,000	44.2 ± 2.1	52.6 ± 2.1	92.6 ± 0.7	99.4 ± 1.1

when PCL-DA was combined with increased levels of *linear*-PDMS$_{66}$-DMA or *star*-PDMS$_{66}$-TMA. The triblock 65:35 macromer produced with the highest M_c value (i.e. lowest crosslink density), even higher than that produced by PCL-DA. The PCL-DA scaffold exhibited a ~45% crystallinity (T_m ~55 °C). Despite the inclusion of PDMS segments at varying concentrations and architectures, PCL % crystallinity was not substantially altered. This indicates that the PDMS segments do not interfere with PCL crystallization, even at higher PMDS levels that also lead to reduced M_c values (i.e. higher crosslink densities). Attributed to their similar PCL crystallinity, the PCL/PDMS scaffolds exhibited similarly excellent shape recover (R_r) and shape fixity (R_r) (~100% and ≥ 91%, respectively) (C = 1) versus the PCL-DA scaffold (**Table 3-1**). R_r values were quite a bit lower for the pre-cycle (C = 0) versus the subsequent cycle (C = 1) (**Table A-11**). This is consistent with prior reports and is attributed to the first shape memory cycle removing the residual strain that originates from fabrication, such that subsequent shape recovery is improved.[20, 178, 196, 198] For most compositions and for both cycles, R_f slighter higher than 100% due to an additional compression of up to 0.7% strain (ε). This is also consistent with prior reports[20, 196] and is thought to result from the rapid crystallization of PCL, resulting in a more compact structure during the cooling process. Such R_f values may also be attributed to compression-induced crystallization of PCL. Overall, these results show that PCL/PDMS scaffolds exhibit shape memory behavior similar to the PCL-DA control and so may be used as self-fitting scaffolds. Given all scaffolds' similarly lower R_r ($C = 0$) values, pre-conditioning prior to self-fitting would maximize expansion into a defect via shape recovery.

3.4.3. Degradation Rates

Summarized in **Figure 2**, the relative rates of scaffold degradation were determined in both accelerated (i.e. basic) (**Table A-12, Figure A-9**) and non-accelerated (i.e. pH ~7.4) (**Table A-13, Figure A-10**) conditions. As *linear*-$PDMS_{66}$-DMA wt% increased, scaffold degradation rate increased and was faster than the PCL-DA control (i.e. 100:0 < 90:10L < 75:25L < 60:40L) This trend was also observed for scaffolds based on *star*-$PDMS_{66}$-TMA (i.e. 100:0 < 90:10S < 75:25S < 60:40S). Thus, despite its hydrophobicity, an increase in PDMS content gave rise to faster degradation rates. Finally, the scaffold based on the triblock macromer (triblock 65:35) degraded the fastest among all scaffolds. In this way, PDMS levels and architecture effectively tuned PCL/PDMS scaffold degradation rate. These trends in degradation rates were first considered in terms of crosslink density, which increases with decreasing Mc. By diminishing material-water interactions within crosslinked networks, a higher crosslink density is known to reduce the hydrolytic degradation rate.[199, 200] Among scaffolds with similarly high PDMS levels, degradation rates increase in order from: star < linear < triblock (e.g. 60:40S < 60:40L < triblock 65:35). Thus, as expected, degradation rates increased as crosslink density decreased (i.e. as M_c increased in the order star < linear < triblock). Additionally, the contributions from phase separation between PCL

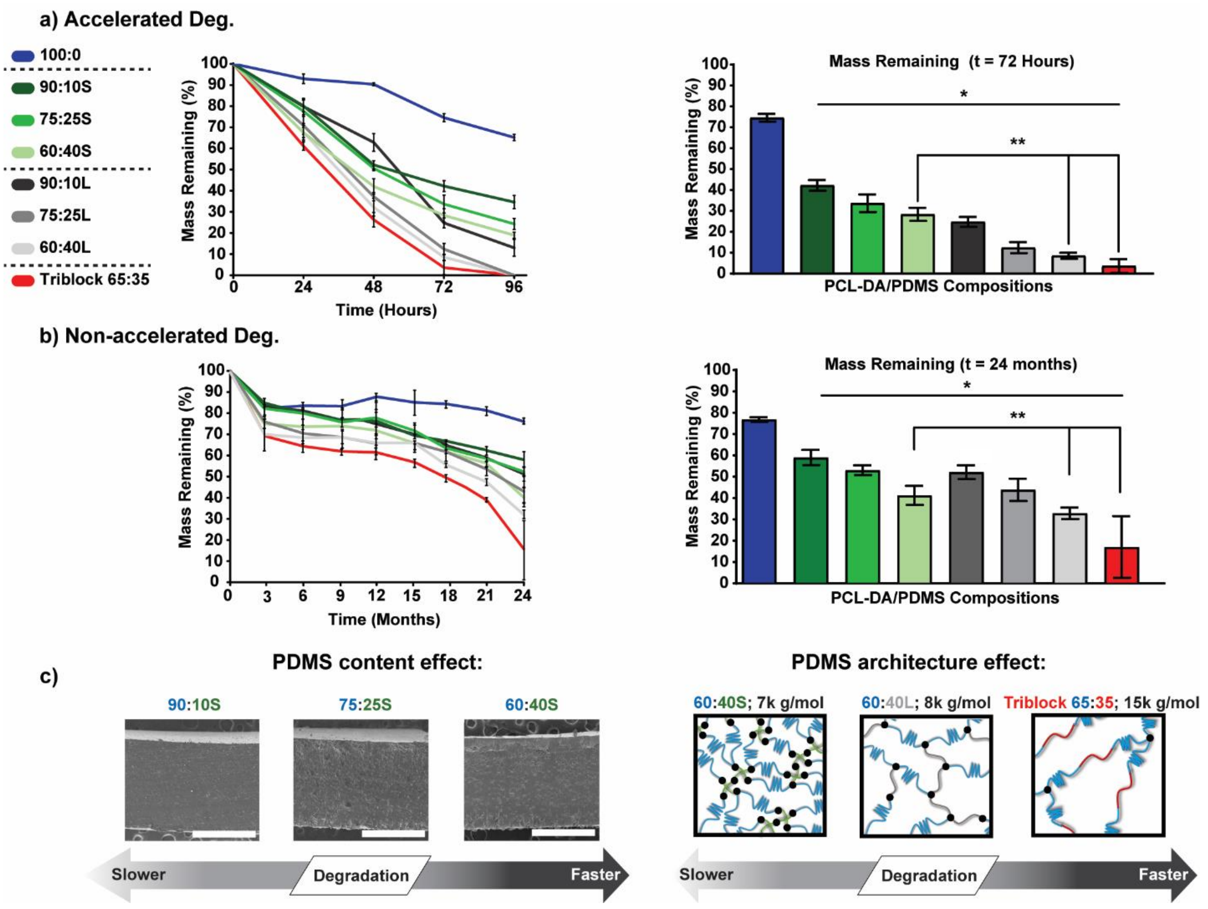

Figure 3-2. (a) Accelerated degradation of scaffolds up to 96 hours. (b) Non-accelerated degradation of scaffolds up to 21 months. (c) Effect of PDMS content and architecture on degradation rates. Scale bar = 500 µm. **p* < 0.05 vs PCL-DA control. ***p* < 0.05 vs similar "high PDMS-content" compositions (i.e. 60:10S, 60:40L, and triblock 65:35).

and PDMS to degradation rates was considered. As noted in our prior work with semi-IPN PCL-DA/PLLA scaffolds, phase separation increased with PLLA content and coincided with increased degradation rates.[128, 173] This was attributed to enhanced water permeability with phase separation, such as that observed for blends.[201-203] In addition to a different polymer type (PDMS rather than PLLA), the present scaffolds were co-matrices (rather than semi-IPNS). Thus, PDMS segments do not exist as non-crosslinked chains, with presumed greater mobility, within the PCL-DA networks. SEM images of analogous film cross-sections (**Figure 3-3**) and surfaces (**Figure A-11**)

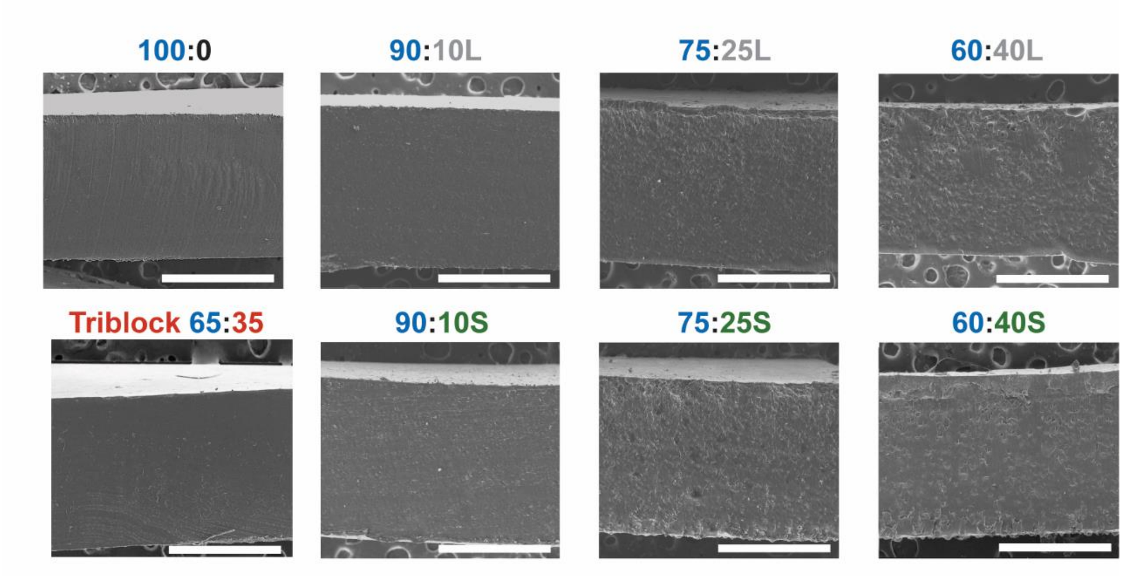

Figure 3-3. SEM imaging film cross-sections. Scale bars = 500 µm

were used to assess differences in the extent of phase separation. As expected, the PCL-DA control (100:0) showed a uniform, smooth morphology while co-matrix films exhibited immiscible domains. For co-matrices based on *linear*-PDMS$_{66}$-DMA and *star*-PDMS$_{66}$-TMA, phase separation increased with PDMS content. This greater phase separation occurred despite a concomitant increased crosslink density (i.e. decreased M_c). Thus, both PDMS content and crosslink density impact degradation rates of these co-matrix scaffolds. Interestingly, the triblock 65:35 scaffold did not exhibit substantial phase separation, despite its high PDMS content. As noted above, it relatively rapid rate of degradation is attributed to its low crosslink density.

3.4.4. Bioactivity

To assess the innate bioactivity of PCL/PDMS scaffolds, following exposure to 1X SBF, the formation of HAp was evaluated by imaging specimen cross-sections (**Figure 3-4**). SBF, by mimicking the ion concentrations, pH, and temperature of human blood plasma, is a useful *in vitro* predictor of bioactivity.[165] While the PCL-DA scaffold (100:0) showed no evidence of

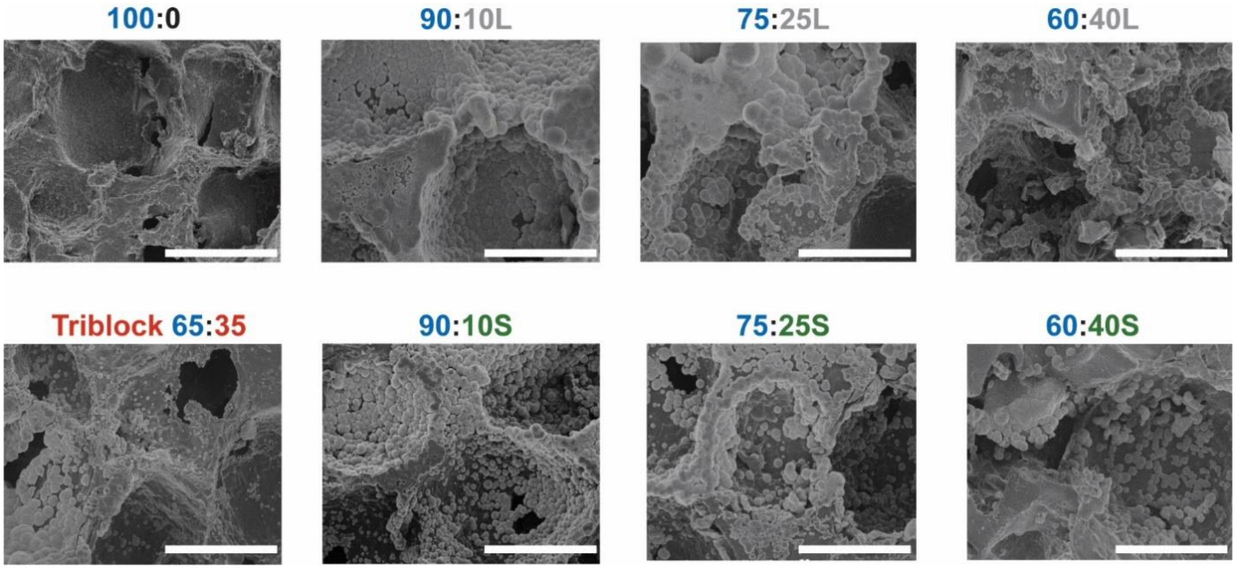

Figure 3-4. SEM images of scaffold cross-sections after soaking 1 month in 1X SBF. Scale bars = 150 μm.

mineralization, all PCL/PDMS scaffolds exhibited substantial deposits on pore walls. Mineralization throughout the PCL/PDMS scaffolds is attributed to pore interconnectivity that facilitated exposure to SBF. Using SEM-EDS, these mineral deposits were confirmed to be carbonated HAp [$Ca_{10}(PO_4)_6(OH)_2$], having a Ca:P molar ratio ~1.67 (**Figure A-12**).[204-207] The innate bioactivity of the PCL/PDMS scaffolds, even with relatively low levels of PDMS (e.g. 90:10L and 90:10S), is notable and is attributed to the hydrophobic, Si-containing PDMS segments.

3.4.5. Mechanical properties

Because of the low T_g (~120 °C) of PDMS, the inclusion of PDMS segments within the PCL-based co-matrices was expected to soften and reduce the strength of scaffolds. Specimens were subjected to compression tests to determine compressive modulus (*E*) (**Figure 3-5, Table A-14**) and compressive strength (*CS*) (**Figure A-13, Table A-15**). As anticipated, *E* and *CS* decreased with increasing PDMS-content (i.e. 60:40S < 75:25S < 90:10S < 100:0 and 60:40L < 75:25L <

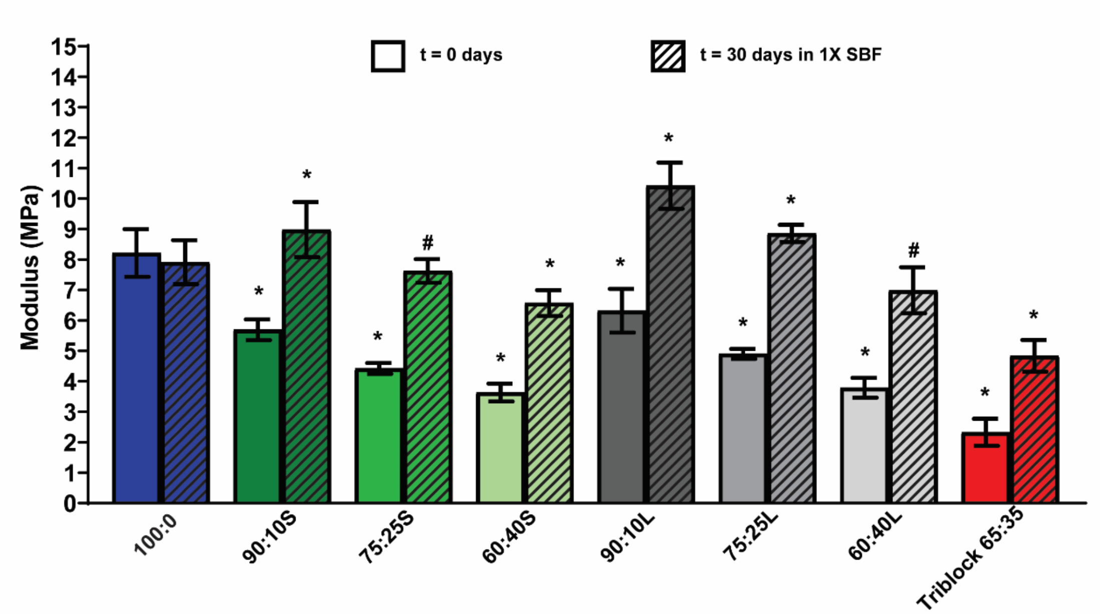

Figure 3-5. Modulus values of scaffolds at *t* = 0 and 30 days in 1X SBF. $*p < 0.05$ vs PCL-DA control under similar conditions (t = 0 or 30). $\#p > 0.05$ vs PCL-DA control under similar conditions (t = 0 or 30).

90:10L < 100:0). The triblock 65:35 scaffold was the least rigid and strong, attributed to both a high PDMS content and low crosslink density.

The reduction in rigidity and strength relative to the PCL-DA (100:0) scaffold is a potential drawback of PCL/PDMS scaffolds in terms of the ability to provide structural support within a bone defect during healing. However, following mineralization, these exhibited pronounced increases in these properties (**Figure 3-5, Table A-14, Figure A-13, Table A-15**). Importantly, mineralized 90:10S, 90:10L, and 75:25L scaffolds exhibited moduli statistically greater than that of the PCL-DA control. For mineralized 75:25S and 60:40L scaffolds, moduli were similar to the control. Due to its high PDMS content and low crosslink density, the mineralized triblock 65:35 exhibited the lowest modulus. In the case of compressive strength, mineralized 90:10L scaffold is greater than and 90:10S scaffold is similar to the PCL-DA control.

3.5. Conclusions

Scaffolds that are able to conformally fit into irregular geometries, exhibit innate bioactive, and degrade at a sufficient rate to promote neotissue infiltration are expected to enhance healing of cranial bone defects. The inclusion of PDMS was hypothesized to impart bioactivity as well as to accelerate degradation rates relative to PCL-DA only scaffolds. Thus, PCL/PDMS SMP scaffolds were formed as co-matrices using different macromers (linear, star, and triblock) to control PDMS content as well as crosslink density. Specifically, PCL_{90}-DA was combined with *linear*-$PDMS_{66}$-dimethacrylate (DMA) or *star*-$PDMS_{66}$-tetramethacrylate (TMA) macromers at 90:10, 75:25, and 60:40 wt % ratios. A triblock macromer AcO-PCL_{45}-*b*-$PDMS_{66}$-*b*-PCL_{45}-OAc [65:35 wt% ratio PCL:PDMS] was also used. Scaffolds were successfully formed with interconnected pores and a similar pore size (~230 μm) conducive to osteogenesis. The incorporation of PDMS segments did not substantially impact PCL crystallinity such that shape memory behavior, essential to self-fitting behavior, was preserved. Scaffold degradation was assessed both in accelerated (basic) and non-accelerated (neutral) conditions. All PCL/PDMS scaffolds exhibited faster degradation rates versus the PCL-DA control. For scaffolds based on both linear and star PDMS macromers, degradation rates increased with PDMS higher contents. The triblock 65:35 scaffold degraded the fastest. Among scaffolds with similarly high PDMS levels, degradation rates increase in order from: star < linear < triblock (e.g. 60:40S < 60:40L < triblock 65:35); this expectedly coincided with a decreased crosslink density. For PCL/PDMS compositions based on linear and star PDMS macromers, phase separation was also observed and also contributes to faster rates of degradation versus PCL-DA. HAp mineralization was observed on all PCL/PDMS scaffolds after 1 month in SBF (1X) but not for PCL-DA. Thus, these PCL/PDMS scaffolds are innately bioactive and should promote bonding and integration with adjacent bone tissue. Since the PDMS is distributed throughout the bulk, this property would be maintained as the scaffold erodes. Due to the low T_g of PDMS, PDMS/PCL scaffolds exhibited lower compressive modulus and strength values versus the PCL-DA scaffold. However, following mineralization, these values increased and, in some cases, exceeded or met that of PCL-DA. Thus, PDMS/PCL SMP scaffolds uniquely meet the criteria expected to heal irregular cranial bone defects.

4. OSTEOGENIC POTENTIAL OF MODIFIED SILOXANE-CONTAINING SHAPE-MEMORY POLYMER (SMP) SCAFFOLDS WITH ENHANCED HYDROPHILICITY

4.1. Overview

"Self-fitting" shape memory (SMP) tissue scaffolds provide an ideal platform for a regenerative approach to heal irregular-shaped cranial defects that require conformal fitting. We have previously reported on SMP scaffolds based on poly(ε-caprolactone) diacrylate (PCL$_{90}$-DA) that shape recover to fill irregular defect geometries. However, PCL-DA scaffolds low degradation rates and lack of innate bioactivity limit regenerative and osteogenic potential. Furthermore, we reported on the incorporation *linear*-polydimethylsiloxane dimethacrylate (*linear*-PDMS$_{66}$-DMA) segments to form PCL-DA/*linear*-PDMS-DMA SMP scaffolds. These were prepared as co-matrices with varying wt% to systematically alter PDMS content (90:10L, 75:25L, and 60:40L; PCL:PDMS). PDMS-containing scaffolds maintained excellent shape memory, mechanical properties, innate bioactivty and enhanced degradation rates. However, while exhibiting the formation of hydroxyapatite (HAp) following exposure to to 1X simulated body fluid (SBF), rate of mineralization was slow (~4 weeks). Due to the hydrophobicity of PDMS, it was suspected that modification to pendant groups leading to increased hydrophilicity may result in higher susceptibility to degradation along with decreased time for mineralization. This predicted behavior is due to the method of polyester degradation (hydrolysis) and HAp-forming solutions being aqueous in nature. Herein, polyhydromethylsiloxane dimethacrylate (PMHS$_{66}$-DMA) was incorporated in a co-matrix with PCL-DA with similar wt% as previous PDMS investigation (90:10, 75:25, and 60:40; PCL:PMHS). When compared to PCL-DA control (100:0) and PDMS-containing scaffolds, PMHS groups had further degradation rates, faster mineralization times (~2 weeks), and enhanced post-mineralization mechanical properties. *In vitro* anaylsis of both siloxane-containing scaffolds exhibited noncyctotoxicty, suitable cellular distrubtion, increases in osteogenic marker expression, and decreases in off-target marker expression.

4.2. Introduction

The often irregular geometries that craniomaxillofacial (CMF) bone defects present challenge the regenerative capabilities of the current gold standard of treatment, autografting.[52, 55, 56] These difficult-to-match geometries lead to complications in conformally fitting rigid grafts, lack of contact to adjacent tissue, and premature resorption.[52-56] In response, we previously reported on thermoresponsive, biodegradable shape memory polymer (SMP) tissue scaffolds.[102] Based on poly(ε-caprolactone) (diacrylate) (PCL_{90}-DA, M_n ~10k g mol^{-1}), scaffolds exhibited shape memory that enabled "self-fitting" wherein crystalline lamellae ($T_{m,PCL}$ or "T_{trans}" ~55 °C) serve as switching segments while the netpoints are formed by chemical crosslinks. Fabrication by a fused salt template produced scaffolds with pore sizing and interconnectivity desired for neotissue infiltration (~200 to 350 µm). Upon exposure to warm air or saline (~55 °C), scaffolds become malleable such that they can be press-fit into irregular geometries, with shape recovery driving its expansion to fill the defect and shape fixity locking it into its new shape.[101, 102]Additionally, we reported on PCL-DA scaffolds coated with bioactive polydopamine (PD) forming hydroxyapatite (HAp) in 1X simulated body fluid (SBF).[102] PD-coated PCL-DA scaffolds were observed to promote osteogenesis through robust expression of runt-related transcription factor 2 (RUNX2), osteopontin (OPN) and osteonectin (OCN) when cultured with human mesenchymal stem cells (h-MSCs).[102] However, PD- coated scaffolds had limitations in erosion of coating during degradation (possibly reducing bioactive capabilities overtime). In response, development on a new generation of SMP scaffolds incorporating silicon polymer, polydimethylsiloxane (PDMS), led to faster degrading and innate bioactive mineral-forming scaffolds (no PD coating required).[105] PDMS was incorporated in co-matrix networks with PCL-DA by functionalized methacrylate (MA) terminal groups. Additionally, architecture of PDMS was varied by *linear*-PDMS$_{66}$-di(D)MA (M_n ~5k g mol^{-1}) and *star*-PDMS$_{66}$-tetra(T)MA (M_n ~5k g mol^{-1}). Subsequent PCL-DA/PDMS scaffolds exhibited PDMS-content (i.e. phase separation driven) increases to degradation rates and *in vitro* mineralization of hydroxyapatite (HAp) after 4 weeks in 1X SBF.[105] While a significant advancement in SMP scaffold design, other bioactive materials (i.e. bioglass) reported HAp mineralization within days [210] correlating to increases in osteogenic expression and healthy bone formation.[211, 212] Thus, while PCL-DA/PDMS scaffolds improved upon PCL-based SMP design, modifications to render enhanced rates of mineralization would further increase its regenerative potential and subsequently, greater osteogenic expression.

Conferment of material-driven bioactivity though PDMS is significant as it removed reliance on rigid HAp-forming silicon-based fillers (e.g., Bioglass® and nanosilicates) that would negatively impact scaffold shape memory.[187-189, 213] Silicones (i.e. siloxanes) are known to induce nucleation and precipitation of calcium phosphate layers through ionic complexation of cationic alkaline-earth metals (i.e. Ca^{2+})[214, 215] further leading to HAp mineralization.[216] However, PDMS-containing scaffolds have slow rates of mineralization (~4 weeks)[105] compared to filler-containing scaffolds (~few days).[210, 217, 218] As a consequence, filler-containing scaffolds are able to produce osteogenic promoting environments and bond to adjacent bone tissue at increased rates.[92] Chemical composition of PDMS and silicon fillers are similar though presence of silicone (-Si-O-) repeating structures. However, differences in siloxane pendant groups greatly affect their hydrophilic tendencies[219] (PDMS: dimethyl pendant groups, hydrophobic (θ ~105°)[220]; silicon-based fillers: no pendant groups, less hydrophobic (θ ~30°, Bioglass®)[221]). In a previous study, it was reported that decreases in hydrophobicity (i.e. wettability) of PCL surfaces lead to increased rates of HAp mineralization.[222] These studies looked at -OH granting surface level modifications rather than innate changes to polymer network afforded by PCL-DA/PDMS. However, the hydrophobic nature of PDMS may directly impact HAp formation as the mineral-forming ions suspended in aqueous physiological fluid (i.e. blood plasma) are impeded from nucleating on the surface. Thus, modification to PDMS pendant groups is suspected to potentially lead to scaffolds with enhanced rates of HAp mineralization and, furthermore, increase rates of hydrolytic degradation. In evaluating osteogenic potential, producing an environment conducive to the desired differentiation response is ideal. While PD-coated PCL-DA scaffolds have produced robust cell viability and osteogenic gene expression [102, 223] it is suspected that scaffolds that innately mineralize (no external coatings) would enhance associated behaviors. Herein, we hypothesized that single methyl pendant group siloxane polymer of polyhydromethylsiloxane dimethacrylate (PMHS-DMA) can be successfully crosslinked with PCL-DA to form PCL-DA/PMHS-DMA scaffolds with enhanced degradation and mineralization rates with increased osteogenic expression leading to an excellent platform for bone regeneration.

Towards enhancing the regenerative capacity of self-fitting SMP scaffolds, PMHS-DMA was incorporated to form PCL-DA/PMHS-DMA co-matrix scaffolds to yield innate and enhanced bioactivity as well as accelerated degradation rates. PCL_{90}-DA was systematically combined with $PMHS_{66}$-DMA (M_n ~5k g mol^{-1}) at 90:10, 75:25, and 60:40 wt% ratios. These scaffolds were directly compared to analogous PCL-DA/*linear*-PDMS-DMA scaffolds (90:10L, 75:25L and 60:40L wt% ratios) from previous studies[105] with a PCL-DA scaffold (100:0 wt%) serving as a control (**Figure 4-1**). Scaffolds were prepared using a solvent-casting, particulate leaching (SPCL) protocol to produce similar pore sizes as well as pore interconnectivity.[102] Scaffolds were

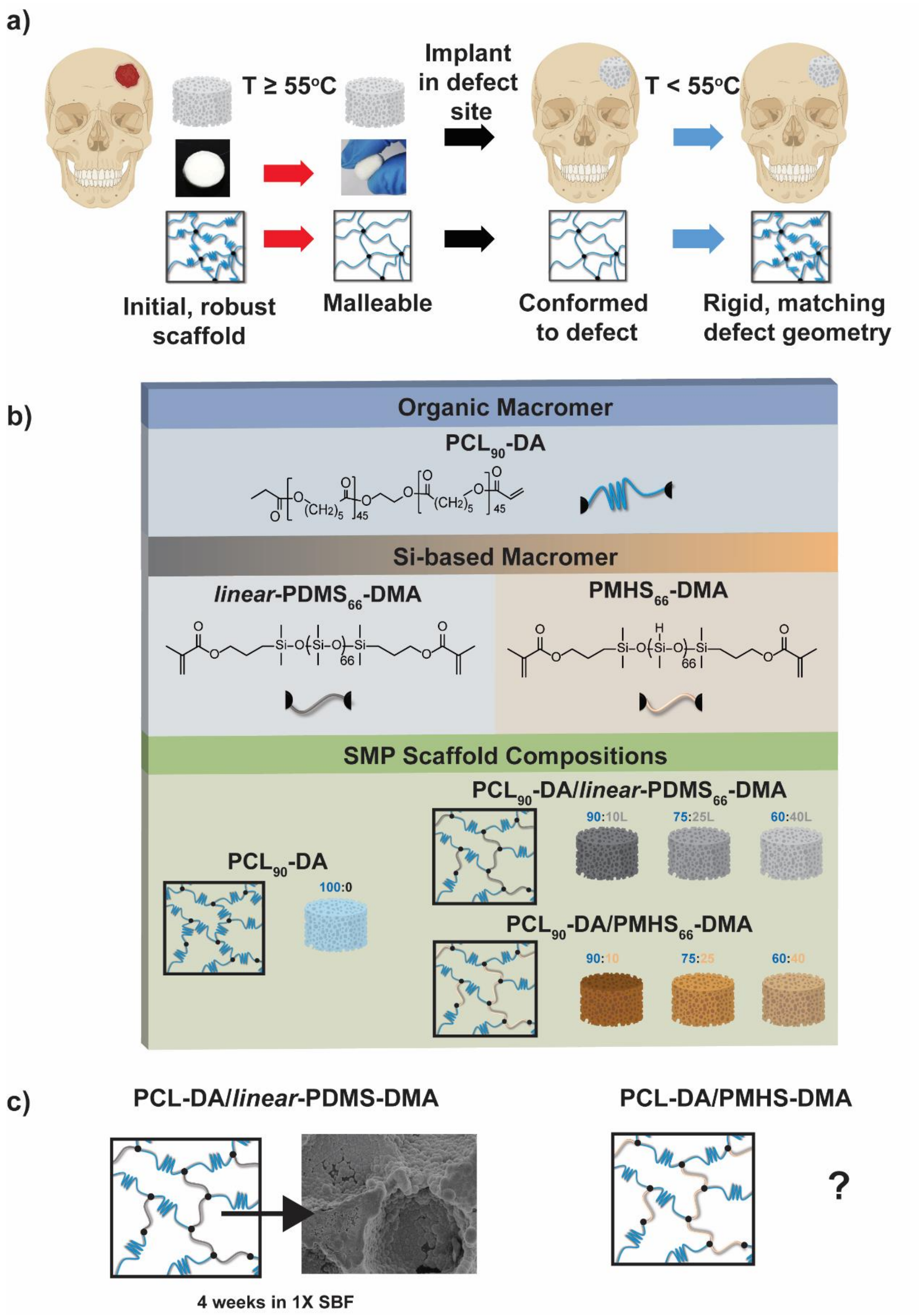

Figure 4-1. (a) PCL-DA scaffolds exhibiting shape memory behavior, conforming to an irregular defect site. (b) Macromers used to form self-fitting SMP scaffolds with varying wt % ratios of PCL to PDMS or PMHS. Schematics are generalized representations of crosslinked network. (c) Mineralization rate of PDMS containing scaffolds *vs* PMHS.

characterized in terms pore size, PCL % crystallinity, shape memory behavior, hydrophilic tendency, and compressive mechanical properties as well as degradation (accelerated and non-accelerated conditions) and bioactivity in 1X SBF. The impact of scaffold mineralization on mechanical properties was also assessed. In evaluating osteogenic potential *in vitro,* PCL-DA control, PCL-DA/*linear*-PDMS-DMA, and PCL-DA/PMHS-DMA scaffolds will be assessed for cytotoxicity, cell distribution and morphology, mineralization staining, and a protein-level immunoassay for osteogenic markers for h-BMSCs.

4.3. Materials and Methods

4.3.1. Materials

Poly(ε-caprolactone) diol (PCL_{90}-diol, M_n ~10k g mol^{-1}), trimethylamine (Et_3N), acryloyl chloride, 4-dimethylaminopyridine (DMAP), 2,2-dimethoxy-2-phenylacetophenone (DMP), 1-vinyl-2-pyrrolidinone (NVP), potassium carbonate (K_2CO_3), sodium hydroxide (NaOH), potassium hydroxide (KOH), sodium chloride (NaCl), octamethylcyclotetrasiloxane (D_4), (D_4^H), triflic acid, hexamethyldisilazane (HMDS), sodium chloride (NaCl), sodium bicarbonate ($NaCO_3$), potassium chloride (KCl), dipotassium m hydrogen phosphate trihydrate ($K_2HPO_4 \cdot 3H_2O$), magnesium chloride hexahydrate ($MgCl_2 \cdot 6H_2O$), calcium chloride ($CaCl_2$), sodium sulfate (Na_2SO_4), phosphate buffered saline (PBS; pH 7.4), and tris(hydroxymethyl)aminomethane were obtained from Sigma-Aldrich. Anhydrous magnesium sulfate ($MgSO_4$), ethylenediaminetetraacetic acid (EDTA), tris-(hydroxymethyl) aminomethane (Trizma base), lithium dodecyl sulfate (LiDS), dithiothreitol (DTT), lithium chloride (LiCl), Formalin solution, Triton X-100, and Halt™ Protease and Phosphatase Inhibitor was obtained from Thermo Fisher Scientific. Tetramethyldisiloxane (tetra-SiH), 1,3-bis(3-methacryloxypropyl)tetramethyldisiloxane, platinum-divinyltetramethyldisiloxane complex in xylene (Karstedt's catalyst) and were obtained from Gelest. Reagent-grade dichloromethane (CH_2Cl_2) and NMR-grade $CDCl_3$ were dried over 4 Å molecular sieves prior to use. Penicillin (10k IU mL^{-1}), and streptomycin (10k µg mL^{-1}) were obtained from Life Technologies. Dulbecco's phosphate buffered saline (DPBS) was obtained from Corning. Heat-inactivated fetal bovine serum (MSC grade; FBS), 1X GlutaMAX, Dulbecco's modified eagle medium (DMEM), and minimum essential medium-α (MEM-α) were obtained from Gibco. Acryloyl PEG-succinimidyl valerate (ACRL-PEG-SVA) was obtained from Laysan Bio, Inc. Alizarin Red S was obtained from Acros Organics. Peptide RGDS was obtained from Bachem. MAGPIX immunoassay was obtained from Luminex, the Luminex human magnetic assay was obtained from R&D Systems, and the Vybrant^{TM} Metabloic Assay Kit and Quant-iT PicoGreen dsDNA Assay was obtained from Invitrogen. Cryopreserved hBMSCs were obtained from three different donors (Texas A&M Institute for Regenerative Medicine).

4.3.2. Synthesis

All reactions were conducted under positive nitrogen (N_2) pressure in oven-dried (120 ºC) glassware, utilizing Teflon-covered magnetic stir bars to agitate reaction mixtures. Chemical structures (including M_n) were verified with ^{1}H NMR spectroscopy (500 MHz spectrometer operating in the FT mode with CDCl3 as the standard). Differential scanning calorimetry (DSC, TA Instruments Q100) was used to characterize the thermal properties of the purified macromers as described below.

PCL-DA. PCL_{90}-DA (i.e. having acrylate end groups) was prepared by acrylate functionalization of PCL_{90}-diol (M_n = ~10k g mol^{-1}; Sigma Aldrich) as previously reported.[102] Briefly, PCL-diol (20.0 g, 2.0 mmol) was dissolved in CH_2Cl_2 (120 mL). DMAP (6.6 mg) was then added as the catalyst. Triethylamine (0.56 mL, 4.0 mmol) and acryloyl chloride (0.65 mL, 8.0

mmol) were added sequentially to the flask, introduced dropwise using a needle and syringe through a rubber septum. The reaction was allowed to stir at room temperature (RT) for 30 min. The crude polymer was purified to obtain PCL-DA (~80% yield). ^{1}H NMR and DSC analyses revealed characteristics consistent with previously reported results. M_n ~10k g mol^{-1}; >90% acrylation; $T_{m,PCL}$ = ~53 ºC; PCL % crystallinity = ~48%.

Linear-PDMS$_{66}$-SiH. Linear-PDMS$_{66}$-SiH (i.e. having silane end groups) (M_n = ~5k g mol^{-1}) was prepared as previous reported.[194] Briefly, D_4 (60.0 g, 202.7 mmol) and tetra-SiH (1.6 g, 12.3 mmol) were reacted by acid-catalyzed ring-opening polymerization (ROP) in the presence of triflic acid (120 μL, 1.35 mmol) overnight (ON) at RT. HMDS (282 μL, 1.35 mmol) was subsequently added and the stirred 1 hr to quench the reaction. The solution was filtered (Ashless, Grade 42) and dried *in vacuo* (RT, ON, 30 in. Hg) to yield a colorless liquid (~72% yield). M_n = ~4125 g mol^{-1}; ^{1}H NMR: ^{1}H NMR (δ, ppm): 0.11 (bm, 411H, SiCH_3), 3.56 (m, 2H, SiH); $T_{g,PDMS}$ = ~ -120 ºC.

Linear-PDMS$_{66}$-DMA. Linear-PDMS$_{66}$-DMA (i.e. having methacrylate end groups) (M_n = ~5k g mol^{-1}) was prepared via hydrosilylation of the terminal silane groups of *linear-PDMS$_{66}$-SiH* with allyl methacrylate, utilizing Karstedt's catalyst according to a previously reported protocol.[194] *Linear-PDMS$_{66}$-SiH* (7.0 g, 1.4 mmol), allyl methacrylate (0.38 g, 3.1 mmol), toluene (35 mL), and Karstedt's catalyst (50 μL) were combined and heated to 90 ºC. The solution was maintained at this temperature for 12 hr, after which the catalyst was removed by refluxing with activated charcoal for ~6 hr. Following filtration, volatiles were removed under vacuum (RT, ON, 30 in. Hg) to isolate the colorless liquid product (~72% yield). M_n = ~4651 g mol^{-1}; ~82% acrylation; ^{1}H NMR (δ, ppm): 0.12 (bm, 421H, SiCH_3), 0.62 (m, 4H, -SiCH_2CH$_2$CH$_2$), ~1.74 (m, 4H, -SiCH$_2$CH_2CH$_2$), 1.98 (m, 6H,

-C(CH_2)(CH_3)), 4.22 (m, 4H, -SiCH_2CH_2CH_2), 5.58 (m, 2H, -C(CH_2)(CH_3)) and 6.27 (m, 2H, -C(CH_2)(CH_3)); $T_{g,PDMS}$ = ~ -120 ºC.

PMHS₆₆-DMA. PMHS$_{66}$-DMA (i.e. having methacrylate end groups) (M_n = ~5k g mol^{-1}) was prepared by D_4^H (60 g, 249.5 mmol) and 1,3-bis(3-methacryloxypropyl)tetramethyldisiloxane (6.0 g, 15.6 mmol) reacted by acid-catalyzed ring-opening polymerization (ROP) in the presence of triflic acid (120 µL, 1.35 mmol) overnight (ON) at RT. The reaction was quenched with HMDS (282 µL, 1.35 mmol) with stirring for 1 hr. The solution was filtered (Ashless, Grade 42) and dried *in vacuo* (RT, ON, 30 in. Hg) to yield a colorless liquid (~78% yield). M_n = ~4587 g mol^{-1}; ~80% acrylation; ^{1}H NMR (δ, ppm): 0.14 (bm, 221H, SiCH_3), 0.66 (m, 4H, - Si$CH_2CH_2CH_2$), 1.78 (m, 4H, -Si$CH_2CH_2CH_2$), 2.02 (m, 6H, -C(CH_2)(CH_3)), 4.17 (m, 4H, -Si$CH_2CH_2CH_2$), 4.78 (s, 67H, Si*H*), 5.51 (m, 2H, -C(CH_2)(CH_3), and 6.15 (m, 2H, -C(CH_2)(CH_3)).; $T_{g,PMHS\text{-}DMA}$ = ~ -135 ºC.

ACRL-PEG-RGDS. ACRL-PEG-RGDS was synthesized as previously reported.[118, 194] Briefly, RGDS was reacted with ACRL-PEG-SVA at a 1:1 molar ratio for 2 h in 50 mM $NaCO_3$. The resulting ACRL-PEG-RGDS product was purified by dialysis and subsequently lyophilized and stored at -20ºC under N_2 until used. ACRL-PEG-RGDS was included in all scaffolds utilized for cell culture at 1 µmol mL^{-1} of precursor solution. ^{1}H NMR analyses were consistent with previously reported results.

4.3.3. SMP Scaffold Fabrication

Porous scaffolds were fabricated via solvent-cast particulate leaching (SCPL) method with a fused salt template to achieve pore interconnectivity as previously reported.[102] Briefly, NaCl particles were sieved (sieve with 425 µm openings) to achieve a size of 459 ± 69 µm. Scanning electron microscopy (SEM; JEOL 6400 SEM, 10kV accelerating voltage) was used in conjunction with imaging software ImageJ® to determine the average size. Sieved salt (10 g) was placed in a 20 mL glass scintillation vial (*I.D.* = 25 mm), to which deionized (DI) water (7.5 wt%) was added in four portions and stirred with a spatula. The hydrated salt was compacted to the bottom of the vial using a blunt glass rod, and the capped vial was then centrifuged (3,220 x *g*, 15 min). The vials were subsequently opened to air-dry (RT, 1 hr), then dried *in vacuo* (RT, 12 hr, 30 in. Hg).

Precursor solutions were prepared with their respective macromer(s) (0.15 g per mL CH_2Cl_2) and 15 vol% of a photoinitiator solution (10 wt% DMP in NVP). The wt% ratios of PCL-DA to *linear*-PDMS-DMA or PMHS-DMA were 90:10, 75:25, and 60:40. Precursor solutions were also formed exclusively with PCL-DA (i.e. 100:0 wt% - control). After vortexing, precursor solution (~5 mL) was promptly added to a prepared salt template. The vials were centrifuged (1,260 x *g*; 10 min), opened and exposed to UV light (UV-Transilluminator; 6 mW cm^{-2}, 365 nm) for 3 min. Following air-drying (RT, 12 hr), the SMP scaffolds were soaked in a water/ethanol mixture (1:1 vol:vol) for ~5 days, removed from vials after day 2, with daily solution changes. The resulting cylindrical scaffolds were allowed to air dry (RT, 12 hr), heat treated *in vacuo* (85 °C, 1 hr, 30 in. Hg) and allowed to rest at RT for 48 hr. The cylindrical scaffolds (*d* ~12 mm) were sliced (*t* ~2 mm) (Vibratome, Leica VT 1000 S) and subsequently biopsy punched (Integra Miltex, *d* ~6 mm). Thus, final scaffold specimen dimensions were *d* ~6 mm x *t* ~2 mm.

4.3.4. SMP Film Fabrication

Analogous SMP solid films were prepared in accordance with a previously reported protocols.[173] The preparation of precursor solutions with corresponding wt% ratios of PCL-DA to *linear*-PDMS-DMA or PMHS-DMA (90:10, 75:25, and 60:40) follows the above method described for SMP scaffold fabrication. The precursor solutions were pipetted into individual circular silicone molds (*d* ~ 45 mm x *t* ~ 2 mm, McMaster-Carr) placed between two glass slides and exposed to UV light (UV-Transilluminator, 6 mW cm^2, 365 nm) for 3 min (1.5 min per side). The resulting solvent-swollen discs were removed from the molds carefully, air dried (RT, 12 hr), and dried *in vacuo* (RT, 4 hr, 30 in. Hg) to ensure adequate solvent removal. Excess material not crosslinked was removed by soaking the discs in ethanol (3 hr). The discs were subsequently air-dried (RT, 12 hr) and heat treated *in vacuo* (85 °C, 1 hr, 30 in. Hg). After resting 48 hr at RT, specimens were subsequently biopsy punched (Integra Miltex, *d* ~5 mm). Final dimensions of film discs were *d* ~5 mm x *t* ~1.1 mm.

4.3.5. Material Characterization

Sol content. Solid film ($N = 3$) or porous scaffold discs ($N = 3$) were weighted and each submerged in 10 mL CH_2Cl_2 within a 20 mL scintillation vial. Sealed vials were placed atop a shaker table (48 hr, 150 rpm). Specimens were removed, rinsed with CH_2Cl_2, air dried (RT, ON), dried *in vacuo* (RT, 24 hr, 30 in. Hg), and weighted. The initial and final weights of specimens were used to determine % sol content

Phase separation. Variances in phase separation (i.e. miscibility) were observed *via* SEM images of cross sections of solid films ($N = 3$). Specimens were subjected to Au-Pt sputter coating (~4 nm) and imaged (JEOL 6400 SEM, 10kV accelerating voltage).

Hydrophilicity. Surface hydrophilicity of films was characterized with static water contact angle (θ_{static}) measurements using a goniometer (CAM-200, KSV Instruments) equipped with an autodispenser, video camera, and drop-shape analysis software (Attention Theta). A sessile DI water droplet (5 μL) was applied to a film and θ_{static} measured at 2 min. The reported θ_{static} values are an average and standard deviation of three measurements ($N = 3$) made on different regions of the same film.

Porosity, pore size and interconnectivity. Percent porosity of scaffolds (*N* = 3) was determined by following equation (1):

$$Porosity\ (\%) = \frac{\rho_{solid\,film} - \rho_{porous\,scaffold}}{\rho_{solid\,film}} * 100 \qquad \textbf{(1)}$$

Scaffold pore size and pore interconnectivity were evaluated via SEM. Scaffold cross-sections were subjected to Au–Pt coating (~4 nm). From the SEM images (*N* = 8) (JEOL 6400, 10kV accelerating voltage), the average pore size was determined from measurements (*N* = 30) pores measured along each image midline with ImageJ software.

PCL T_m and % crystallinity. The PCL melting temperature (T_m) and % crystallinity of each scaffold composition was determined *via* differential scanning calorimetry (DSC, TA Instruments Q100). Specimens (~15 mg, *N* = 3) were individually sealed in hermetic pans and heated at a rate of 5 °C min^{-1} from 27 °C to 200 °C. Measured values were taken from the 2nd DSC cycle to exclude fabrication-induced thermal history. Utilizing the endothermic PCL melt peak, T_m was determined from the maximum point and enthalpy change (ΔH_m) was calculated from the peak area (TA Universal Analysis software). PCL percent crystallinity (% χ_c), with a correction factor accounting for the varying PCL wt% among the compositions, was calculated by equation (2):

$$\%\,\chi_c = \frac{\Delta H_m - \Delta H_c}{\Delta H_m^0 * w} * 100 \qquad \textbf{(2)}$$

where $\Delta H°_m$ as the enthalpy of fusion of theoretical 100% crystalline PCL (139.5 J g^{-1}),[163] and *w* the mass fraction of the PCL (e.g. w = 0.90 for PCL for the 90:10 PCL-DA:*linear*-PDMS$_{66}$-DMA).

Shape memory behavior. Shape memory properties were quantified via strain-controlled cyclic-thermal mechanical compression tests over two cycles (*C*) (TA Instrument Q800 DMA). Scaffolds (*N* = 3) were subjected to the following sequence: (1) after equilibrating at 60 °C for 10 min, compress to a maximum strain (ε_m = 50%) at a rate of 50%/min, (2) hold at ε_m for 5 min and then cool to 25 °C to fix the temporary shape, (3) remove the load and immediately measure ε_u, and (4) reheat to 60 °C to recover the permanent shape, measure the recovered strain (ε_p), and to start the next cycle. The first cycle (C = 0) is referred to as the "pre-cycle" and is followed by C =1. After shape recovery (C = 0), the specimen was cooled to RT and the new dimensions of the pre-cycled specimen was recorded and used for the subsequent cycle C = 1). The shape fixity (R_f) and shape recovery (R_r) for the first (C = 0) and second (C = 1) cycles were calculated using the following equations (3) and (4):

$$R_f(\mathrm{C}) = \frac{\varepsilon_u(C)}{\varepsilon_m} \qquad \textbf{(3)}$$

$$R_r(\mathrm{C}) = \frac{\varepsilon_m - \varepsilon_p(C)}{\varepsilon_m - \varepsilon_p(C-1)} \qquad \textbf{(4)}$$

$\varepsilon_u(C)$ is the ultimate strain in the stress-free state in the fixing process. ε_m is the maximum compressive strain (50%). $\varepsilon_p(C-1)$ and $\varepsilon_p(C)$ are the final strains of the specimen after the two successive cycles in the stress-free state during the shape recovery process. For pre-cycles (C = 0), $\varepsilon_p(-1)$ equals "zero".

Accelerated degradation. Scaffold degradation studies were performed under base-catalyzed conditions (0.2 M NaOH) per ASTM F1635. Specimens (N = 3 per time point) were each immersed in 10 mL of the basic solution in a sealed 20 mL glass scintillation vial and placed in an incubator (VWR Benchtop Shaking Incubator Model 1570) at 37 °C and 60 rpm. At four designated timepoints (24, 48, 72, and 96 hr) specimens were removed, thoroughly rinsed with DI water, blotted, and dried *in vacuo* (RT, 12 hr, 30 in. Hg). The mass of the dried specimen was recorded and compared to their initial mass to determine % mass loss. Specimens were used for a single time point (i.e. not used for subsequent time points).

Non-accelerated Degradation. Scaffold degradation studies were likewise performed as above but under neutral (i.e., non-accelerated) conditions of PBS (pH = 7.4). Specimens ($N = 3$ per time point) were each immersed in 10 mL of neutral solution in a sealed 20 mL glass scintillation vial and maintained in an incubator (37 °C, 60 rpm). At six designated timepoints (2, 4, 6, 8, 10, and 12 weeks) specimens were taken from solution, thoroughly rinsed with DI water, blotted, and dried *in vacuo* (RT, 12 hr, 30 in. Hg). The mass of the dried specimen was recorded and compared to their initial mass to determine % mass loss. Specimens were used for a single time point (i.e. not used for subsequent time points).

Bioactivity. SBF (1X) was prepared as described by Kokubo.[165] Scaffolds ($N = 3$) were each immersed in 20 mL SBF in a sealed centrifuge tube maintained at 37 °C. After 14 and 30 days, specimens were removed, thoroughly rinsed with DI water, blotted, and dried *in vacuo* (RT, 12 hr, 30 in. Hg). Cross-section specimens were prepared by sectioning with a stainless-steel blade and sputtered coated with Au-Pt (~4 nm). FEI Q600 SEM-Energy Dispersive X-ray Spectroscopy (EDS) was utilized to visualize mineralization of HAp.

Compressive mechanical properties. Specimens ($N = 5$) underwent static compression tests (Instron 5944) at RT. A constant strain rate (1.5 mm min^{-1}) was up to 85% strain. From the resulting stress−strain curves, modulus (E) was determined from the slope in the initial linear region ($\leq 10\%\ \varepsilon$). Compressive strength (CS) was determined from the stress at 85% strain. These values were measured also on scaffolds following 30 days exposure to SBF followed by drying *in vacuo* (RT, 24 hr, 30 in. Hg).

Cell Culture. Cryopreserved human bone marrow derived mesenchymal stem cells (hBMSCs) (Texas A&M Institute for Regenerative Medicine) from three different donors were cultured as previously reported.[136, 224] Briefly, cells were thawed and expanded in Minimum

Essential Medium-α (α-MEM) supplemented with 10% MSC-qualified, heat-inactivated fetal bovine serum (FBS) and 1X GlutaMAX in a 37°C-5% CO_2 jacketed incubator. hBMSCs were then transitioned to experimental merium containing Dulbecco's Modified Eagle Medium (DMEM) supplemented with 10% MSC-qualified, heat-inactivated FBS, 1X GlutaMAX, and 1% antibiotic solution (10,000 IU mL^{-1} penicillin, 10,000 μg mL^{-1} streptomycin) 48 hours prior to seeding the scaffolds. Cells from each of the three hBMSC donors were harvested at passage 5-6 and pooled in equal parts immediately prior to seeding on scaffolds.

Seeding and Culture of Scaffolds. Scaffolds for *in vitro* studies were fabricated including 1 μmol mL^{-1} ACRL-PEG-RGDS to promote cellular attachment.[225, 226] These scaffolds (d ~ 9 mm t ~ 2 mm) were press-fit into a plastic model defect (McMaster-Carr, d ~ 8 mm t ~ 2 mm). Scaffolds were dehydrated and sterilized via EtO as previously reported.[224] Before seeding of cells, scaffolds were rehydrated via EtOH and Dulbecco's Phosphate Buffered Saline (DPBS; Corning). Briefly, scaffolds were soaked in 100% EtOH followed by decreasing increments of 25% EtOH in DPBS for 20 min per step until scaffolds were transitioned to 100% DPBS and washed 4 times for 5 min in DPBS. Scaffolds were then placed in blank medium prior to seeding for 1 hour. hBMSCs were seeded onto scaffolds as previously described.[224] Briefly, pooled hBMSCs were pipetted onto the scaffolds at a density of 3.5 x 10^6 cells mL^{-1} in experimental medium in non-tissue culture-treated 24-well plates and placed into a 37°C-5% CO_2 jacketed incubator. After 24 hours, cell-laden scaffolds were then transferred to fresh non-tissue culture-treated 24-well plates in experimental medium to remove nonadherent cells. hBMSCs seeded on PCL-DA scaffolds in experimental medium supplemented with 50 µg mL^{-1} L-ascorbic acid, 10 mM β-glycerophosphate, and 100 nM dexamethasone served as osteogenic controls. All other experimental groups were cultured in un-supplemented experimental medium to assess the intrinsic osteoinductivity of the scaffolds.

Cytotoxicity. Following 48 hours of culture, the non-cytotoxicity of scaffolds was assessed via the Vybrant™ Metabolic Assay Kit (Invitrogen) according to the manufacturer's instructions. Briefly, seeded scaffolds were incubated in 10 μM C_{12}-reazurin for 15 minutes, after which the fluorescence was measured using a Biotek Synergy HTX multimode reader at excitation and emission wavelengths of 563 and 587 nm, respectively. The non-cytotoxicity of the scaffolds was presented relative to the nontoxic PCL-DA growth medium (PCL-DA GM) controls.

MAGPIX Multiplex Immunoassay. Following 14 days of culture, cell-laden scaffolds were lysed and homogenized as previously described.[224] Briefly, scaffolds were rinsed with DPBS without Ca^{2+}/Mg^{2+}, placed in 1.7 mL microfuge tubes, then flash frozen in liquid N_2. Following the addition of ice-cold (4°C) lysis buffer (100 mM Trizma base, 500 mM LiCl, 10 mM EDTA, 1% LiDS, 5 mM DTT, pH~7.8) containing Halt™ Protease and Phosphatase Inhibitor (Thermo Scientific), scaffolds were homogenized using plastic, RNAse-free pestles (VWR) at 4°C, vortexed, then centrifuged. The resultant supernatant was extracted and stored at -80°C for subsequent proteomic analyses. The protein levels of collagen 1 alpha 1 (COL1A1), vascular endothelial growth factor (VEGF), secreted protein acidic and rich in cysteine (SPARC), receptor activator of NF-κB ligand (RANKL), osteopontin (OPN), and bone morphogenetic protein 4 (BMP-4) were measured from lysed sample homogenates using a MAGPIX multiplex immunoassay, as described previously.[224] Sample median fluorescence intensities were assessed via a corresponding standard curve to calculate sample concentrations. Total per-sample DNA content was measured using the Quant-iT™ PicoGreen dsDNA Assay (Invitrogen) according to the manufacturer's instructions. Sample DNA content was utilized to normalize protein expression levels of a per-cell basis.

Western Blot. Western blots were performed to semi-quantitatively compare the expression of proteins associated with chondrogenic (SRY-box transcription factor 9 – SOX9, collagen 2 alpha 1 chain – COL2A1), and adipogenic (CCAAT/enhancer-binding protein α – C/EBP-α, adipocyte fatty acid binding protein – AFABP) differentiation of hBMSCs as previously described.[227] Briefly, concentrated, denatured sample lysates corresponding to 360, 470, and 600 ng DNA (constant within-set sample loading) were added to 10% sodium dodecyl sulfate-polyacrylamide gel electrophoresis (SDS-PAGE) Tris-glycine gels and proteins of interest were separated via electrophoresis. Protein expression levels were assessed through band integrated optical densitometry using Adobe Photoshop CS2 (Version 9.0) and normalized to the loaded DNA amount and to the PCL-DA GM groups. The following antibodies were used: SOX9 (1:500; sc-166505; Santa Cruz Biotechnology), COL2A1 (1:1000; 600-401-104-0.1; Rockland), C/EBP-α (1:500; sc-61; Santa Cruz Biotechnology), and AFABP (1:500; sc-271529; Santa Cruz Biotechnology).

Cell Morphology and Distribution. To assess cell morphology, scaffolds were washed with pre-warmed (37°C) DPBS and fixed with 10% neutral-buffered Formalin solution. Following an additional two DPBS washes, the fixed cells were permeabilized using 0.1% Triton X-100 in DPBS. Cells were then stained with rhodamine phalloidin and DAPI. Confocal fluorescent images of the stained scaffolds were obtained using a Leica SP8 STED microscope (10X objective). Projections were generated from the resultant *z*-stacks using ImageJ.

Calcium Deposition. Following 14 days of culture, calcium deposition was assessed via Alizarin Red S staining as described previously.[224] Briefly, scaffolds were washed twice with DPBS, fixed with 10% neutral-buffered Formalin, washed twice more with DPBS, then stained with 2% w/v Alizarin Red S solution (5 mins; pH = 4.2). After additional DPBS washes, representative images of equivalently stained sections were taken for subsequent qualitative assessment of Alizarin Red S staining. For quantitative analysis, bound Alizarin Red S dye was leached from the stained scaffolds by placing them in a 10% acetic acid solution. Scaffolds were then removed, and the dye/acetic acid solution was neutralized. Solutions from each sample were placed in duplicate in a 96-well plate and absorbance was read at 500 nm (Biotek Synergy HTX multimode reader). The obtained absorbance values were normalized to scaffold weight on a per-sample basis.

Statistical Analyses. Data were reported as a mean ± standard deviation. Values were compared in GraphPad Prism via ANOVA followed by a t-test where a *p*-value of < 0.05 was considered statistically significant.

4.4. Results and Discussion

4.4.1. Fabrication

PCL-DA, PCL-DA/*linear*-PDMS-DMA and PCL/PMHS-DMA scaffolds and films were fabricated successfully following a SCPL and mold casting protocols [102, 173], respectively. Sol content testing was performed on analogous films to determine success of UV crosslinking to form co-matrices (**Table A-16**). PCL-DA control (100:0), PCL/PDMS, and PCL/PMHS compositions all rendered low sol content indicating successful crosslinking (~2-3% scaffolds, ~10-12% films). SEM images of scaffolds confirmed pore interconnectivity, achieved through use of fused salt templates (**Figure A-14**). All compositions exhibited similar pore sizes (~230 μm), which is within the targeted range to support osteogenesis (**Table A-17**). Porosity of scaffolds were found to all be >60% (**Table A-18**). Furthermore, pores were observed to remain rather open along edges of SMP scaffolds (i.e. portion of material in contact with mold perimeter) following self-fitting of the material into a model irregular defect as previously reported.[105]

4.4.2. Hydrophilicity, PCL crystallinity, and shape memory behavior

Given the anticipated effect on shape memory behavior, degradation rates, and mechanical properties, the hydrophilicity (contact angle) and PCL % crystallinity of the various compositions were analyzed (**Table 4-1**). On a structural level, PMHS contains one less methyl pendant group compared to the structure of PDMS, leading to a generation of a more hydrophilic SMP scaffolds in PMHS-containing compositions. Contact angle testing confirms that PMHS-containing compositions exhibited lower contact angle (θ_{static}) values when compared to corresponding PDMS counterparts (**Table 4-1**, **Figure A-15**). Moreover, PCL % crystallinity was determined to predict the relative impact on shape fixity (R_f) and shape recovery (R_r). PCL-DA control scaffolds (100:0) exhibited ~45% crystallinity (T_m ~55 °C). Despite inclusion of PDMS or PMHS segments at varying concentrations, PCL % crystallinity was not substantially altered, nor was T_m significantly impacted at any copolymer ratio. Likely due to their relatively similar PCL % crystallinity, PDMS and PMHS-containing scaffolds all exhibited excellent shape recovery and shape fixity ($\geq$ 94%, C = 1) versus PCL-DA control scaffolds (**Table 4-1**). R_r values for the precycle (C = 0) were

Table 4-1. Contact Angle, % Crystallinity, T_m, Shape Fixity, and Shape Recovery

Matrix Composition	**Contact Angle (°)**	**% crystallinity**	**T_m (°C)**	**R_f (%) $C = 1$**	**R_r (%) $C = 1$**
PCL-DA 100:0	72.5 ± 2.2	47.7 ± 3.2	54.3 ± 1.6	101.1 ± 1.2	99.3 ± 1.1
PCL-DA/ *linear*-PDMS-DMA 90:10L	75.8 ± 1.2	48.1 ± 2.1	56.1 ± 1.1	99.7 ± 1.2	94.3 ± 2.2
PCL-DA/ *linear*-PDMS-DMA 75:25L	96.5 ± 4.2	52.9 ± 0.9	55.1 ± 1.3	100.1 ± 0.2	98.4 ± 3.4
PCL-DA/*linear*-PDMS-DMA 60:40L	112.8 ± 7.4	54.1 ± 1.1	55.3 ± 1.2	99.2 ± 1.2	95.7 ± 1.2
PCL-DA/PMHS-DMA 90:10	73.4 ± 1.3	44.1 ± 4.6	54.2 ± 3.1	99.7 ± 0.8	96.1 ± 1.1
PCL-DA/PMHS-DMA 75:25	77.5 ± 2.2	46.4 ± 1.7	53.2 ± 2.1	97.4 ± 1.2	96.8 ± 0.5
PCL-DA/PMHS-DMA 60:40	97.4 ± 2.3	51.9 ± 2.3	53.4 ± 1.7	98.2 ± 1.5	95.3 ± 1.3

observed to be much lower than the subsequent cycle (*C* = 1), which remains consistent with previous reports that indicate subsequent shape-recovery is improved after an initial cycle removes residual strain originating from scaffold fabrication (**Table A-19**).[20, 178] Across the various compositions and for both cycles, R_f is occasionally reported as being slightly higher than 100% due to an additional compression of up to 0.7% strain (ε). This also remains consistent with prior reports and is thought to be explained by the rapid crystallization of PCL, resulting from the expansion of the initially more compact structure during the cooling process.[20] Another possible explanation for this behavior may be attributed to compression induced crystallization of PCL. Overall, these results indicate that PCL/PMHS scaffolds exhibit shape-memory behavior similar to that of their PCL/PDMS counterparts and PCL-DA controls, and such may be implemented successfully as self-fitting scaffolds. Preconditioning prior to self-fitting is recommended to maximize expansion into a defect via shape memory.

4.4.3. Degradation Rates

Demonstrated in **Figure 4-2**, accelerated (i.e. basic) (**Table A-20**, **Figure A-16**) and non-accelerated (i.e., pH ~7.4) (**Table A-21**, **Figure A-17**) degradation testing were conducted for the various scaffold compositions. Relative rates of degradation were determined to be consistent with previous work performed on PCL/PDMS containing scaffolds, with degradation rates increasing as PDMS content increases (i.e., 100:0 < 90:10L < 75:25L < 60:40L).[105] This trend is also observed in PCL-DA/PMHS-DMA scaffolds, with degradation rates increasing as PMHS wt% increases (i.e., 100:0 < 90:10 < 75:25 < 60:40). As reported previously, despite the hydrophobic nature of silicon-containing polymers, their presence facilitates faster rates of degradation in SMP scaffolds.[105] This is likely related to increases in observed phase separation of higher silicon content compositions. SEM images of analogous film cross-sections (**Figure A-**

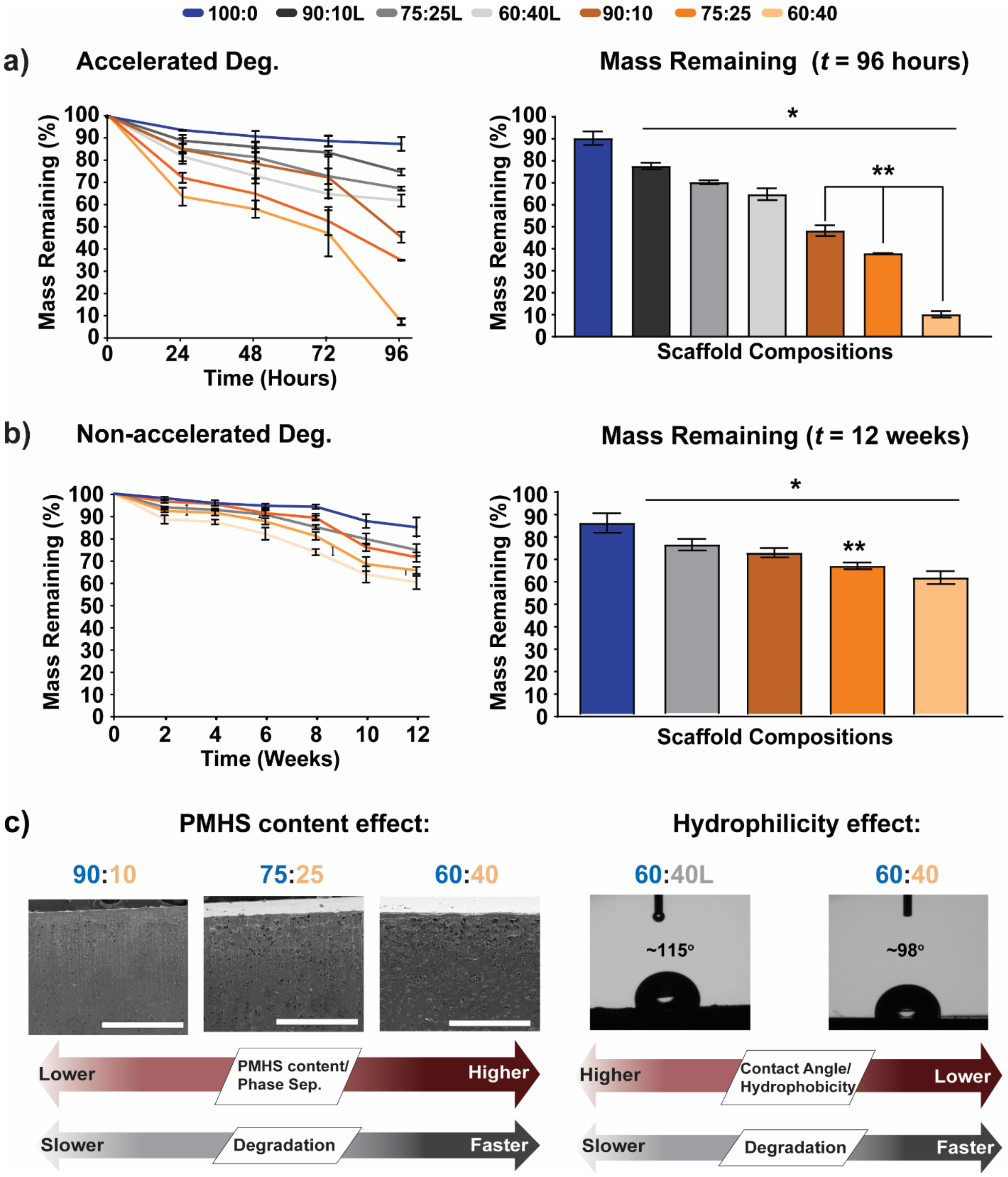

Figure 4-2. (a) Accelerated degradation of scaffolds up to 96 hours. (b) Non-accelerated degradation of scaffolds up to 12 weeks. (c) Effect of PMHS content and hydrophilicity on degradation rates. Scale bar = 500 µm. **p* < 0.05 vs PCL-DA control. ***p* < 0.05 vs PDMS compositions of similar ratio.

18) demonstrate increased roughness topography, indicative of phase separation, which is seen to increase with higher PMHS content. As noted in previous work on semi-IPN PCL-DA/PLLA scaffolds,[173] enhanced water permeability was attributed to a higher degree of phase separation, ultimately contributing to increased rates of hydrolytic degradation.[61, 201, 202] Degradation results also highlight the impact of structural differences between PDMS and PMHS that directly contribute to degradation rates. The loss of a methyl pendent group of PMHS, when compared to PDMS, permits increased hydrophilicity (as demonstrated by decreased contact angle; **Table 4-1**, **Figure A-15**), resulting in greater rates of hydrolytic degradation for PMHS-containing scaffolds. The data confirms this phenomenon, demonstrating that PMHS-containing scaffolds degraded at a significantly faster rate than their relative PDMS wt% counterpart (i.e., 75:25L < 75:25), all of which degraded faster than the PCL control (100:0).

4.4.4. Bioactivity

As previously reported, the inherent bioactivity of PCL-DA/*linear*-PDMS-DMA scaffolds, even with relatively low concentrations of PDMS (e.g. 90:10), is attributed to its silicon component.[105] PMHS shares commonalities with the structure of PDMS, with the difference being that PMHS contains one less methyl pendent group. Thus, in order to determine the impact of the structural differences between PDMS and PMHS containing scaffolds, innate scaffold bioactivity was assessed using a previously reported protocol.[105] Briefly, following exposure to 1X SBF for two weeks, the formation of HAp was assessed via imaging specimen cross-sections (**Figure 4-3**). PCL-DA scaffolds (100:0) and PCL/PDMS scaffolds showed no evidence of mineralization, however all PCL/PMHS scaffolds exhibited substantial mineral deposition along pore walls. The composition of these deposits was confirmed via SEM-EDS to be HAp [$Ca_{10}(PO_4)_6(OH)_2$]. Previous work on PDMS has demonstrated mineralization of PCL/PDMS containing scaffolds

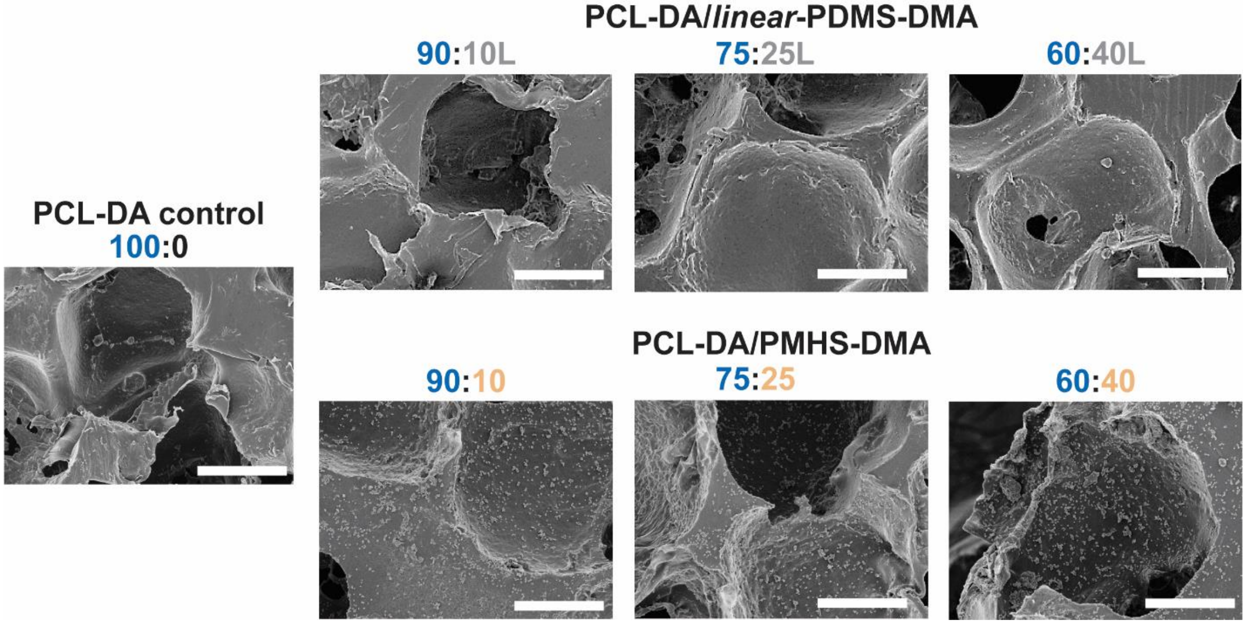

Figure 4-3. SEM images of scaffold cross-sections after 2 weeks in 1X SBF. Scale bar = 150 μm.

after exposure to 1X SBF for one month.[105] By reducing the length of the study, direct comparisons were made between the two compositions to determine which expresses a faster onset of mineralization. Thus, PMHS containing scaffolds were seen to mineralize in half the time (i.e. 2 weeks vs 4 weeks) required for PDMS containing scaffolds of comparable copolymer ratios. This is attributed to the reduction in steric hindrance permitted by the loss of a methyl pendant group between the two polymer structures. Additionally, it is believed that the reduction of hydrophobicity promotes ions suspended in the aqueous SBF to nucleate more readily on the scaffold's surface.

4.4.5. Mechanical properties

Incorporation of low T_g polymers, such as PDMS ($T_{g,PDMS}$ ~ -120°) or PMHS ($T_{g,PMHS}$ ~ -135), into copolymer matrices with PCL-DA is expected to result in a softer overall material, posing as a potential limitation for oseteointegrative applications. Compression testing was conducted on scaffold specimens in order to determine compressive modulus (*E*) (**Figure 4-4**, **Table A-22**) and compressive strength (*CS*) (**Figure A-19**, **Table A-23**). As has been recorded in previous work on PCL/PDMS scaffolds, *E* and *CS* were seen to decrease with increasing PDMS content (i.e., 60:40L < 75:25L < 90:10L < 100:0).[105] Likewise, PMHS containing scaffolds were also seen to decrease in modulus with higher PMHS content (i.e., 60:40 < 75:25 < 90:10 < 100:0). However, the moduli of PDMS-containing and PMHS-containing scaffolds were seen to dramatically increase following mineralization (30 days, 1X SBF, **Figure 4-4**). The modulus of the 90:10L and 75:25L PDMS scaffolds as well as all PMHS containing scaffolds were seen to be

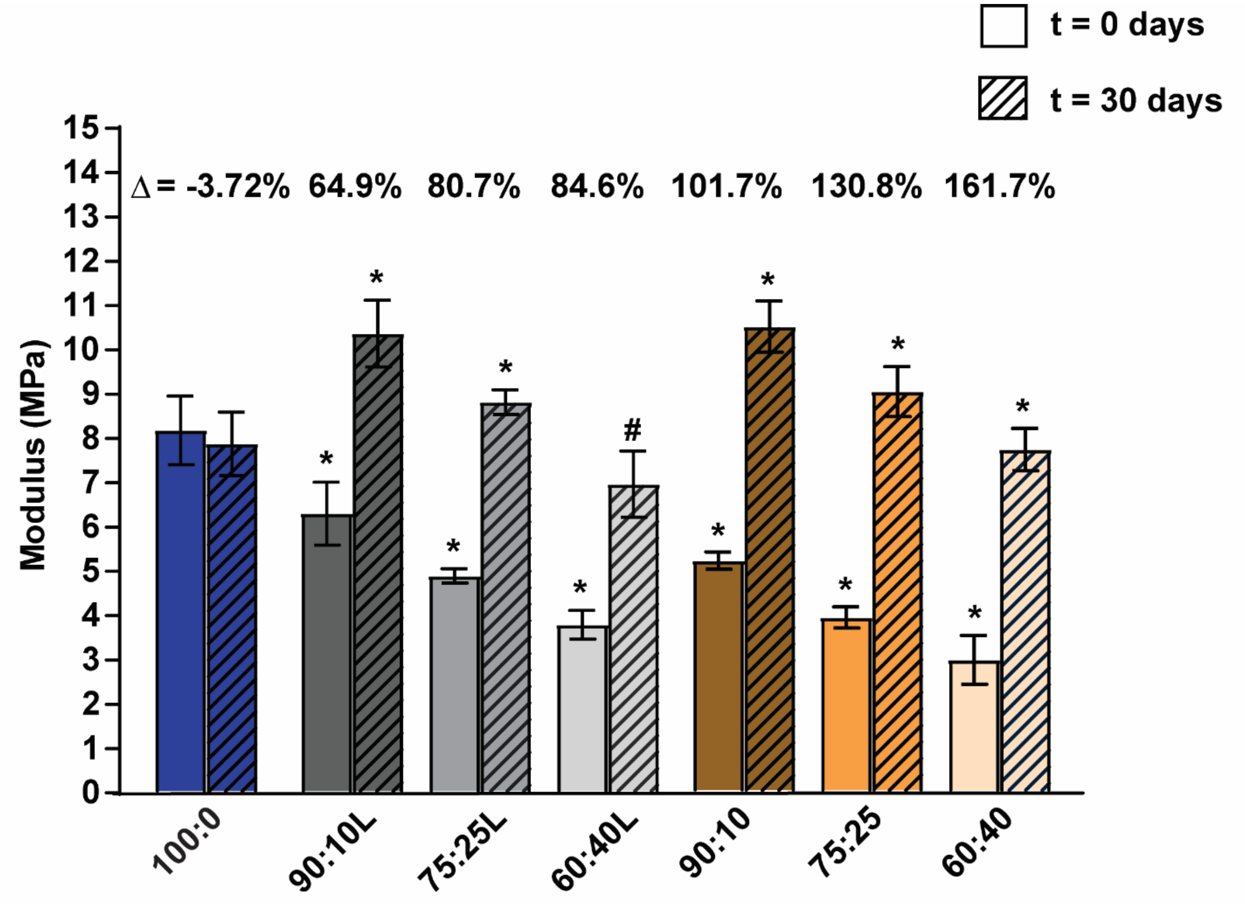

Figure 4-4. Modulus values of scaffolds at $t = 0$ and 30 days in 1 X SBF. *$p < 0.05$ vs PCL-DA control under similar conditions ($t = 0$ or 30). #$p > 0.05$ vs PCL-DA under similar conditions.

statistically greater than the PCL-DA control. The 60:40L composition was seen to have a modulus similar to the PCL-DA control following mineralization. Additionally, the modulus of PMHS containing compositions were seen to exhibit a greater percentage increase when compared to their PDMS wt% analogue. This is thought to be attributed to the earlier onset of mineralization for PMHS containing compositions.

4.4.6. *In vitro* analysis

Scaffold Non-Cytotoxicity, Cell Distribution, and Morphology. Non-cytotoxicity of the selected scaffold formulations was evaluated using the Vybrant™ Metabolic Assay Kit (Invitrogen). The scaffolds formulations tested had no significant effects on hBMSC viability (**Figure A-20, Table A-24**). Notably, all three PMHS formulations tested demonstrated a trend toward increased metabolic activity, with the PMHS 60:40 groups exhibiting significantly increased metabolic activity relative to the PCL-DA GM control. Scaffolds were stained with rhodamine phalloidin and DAPI to observe hBMSC cell morphology and spreading. All formulations demonstrated robust cell adherence and spreading, however, the PDMS groups appeared to better accommodate cell spreading relative to the PMHS groups, as evidenced by the increased rhodamine phalloidin staining (**Figure A-21**).

Scaffold-Induced Osteogenic Marker Expression and Calcium Deposition. The capacity of scaffolds to promote the specific osteogenic lineage progression of and calcium deposition by hBMSCs was compared in the absence of osteogenic supplements to evaluate the intrinsic osteoinductivity of PCL-DA scaffolds with or without siloxane copolymers. PCL-DA scaffolds exposed to osteogenic medium (PCL-DA OM) and un-supplemented, experimental growth medium (PCL-DA GM) were used as positive and negative osteogenic controls, respectively. Following 14 days of culture, the expression levels of key markers associated with hBMSC osteogenic differentiation, including relevant bone extracellular matrix (ECM) proteins (i.e. COL1A1, OPN, SPARC, RANKL), and growth factors (i.e. BMP-4, VEGF) were assessed (**Figure 4-5, Table A-25**). Results suggest that PDMS-containing scaffolds generally demonstrate greater osteoinductivity relative to their PMHS counterparts. hBMSCs cultured in PCL-DA/PMHS-DMA 60:40 scaffolds express significantly lower COL1A1 and SPARC relative to the PCL-DA GM control. Contrarily, hBMSCs cultured in PCL-DA/*linear*-PDMS-DMA 60:40L scaffolds express greater VEGF and OPN relative to the PCL-DA GM control. Both PCL-DA/*linear*-PDMS-DMA 75:25L and 60:40L groups expressed significantly greater BMP-4 than the PCL-DA GM control. All scaffold formulations evaluated demonstrated a trend toward greater RANKL expression relative to both the PCL-DA OM and GM controls, with the 60:40L group reaching statistical significance relative to the PCL-DA GM control.

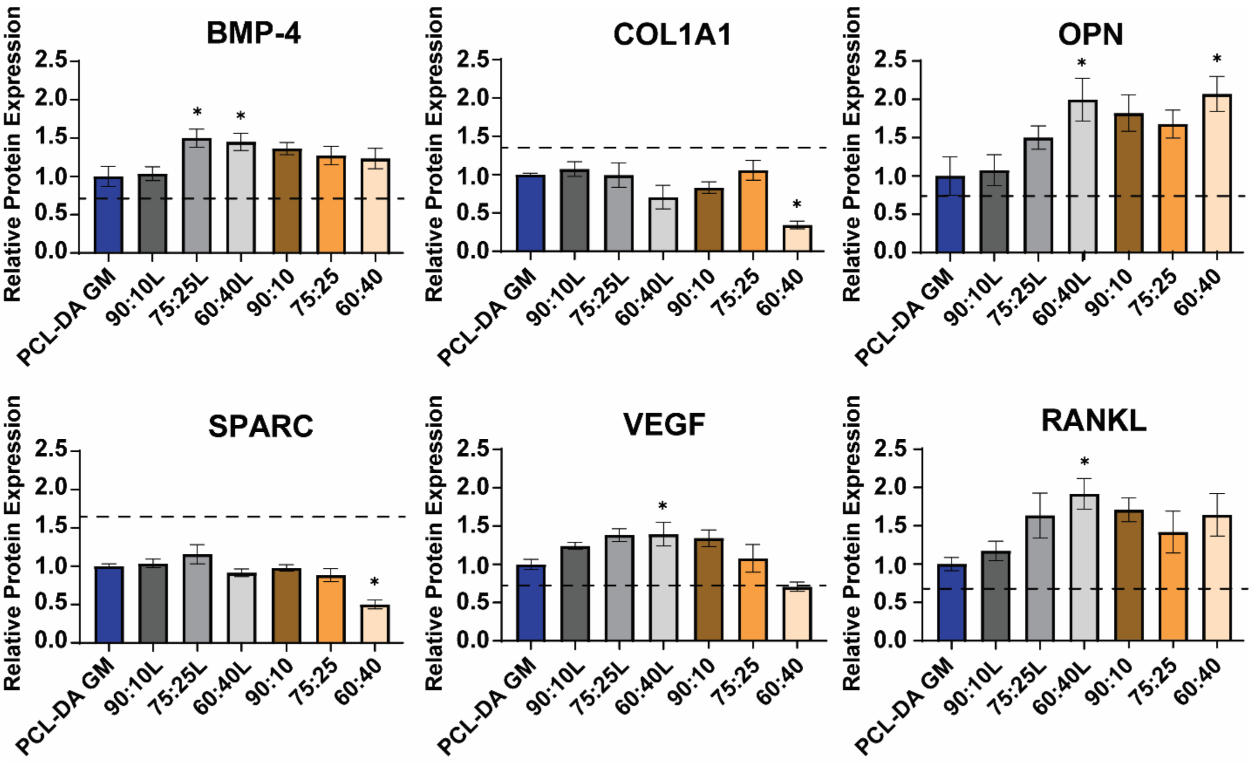

Figure 4-5. Relative osteogenic markers following a 14 day culture of h-MSCs normalized to PCL-DA GM. Dashed line represents PCL-DA OM control. *$p < 0.05$ vs PCL-DA GM control.

To further assess osteogenesis, the calcium deposition of seeded hBMSCs was evaluated both quantitatively and qualitatively via modifications of established methods[228] as described previously.[224] Quantification of Alizarin Red S staining revealed a decrease in calcium deposition with increasing PMHS content, with PMHS 60:40 groups demonstrating a significant reduction in staining relative to the PCL-DA GM controls (**Figure A-22, Table A-26**). Contrarily, no significant differences in calcium deposition were found between any of the tested PDMS formulations and the PCL-DA GM controls. These findings are recapitulated in the representative images of Alizarin Red S-stained scaffold sections (**Figure A-23**) which show a clear reduction in staining with increasing PMHS content.

Scaffold-Induced Off-Target Marker Expression. To assess the specificity of the observed osteogenesis, expression of chondrogenic (i.e. SOX9, COL2A1) and adipogenic (i.e. AFABP, C/EBP-α) markers were evaluated. These showed no significant differences relative to the PCL-DA GM controls (**Figure A-24, Table A-27**). In addition, each of these markers in the PDMS and PHMS groups demonstrated reduce expression relative to positive PCL-DA OM controls, suggesting that the differentiation is at least as specific as that supported by osteogenic medium. Cumulatively, the osteogenic and off-target effects data suggest that PDMS-containing scaffolds may provide a suitable platform for the directed osteogenic differentiation of seeded hBMSCs.

4.5. Conclusions

Herein, towards improving functionality of siloxane-containing PCL-based SMP scaffolds, PMHS-DMA was incorporated in a co-matrix with PCL-DA. These PCL-DA/PMHS-DMA networks were directly compared to previously reported PCL-DA/*linear*-PDMS-DMA networks utilizing similar wt% ratios (90:10, 75:25, and 60:40 (PCL-DA:siloxane)). Both solid films and porous scaffolds were fabricated from aforementioned networks to evaluate changes in properties. It was suspected that modification of siloxane (PDMS (dimethyl) to PMHS (single methyl)) would impact network behavior (e.g. hydrophobicity, degradation rate, and mechanical properties). All network groups were successfully fabricated into solid films (sol content ~10%) and porous scaffolds (sol content ~3%, pore size ~230 µm, and porosity ~70%). Similar to *linear*-PDMS-DMA, PMHS-DMA segments did not impact PCL % crystallinity, shape recovery, or shape fixity. However, PMHS-containing networks did show increased hydrophilic behavior by decreased contact angle (θ_{static}) values versus PDMS-containing counterparts. This property variation expectantly coincided with enhances to hydrolytic degradation rate (accelerated and non-accelerated conditions) for PMHS-containing scaffolds. Furthermore, scaffolds with PMHS were innately bioactive with HAp forming at ~2 weeks opposed to ~4 weeks for PDMS analogues. Similarly to PDMS, PMHS acted as a “softening segment” with decreases to compressive modulus/strength in higher wt% compositions. However, post-mineralization PMHS-containing scaffolds were comparable or surpassed both PCL-DA control and PCL-DA/*linear*-PDMS-DMA counterparts. *In vitro* analysis of 14 day cultured h-MSCs on siloxane-containing scaffolds demonstrated enhancements in osteogenic potential when compared to PCL-DA control. All PDMS and PMHS scaffold exhibited ideal preservation of cell viability with PMHS-containing groups exhibiting an upward trend in viability. This may indicate that the implementation of PMHS at the tested concentrations facilitates the viability and proliferation of hBMSCs under these culture conditions. Likewise, siloxane scaffolds demonstrated suitable levels of osteogenic marker expression (e.g. RANKL) with low off-target expression (e.g. SOX9). While an upregulation in local *in vivo* RANKL expression is indicative of monocytic osteoclastic differentiation and subsequent bone reformation, osteocytes and osteoblasts express RANKL, in part, to maintain bone homeostasis; therefore, the increase in RANKL shown in the PDMS 60:40 group may indicate osteogenic differentiation of the seeded hBMSCs. Moreover, the overall increases in OPN and BMP-4 shown in all groups evaluated here indicates that the tested scaffold formulations are overall osteoinductive relative to the PCL-DA GM controls. While, PCL-DA/PMHS-DMA showed improvements on material behavior (i.e. degradation, post-HAp mechanical properties) vs PDMS groups, both siloxane scaffolds are substantial improvements upon PCL-DA control and are suitable as osteoinductive platforms for CMF bone regeneration.

5. CONCLUSIONS

5.1. Conclusions and Discussion

A regenerative engineering approach to healing irregular CMF bone defects critically relies on a scaffold that enables good contact with adjacent tissues. Thus, the unique ability of “self-fitting” PCL-based SMP scaffolds to conformally fit into irregular defects may improve osseointegration and bone healing. These SMP scaffolds were originally prepared by Grunlan and co-workers as networks from PCL-DA (M_n ~10k g mol^{-1}) and as semi-IPNs from PCL-DA and PLLA (M_n ~10k g mol^{-1}; 75:25 wt% ratio), with the semi-IPNs displaying accelerated degradation. Imparting bioactivity to such self-fitting scaffolds would be expected to improve the regenerative potency. As discussed in Chapter I, bioactive scaffolds enhance regeneration via the formation of HAp (for enhanced bonding to adjacent bone tissue) and also by promoting osteogenic differentiation. Numerous strategies have been explored to impart bioactivity to bone substitutes and scaffolds. Traditionally, these have relied on the incorporation of bioactive glasses and glass ceramics. Alternatively, bioactive PD coatings were applied to PCL-DA and PCL-DA/PLLA semi-IPN scaffolds. But, this surface coating is lost as the scaffold begins to erode. In contrast, Grunlan and co-workers demonstrated that PEG-DA hydrogel scaffolds became bioactive when prepared with PDMS macromers. Thus, in this present work, siloxane polymers were incorporated into PCL-based SMP scaffolds for innate bioactivity.

In Chapter II, the impact of EtO-sterilization to PD-coated PCL-DA and PCL-DA/PLLA (75:25 wt%) semi-IPN scaffolds’ bioactivity and material properties was evaluated. While EtO sterilization is widely used for the sterilization of polymers, including biodegradable polyesters, its utility of PD-coated polyesters was not reported in the literature. Prior to advancing to cell culture or *in vivo* studies, the lack of negative effects on PD-coated scaffolds must be confirmed.

Thus, PCL-DA 100:0 [***Series A***] and semi-IPN PCL-DA/PLLA [***Series B***] scaffolds were prepared as four subgroups: non-coated/non-sterilized (***NC/NS***), coated/non-sterilized (***C/NS***), non-coated/sterilized (***NC/S***), and coated/sterilized (***C/S***). EtO sterilization was conducted at a low operating temperature (~30-35 °C), below that of $T_{m,PCL}$ (~55 ºC), and at a low relative humidity (~35% RH). No changes to morphology (i.e., pore interconnectivity and pore size) were observed. Shape memory behavior was also maintained, and attributed to the lack of change to PCL crystallinity. A lack of change compressive modulus was linked to retention of PCL crystallinity, PLLA crystallinity (***Series B***), and crosslinks. EtO sterilization has been reported to increase surface hydrophobicity. In this work, for ***Series A***, sterilized PD-coated specimens (***C/S***) became slightly more hydrophobic, but remained appreciably more hydrophilic versus non-coated, sterilized specimens (***NC/S***). For ***Series B***, no changes in surface hydrophilicity were observed. Most importantly, indicative of retention of PD-coating bioactivity, all sterilized coated scaffolds (***C/S***) mineralized when exposed to SBF (1X). Degradation behavior was also retained per *in vitro* gravimetric tests done under accelerated (basic) and non-accelerated conditions. Furthermore, under non-accelerated conditions, similar water uptake as well as compressive modulus values was observed for sterilized PD-coated scaffolds (***C/S***) versus those prior to sterilization (***C/NS***). In conclusion, EtO is a suitable method to sterilize PD-coated SMP scaffolds.

In Chapter III, to achieve innate bioactivity in the absence of a PD-coating, PCL/PDMS co-matrices were prepared. Such scaffolds were excepted to increase the rate of biodegradation relative to PCL-DA scaffolds due to phase separation effects, as observed for PCL-DA/PLLA semi-IPN scaffolds. PDMS macromers were selected with varying architectures, affording tunability of PDMS content and crosslink density. Specifically, PCL_{90}-DA was combined with *linear*-$PDMS_{66}$-DMA (5k g mol^{-1}), and *star*-$PDMS_{66}$-TMA (5k g mol^{-1}) at 90:10, 75:25, and 60:40

wt % ratios. Scaffolds were also formed from AcO-PCL_{45}-*b*-$PDMS_{66}$-*b*-PCL_{45}-OAc (65:35 wt % ratio) (10k g mol^{-1}). Scaffolds were successfully formed with interconnected pores and a similar pore size (~230 μm). PCL crystallinity was not substantially impacted by the incorporation of PDMS such that shape memory behavior was retained. Scaffold degradation was assessed both in accelerated (basic) and non-accelerated (neutral) conditions. All PCL/PDMS scaffolds exhibited faster degradation rates versus the PCL-DA control. For scaffolds based on both linear and star PDMS macromers, degradation rates increased with higher PDMS content. The scaffolds prepared with the triblock PDMS macromer degraded the fastest. For scaffolds with similarly high PDMS levels, degradation rates increase in order from: star < linear < triblock (e.g., 60:40S < 60:40L < triblock 65:35) and also coincided with a decreased crosslink density. The observed phase separation of PCL/PDMS compositions (films) is considered the origin of accelerated degradation versus PCL-DA. As hypothesized, PCL/PDMS scaffolds, irrespective of PDMS content, underwent HAp mineralization (one month in 1X SBF). Versus localization of a bioactive coating exclusively to the surface (e.g., a PD coating), the bioactive PDMS component is distributed through the bulk. Thus, throughout erosion, the scaffold bioactivity would be retained. Due to the low T_g of PDMS, PCL/PDMS scaffolds expectedly exhibited lower compressive moduli and strengths versus PCL-DA scaffolds. However, following mineralization, these values increased and, in some cases, exceeded or met that of PCL-DA. Thus, PDMS/PCL SMP scaffolds uniquely afford bioactivity expected to persist during degradation as well as enhanced increased stiffness with mineralization that may provide better mechanical support during healing.

In Chapter IV, the impact of siloxane polymer hydrophobicity on SMP scaffold bioactivity was assessed. Co-matrix SMP scaffolds were formed by combining PCL_{90}-DA with a $PMHS_{66}$-DMA (5k g mol^{-1}) macromer. Analogous scaffolds were prepared with $PDMS_{66}$-DMA (5k g mol^{-}

^{1}), (as in Chapter III). Thus, PMHS$_{66}$-DMA (“monomethyl”) is more hydrophilic versus PDMS$_{66}$-DMA (“dimethyl”). Co-matrices were fabricated, both as porous scaffolds and solid films, by combining PCL$_{90}$-DA with each siloxane macromer at increasing wt% ratios (90:10, 75:25, and 60:40; PCL-DA:siloxane macromer). All scaffolds exhibited similar PCL % crystallinity, as well as shape memory behavior (i.e., recovery and fixity). Per goniometry, PCL/PMHS films expectedly exhibited increased hydrophilicity versus analogous PCL/PDMS films. This led to an increase in the rate of hydrolytic degradation (accelerated and non-accelerated conditions) PCL/PMHS scaffolds. Bioactivity was also enhanced for PCL/PMHS scaffolds, undergoing HAp mineralization in just ~2 weeks as opposed to ~4 weeks for analogous PCL/PDMS. Stemming from their low T_g values, both PMHS$_{66}$-DMA (-120 ºC) and PDMS$_{66}$-DMA (-125 ºC) act as softening segments. Thus, scaffold compressive modulus and strength decreased with increasing siloxane macromer content. However, following HAp mineralization, PCL/PDMS and PCL/PHMS scaffold moduli were similar to or greater than that of the PCL-DA scaffold. h-MSCs cultured (14 days) on siloxane-containing scaffolds demonstrated enhanced in osteogenic potential versus the PCL-DA control. PCL/PMHS and PCL/PDMS scaffolds generally exhibited similar viability, with the PCL/PMHS (60:40) scaffold exhibiting an increase in viability. Likewise, siloxane-containing scaffolds demonstrated enhanced levels of osteogenic marker expression (e.g., RANKL) with low off-target expression (e.g., SOX9). Moreover, in growth media, the increase in OPN and BMP-4 observed for all siloxane-containing scaffolds demonstrated that they are more osteoinductive relative to the PCL-DA. For PCL/PMHS scaffolds, the enhanced osteogenic potentials (versus PCL-DA scaffolds), and accelerated rate of degradation and mineralization (versus PCL-DA and PCL/PDMS scaffolds) may improve their regenerative potential.

In total, this work expands the utility of "self-fitting" SMP scaffolds for the treatment of CMF bone defects. EtO sterilization is indeed suitable for PCL-DA and PCL-DA/PLLA semi-IPN SMPs, included those coated with bioactive PD. However, because PD coatings are lost as scaffolds begin to erode, bioactivity would be diminished. Thus, PCL-based SMP scaffolds with innate bioactivity that is sustained throughout erosion can be achieved by incorporation of siloxane polymers segments. Such PCL/siloxane co-matrix scaffolds also exhibit accelerated degradation rates stemming from phase separation. The properties of the siloxane macromer (e.g., architecture, and hydrophobicity) as well as concentration can be tuned to tailor rate of HAp mineralization, biodegradation, and osteogenic potential of seeded hMSCs

Future Direction

5.1.1. Further Modification to Bioactive Siloxane Polymers

The work reported in this dissertation highlights the importance of achieving bioactivity for polymeric bone regenerative scaffolds. While a variety of methods may be used to achieve this goal (**Figure 1-3**), all conventional techniques (e.g. bioceramic fillers) would negatively impact shape memory function or be rendered ineffective over time (e.g. plasma treatment, PD coatings). Thus, our work investigated the potential of siloxane polymer induced bioactivity and, for the first time, reported this application in PCL-based SMP tissue scaffolds. However, as mentioned in Chapter III and IV, rate of mineralization is another factor that should be considered. Our bioactive PCL-DA/PDMS and PCL-DA/PMHS scaffolds exhibited HAp mineralization at 4 and 2 weeks, respectively. While this is a significant achievement, when compared to mineralization rate of other bioactive materials (e.g. Bioglass®; hours to a few days), these weeks long processes are too slow. A material's rate of mineralization has been directly linked to increases in osteoinductivity

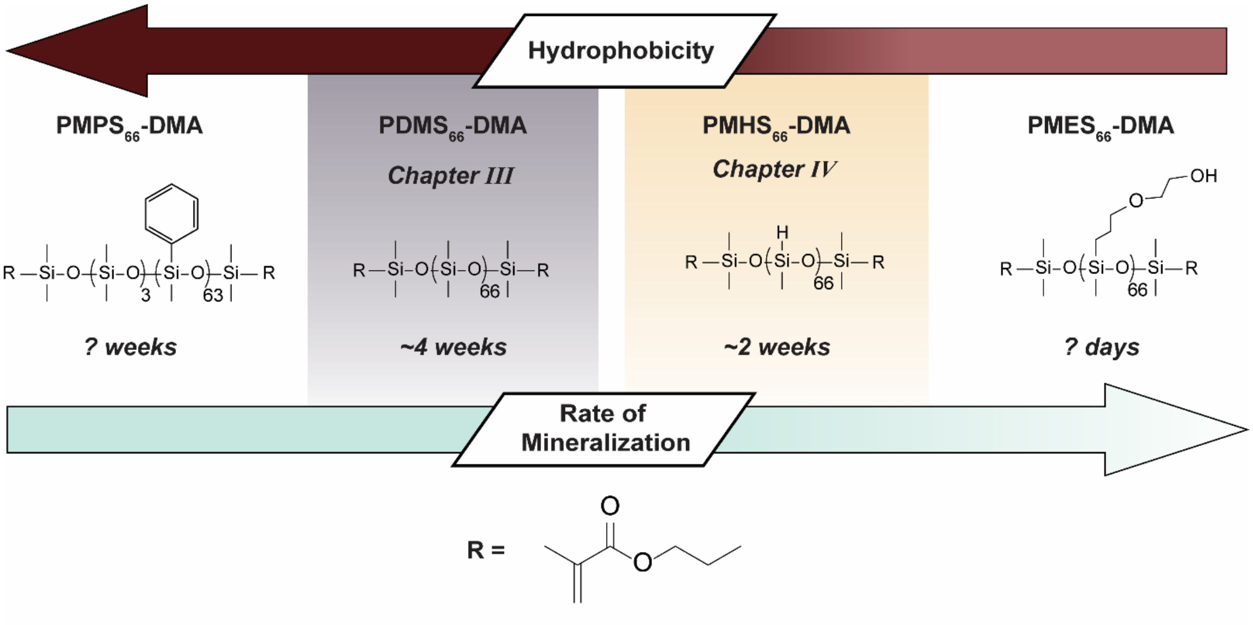

Figure 5-1. Siloxane polymers with pendent group driven changes to hydrophilicity.

and bonding to adjacent bone tissue. Thus, future work should be conducted to enhance mineralization rate.

Further expanding from Chapter IV, an increase in mineralization rate was observed from PDMS to PMHS scaffolds. This was considered to be a result of a decrease in hydrophobicity between siloxane polymers. Inspiration for this investigation comes from the shared characteristic of hydrophilicity among bioactive materials. Furthermore, it was suggested that as the HAp forming ions are suspended in an aqueous solution, increased wettability may promote mineral nucleation. Secondly, it is known that the electron pairs from Oxygen in silicone chains (-Si-O-) act as ion chelated agents. Thus, it was suspected that methyl pendant groups may negatively impact mineralization through steric hinderance. PMHS reduced both hydrophobic and hindering methyl groups, leading to enhanced mineralization rate. Future work should be conducted to probe this behavior further by introduction of siloxanes with varying hydrophobicity in an SMP scaffold.

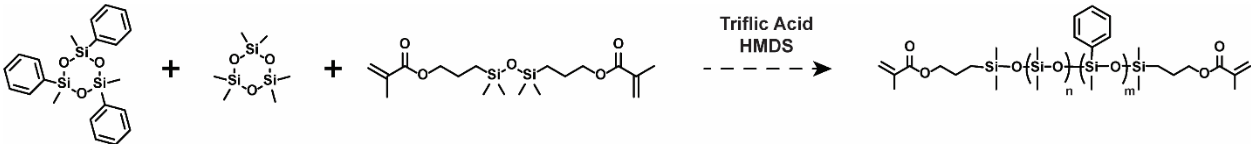

Figure 5-2. Proposed ROP synthesis of PMPS-DMA as a highly hydrophobic siloxane component in a PCL-based co-matrix SMP scaffolds.

We propose that this investigation is conducted utilizing two new siloxane polymers, polymethylphenylsiloxane dimethacrylate ($PMPS_{66}$-DMA) and polymethylethoxyethanolsiloxane dimethacrylate ($PMES_{66}$-DMA). As seen in **Figure 5-1**, both new siloxanes represent two ends of the hydrophobic spectrum. Based on trends established by PDMS and PMHS, it is suspected that PMPS (representing highly hydrophobic) may mineralize at >4 weeks. In contrast, PMES (representing more hydrophilic) may lead to HAp deposits at <2 weeks. If these hypotheses are proven accurate, this may allow further tunability of mineralization rate in siloxane polymers, possibly reaching rates of bioactive glasses. However, consideration must be placed on bulk material properties during siloxane co-matrix formations as previously reported in this dissertation.

PMPS is suspected to reduce mineralization rate due to high levels of hydrophobicity imparted by a phenyl pendant group. Aromatic rings are known to be hydrophobic due to limited electronegativity differences between bonds, leading to a lack of polarity. Incorporating such a ring as a pendant group in a siloxane component of a PCL-DA/siloxane co-matrix would overall increase network hydrophobicity. Thus, we suspect PCL-DA/PMPS-DMA SMP scaffolds have decreased wettability, bioactivity, and hydrolytic degradation rate. Another property to be investigated is mechanical behavior as PMPS likely has a higher T_g than other siloxanes due to bulky side groups. The proposed reaction (**Figure 5-2**) is an acid catalyzed ring-opening polymerization (ROP) of hexamethylhexaphenylcyclotrisiloxane (D^3MePh) and hexamethylcyclotrisiloxane (D^3) simultaneously with capping agent 1,3-bis(3-

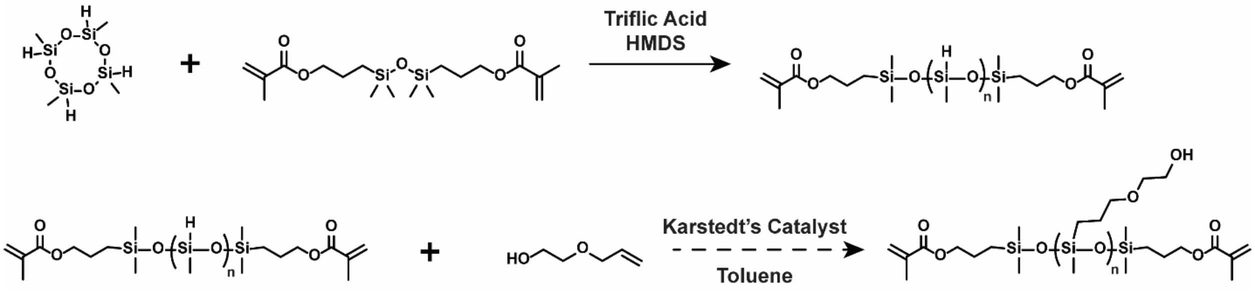

Figure 5-3. Proposed ROP and hydrosilylation synthesis of PMES-DMA as a hydrophilic siloxane component in a PCL-based co-matrix SMP scaffolds.

methacryloxypropyl)tetramethyldisiloxane by triflic acid. Repeat units can be controlled by molar ratios of D^3MePh, D^3, and capping agent.

In a contrasting manner, PMES is suspected to enhance mineralization rate through decreased levels of hydrophobicity imparted by alcohol pendant groups. Inspiration for this generation of siloxane polymer comes from hydrophilic polyethylene glycol (PEG). This polymer has such high levels of hydrophilicity that when crosslinked it forms a hydrogel. Thus, we seek to leverage this effect in a localized way by incorporating the alcohol terminated pendant group to draw water to siloxane chains. This is suspected to further allow chelation of cations from aqueous solutions (e.g. SBF, human blood plasma) thus decreasing time of mineral formation. Thus, we hypothesize that PCL-DA/PMES-DMA SMP scaffolds will have increased wettability, bioactivity, and hydrolytic degradation rate. Special consideration should be given to any excessive degradation rates as scaffolds. While resorption is a critical property for regenerative scaffolds, they must also be able to provide structural support to HAp and cells during initial stages of healing. The proposed reaction (**Figure 5-3**) synthesis follows two steps, 1) ROP of D^4H with capping agent 1,3-bis(3-methacryloxypropyl)tetramethyldisiloxane by triflic acid to make PMHS-DMA, and 2) hydrosilylation of PMHS-DA with 2-allyloxyethanol by platinum-based Karstedt's catalyst. In this way, repeat units of PMES-DMA can be controlled by step 1 mole ratio of D^4H to capping agent.

5.1.2. Pre-treatment of Existing Siloxane Polymers

In further enhancing the bioactive capabilities of existing siloxane-containing SMPs (i.e. PDMS and PMHS generations) investigation to scaffold modifications (post-fabrication) should be conducted. One such idea is that of "pre-treating" or pre-degrading these generations of scaffolds prior to utilization. The reasoning behind this proposed treatment is the suspected degradation products of acrylated end group crosslinks advancing mineralization. Through ester hydrolysis of crosslinks, it is suspected that hydrophilic by-products (i.e. alcohol and carboxylic acid) may aid in increased wettability (**Figure 5-4**). First, degradation products should be identified by pre-treating films and scaffolds of PCL-DA/PDMS-DMA, PCL-DA/PMHS-DMA, PDMS-DMA controls, and PMHS-DMA controls. This should be conducting in basic (i.e. NaOH solution) and neutral (i.e. PBS) conditions as to determine degradation extent of each "treatment solution".

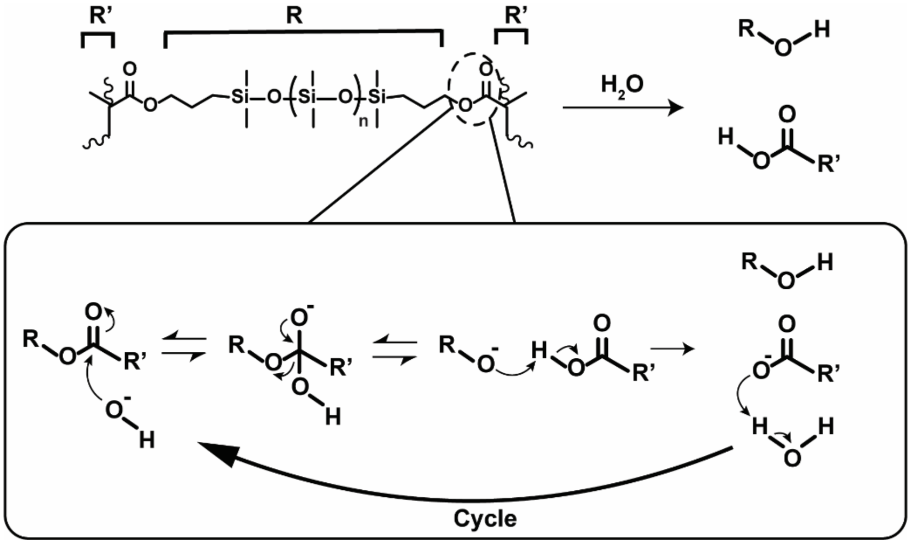

Figure 5-4. Proposed base-catalyzed hydrolysis of crosslinked PDMS with hydrophilic degradation products.

After treatment, films should be tested for changes in hydrophilicity (i.e. contact angle) as well as surface changes through attenuated total reflection Fourier-transform infrared (ATR-FTIR) spectroscopy. In combination, these techniques will allow for in-depth analysis on -OH or other hydrophilic group production through pre-treatment. Following, scaffolds should be submerged in 1X SBF, removed weekly, and checked for HAp mineralization by SEM/SEM-EDS. If established that pre-treated scaffolds mineralize at faster rates, then an extensive material characterization should be conducted. As these materials are being degraded, special consideration should be taken for changes to mechanical properties or shape memory behavior that may be drastically altered. This project can be highly varied by time of treatment, treatment solution basicity, and type of siloxane polymer undergoing treatment. Thus, an investigation into pre-treated siloxane-containing scaffolds may led to enhanced rates of bioactivity and improvements to osteoinductivity.

REFERENCES

1. Clarke, B., Normal bone anatomy and physiology. *Clin. J. Am. Soc. Nephrol.* **2008,** *3 Suppl* (Suppl 3), S131-S139.

2. Yue, S.; He, H.; Li, B.; Hou, T., Hydrogel as a biomaterial for bone tissue engineering: a review. *Nanomaterials* **2020,** *10* (8), 1511.

3. Quinn, J.; McFadden, R.; Chan, C.-W.; Carson, L., Titanium for orthopedic applications: an overview of surface modification to improve biocompatibility and prevent bacterial biofilm formation. *iScience* **2020,** *23* (11), 101745.

4. Apostu, D.; Lucaciu, O.; Berce, C.; Lucaciu, D.; Cosma, D., Current methods of preventing aseptic loosening and improving osseointegration of titanium implants in cementless total hip arthroplasty: a review. *J. Int. Med. Res.* **2018,** *46* (6), 2104-2119.

5. Grosse, S.; Haugland, H. K.; Lilleng, P.; Ellison, P.; Hallan, G.; Høl, P. J., Wear particles and ions from cemented and uncemented titanium-based hip prostheses-a histological and chemical analysis of retrieval material. *J. Biomed. Mater. Res. B Appl. Biomater.* **2015,** *103* (3), 709-17.

6. Niinomi, M.; Nakai, M., Titanium-based biomaterials for preventing stress shielding between implant devices and bone. *Int. J. Biomater.* **2011,** *2011*, 836587.

7. Heary, R. F.; Parvathreddy, N.; Sampath, S.; Agarwal, N., Elastic modulus in the selection of interbody implants. *J. Spine Surg.* **2017,** *3* (2), 163-167.

8. Foletti, J. M.; Lari, N.; Dumas, P.; Compes, P.; Guyot, L., [PEEK customized implant for skull esthetic reconstruction]. *Rev. Stomatol. Chir. Maxillofac.* **2012,** *113* (6), 468-71.

9. Chivers, R. A.; Moore, D. R., The effect of molecular weight and crystallinity on the mechanical properties of injection moulded poly(aryl-ether-ether-ketone) resin. *Polymer* **1994,** *35* (1), 110-116.

10. Alvaredo, Á.; Martín, M. I.; Castell, P.; Guzmán de Villoria, R.; Fernández-Blázquez, J. P., Non-isothermal crystallization behavior of PEEK/graphene nanoplatelets composites from melt and glass states. *Polymers* **2019,** *11* (1).

11. Kurtz, S. M.; Devine, J. N., PEEK biomaterials in trauma, orthopedic, and spinal implants. *Biomaterials* **2007,** *28* (32), 4845-4869.

12. Bathala, L.; Majeti, V.; Rachuri, N.; Singh, N.; Gedela, S., The role of polyether ether ketone (Peek) in dentistry - a review. *J. Med. Life* **2019,** *12* (1), 5-9.

13. Ng, Z. Y.; Nawaz, I., Computer-designed PEEK implants: a peek into the future of cranioplasty? *J. Craniofac. Surg.* **2014,** *25* (1), e55-8.

14. Punchak, M.; Chung, L. K.; Lagman, C.; Bui, T. T.; Lazareff, J.; Rezzadeh, K.; Jarrahy, R.; Yang, I., Outcomes following polyetheretherketone (PEEK) cranioplasty: systematic review and meta-analysis. *J. Clin. Neurosci.* **2017,** *41*, 30-35.

15. Mangano, F.; Mangano, C.; Margiani, B.; Admakin, O., Combining intraoral and face scans for the design and fabrication of computer-assisted design/computer-assisted manufacturing (CAD/CAM) polyether-ether-ketone (PEEK) implant-supported bars for maxillary overdentures. *Scanning* **2019,** *2019*, 4274715-4274715.

16. Papathanasiou, I.; Kamposiora, P.; Papavasiliou, G.; Ferrari, M., The use of PEEK in digital prosthodontics: a narrative review. *BMC Oral Health* **2020,** *20* (1), 217.

17. Feng, X.; Ma, L.; Liang, H.; Liu, X.; Lei, J.; Li, W.; Wang, K.; Song, Y.; Wang, B.; Li, G.; Li, S.; Yang, C., Osteointegration of 3D-printed fully porous polyetheretherketone scaffolds with different pore sizes. *ACS Omega* **2020,** *5* (41), 26655-26666.

18. Haleem, A.; Javaid, M., Polyether ether ketone (PEEK) and its 3D printed implants applications in medical field: an overview. *Clin. Epidemiol. Glob. Health* **2019,** *7* (4), 571-577.

19. Mao, A. S.; Mooney, D. J., Regenerative medicine: current therapies and future directions. *Proc. Natl. Acad. Sci. USA* **2015,** *112* (47), 14452-14459.

20. Zhang, D.; Burkes, W. L.; Schoener, C. A.; Grunlan, M. A., Porous inorganic–organic shape memory polymers. *Polymer* **2012,** *53* (14), 2935-2941.

21. Augustine, R.; Kalarikkal, N.; Thomas, S., Advancement of wound care from grafts to bioengineered smart skin substitutes. *Prog. Biomater.* **2014,** *3* (2-4), 103-113.

22. Leal, B. B. J.; Wakabayashi, N.; Oyama, K.; Kamiya, H.; Braghirolli, D. I.; Pranke, P., Vascular tissue engineering: Polymers and methodologies for small caliber vascular grafts. *Front. Cardiovasc. Med.* **2021,** *7* (376).

23. Amini, A. R.; Laurencin, C. T.; Nukavarapu, S. P., Bone tissue engineering: recent advances and challenges. *Crit. Rev. Biomed. Eng.* **2012,** *40* (5), 363-408.

24. Albrektsson, T.; Johansson, C., Osteoinduction, osteoconduction and osseointegration. *Eur. Spine J.* **2001,** *10 Suppl 2* (Suppl 2), S96-101.

25. Du, Y.; Guo, J. L.; Wang, J.; Mikos, A. G.; Zhang, S., Hierarchically designed bone scaffolds: from internal cues to external stimuli. *Biomaterials* **2019,** *218*, 119334.

26. Stevens, M. M., Biomaterials for bone tissue engineering. *Mater. Today* **2008,** *11* (5), 18-25.

27. Yu, X.; Tang, X.; Gohil, S. V.; Laurencin, C. T., Biomaterials for bone regenerative engineering. *Adv. Healthc. Mater.* **2015,** *4* (9), 1268-85.

28. Cozza, N.; Monte, F.; Bonani, W.; Aswath, P.; Motta, A.; Migliaresi, C., Bioactivity and mineralization of natural hydroxyapatite from cuttlefish bone and bioglass® co-sintered bioceramics. *J. Tissue Eng. Regen. Med.* **2018,** *12* (2), e1131-e1142.

29. Roberts, T. T.; Rosenbaum, A. J., Bone grafts, bone substitutes and orthobiologics: the bridge between basic science and clinical advancements in fracture healing. *Organogenesis* **2012,** *8* (4), 114-124.

30. Frantz, C.; Stewart, K. M.; Weaver, V. M., The extracellular matrix at a glance. *J. Cell Sci.* **2010,** *123* (24), 4195-4200.

31. Lin, X.; Patil, S.; Gao, Y.-G.; Qian, A., The bone extracellular matrix in bone formation and regeneration. *Frontiers Pharmacol.* **2020,** *11*, 757-757.

32. Ravindran, S.; Gao, Q.; Kotecha, M.; Magin, R. L.; Karol, S.; Bedran-Russo, A.; George, A., Biomimetic extracellular matrix-incorporated scaffold induces osteogenic gene expression in human marrow stromal cells. *Tissue Eng. Part A* **2011,** *18* (3-4), 295-309.

33. Tomoaia, G.; Pasca, R.-D., On the collagen mineralization. a review. *Clujul Med.* **2015,** *88* (1), 15-22.

34. Itoh, S.; Kikuchi, M.; Koyama, Y.; Matumoto, H. N.; Takakuda, K.; Shinomiya, K.; Tanaka, J., Development of a novel biomaterial, hydroxyapatite/collagen (HAp/Col) composite for medical use. *Biomed. Mater. Eng.* **2005,** *15* (1-2), 29-41.

35. Jeong, J.; Kim, J. H.; Shim, J. H.; Hwang, N. S.; Heo, C. Y., Bioactive calcium phosphate materials and applications in bone regeneration. *Biomater. Res.* **2019,** *23* (1), 4.

36. Ronca, A.; Ambrosio, L.; Grijpma, D. W., Design of porous three-dimensional PDLLA/nano-hap composite scaffolds using stereolithography. *J. Appl. Biomater. Funct. Mater.* **2012,** *10* (3), 249-58.

37. Suchanek, W.; Yoshimura, M., Processing and properties of hydroxyapatite-based biomaterials for use as hard tissue replacement implants. *J. Mater. Res.* **1998,** *13* (1), 94-117.

38. Vinodhini, S. P.; Manonmani, R.; Venkatachalapathy, B.; Sridhar, T. M., Interlayer TiO2–HAP composite layer for biomedical applications. *RSC Advances* **2016,** *6* (67), 62344-62355.

39. Buyuksungur, S.; Endogan Tanir, T.; Buyuksungur, A.; Bektas, E. I.; Torun Kose, G.; Yucel, D.; Beyzadeoglu, T.; Cetinkaya, E.; Yenigun, C.; Tönük, E.; Hasirci, V.; Hasirci, N., 3D printed poly(ε-caprolactone) scaffolds modified with hydroxyapatite and poly(propylene fumarate) and their effects on the healing of rabbit femur defects. *Biomater. Sci.* **2017,** *5* (10), 2144-2158.

40. Xu, S.; Liu, J.; Zhang, L.; Yang, F.; Tang, P.; Wu, D., Effects of HAp and TCP in constructing tissue engineering scaffolds for bone repair. *J. Mater. Chem. B* **2017,** *5* (30), 6110-6118.

41. Manolagas, S. C., Birth and death of bone cells: Basic regulatory mechanisms and implications for the pathogenesis and treatment of osteoporosis. *Endo. Rev.* **2000,** *21* (2), 115-137.

42. Miller, S. C.; de Saint-Georges, L.; Bowman, B. M.; Jee, W. S., Bone lining cells: structure and function. *Scanning Microsc.* **1989,** *3* (3), 953-60; discussion 960-1.

43. Boyce, B. F.; Xing, L., Functions of RANKL/RANK/OPG in bone modeling and remodeling. *Arch. Biochem. Biophys.* **2008,** *473* (2), 139-146.

44. Hu, K.; Olsen, B. R., The roles of vascular endothelial growth factor in bone repair and regeneration. *Bone* **2016,** *91*, 30-8.

45. Kawane, T.; Qin, X.; Jiang, Q.; Miyazaki, T.; Komori, H.; Yoshida, C. A.; Matsuura-Kawata, V. K. d. S.; Sakane, C.; Matsuo, Y.; Nagai, K.; Maeno, T.; Date, Y.; Nishimura, R.; Komori, T., Runx2 is required for the proliferation of osteoblast progenitors and induces proliferation by regulating Fgfr2 and Fgfr3. *Sci. Rep.* **2018,** *8* (1), 13551.

46. Ribeiro, N.; Sousa, S. R.; Brekken, R. A.; Monteiro, F. J., Role of SPARC in bone remodeling and cancer-related bone metastasis. *J. Cell Biochem.* **2014,** *115* (1), 17-26.

47. Si, J.; Wang, C.; Zhang, D.; Wang, B.; Zhou, Y., Osteopontin in bone metabolism and bone diseases. *Med. Sci. Monit.* **2020,** *26*, e919159-e919159.

48. Truong, L.-H.; Kuliwaba, J. S.; Tsangari, H.; Fazzalari, N. L., Differential gene expression of bone anabolic factors and trabecular bone architectural changes in the proximal femoral shaft of primary hip osteoarthritis patients. *Arthritis Res. Therapy* **2006,** *8* (6), R188.

49. Wang, R. N.; Green, J.; Wang, Z.; Deng, Y.; Qiao, M.; Peabody, M.; Zhang, Q.; Ye, J.; Yan, Z.; Denduluri, S.; Idowu, O.; Li, M.; Shen, C.; Hu, A.; Haydon, R. C.; Kang, R.; Mok, J.; Lee, M. J.; Luu, H. L.; Shi, L. L., Bone morphogenetic protein (BMP) signaling in development and human diseases. *Genes & Diseases* **2014,** *1* (1), 87-105.

50. Gao, C.; Peng, S.; Feng, P.; Shuai, C., Bone biomaterials and interactions with stem cells. *Bone Res.* **2017,** *5* (1), 17059.

51. Rolvien, T.; Barbeck, M.; Wenisch, S.; Amling, M.; Krause, M., Cellular mechanisms responsible for success and failure of bone substitute materials. *Int. J. Mol. Sci.* **2018,** *19* (10), 2893.

52. Alsberg, E.; Hill, E. E.; Mooney, D. J., Craniofacial tissue engineering. *Crit. Rev. Oral Biol. Med.* **2001,** *12* (1), 64-75.

53. Clementini, M.; Morlupi, A.; Agrestini, C.; Ottria, L., Success rate of dental implants inserted in autologous bone graft regenerated areas: a systematic review. *Oral Implantol.* **2011,** *4* (3-4), 3-10.

54. Neovius, E.; Engstrand, T., Craniofacial reconstruction with bone and biomaterials: review over the last 11 years. *J. Plastic Recon. Aesthetic Surg.* **2010,** *63* (10), 1615-1623.

55. Procopio, O.; Trojan, D.; Frigo, A. C.; Paolin, A., Use of homologous bone for alveolar crest reconstruction in 483 patients with 5 years' outcomes post implantation. *Oral Maxillofac. Surg.* **2019,** *23* (3), 353-363.

56. Triplett, R. G.; Schow, S. R., Autologous bone grafts and endosseous implants: complementary techniques. *J. Oral Maxillofac. Surg.* **1996,** *54* (4), 486-94.

57. Bae, E.-B.; Kim, H.-J.; Ahn, J.-J.; Bae, H.-Y.; Kim, H.-J.; Huh, J.-B., Comparison of bone regeneration between porcine-derived and bovine-derived xenografts in rat calvarial defects: a non-inferiority study. *Materials* **2019,** *12* (20), 3412.

58. Ding, Y.; Wang, L.; Su, K.; Gao, J.; Li, X.; Cheng, G., Horizontal bone augmentation and simultaneous implant placement using xenogeneic bone rings technique: a retrospective clinical study. *Sci. Rep.* **2021,** *11* (1), 4947.

59. Bracey, D. N.; Seyler, T. M.; Jinnah, A. H.; Smith, T. L.; Ornelles, D. A.; Deora, R.; Parks, G. D.; Van Dyke, M. E.; Whitlock, P. W., A porcine xenograft-derived bone scaffold is a biocompatible bone graft substitute: an assessment of cytocompatibility and the alpha-gal epitope. *Xenotransplantation* **2019,** *26* (5), e12534.

60. Haugen, H. J.; Lyngstadaas, S. P.; Rossi, F.; Perale, G., Bone grafts: which is the ideal biomaterial? *J. Clin. Periodontol.* **2019,** *46* (S21), 92-102.

61. Zhang, H.; Yang, L.; Yang, X.-G.; Wang, F.; Feng, J.-T.; Hua, K.-C.; Li, Q.; Hu, Y.-C., Demineralized bone matrix carriers and their clinical applications: an overview. *Orthop. Surg.* **2019,** *11* (5), 725-737.

62. Urist, M. R. J. S., Bone: formation by autoinduction. *Science* **1965,** *150* (3698), 893-899.

63. Drosos, G. I.; Touzopoulos, P.; Ververidis, A.; Tilkeridis, K.; Kazakos, K., Use of demineralized bone matrix in the extremities. *World J. Orthop.* **2015,** *6* (2), 269-277.

64. Gruskin, E.; Doll, B. A.; Futrell, F. W.; Schmitz, J. P.; Hollinger, J. O., Demineralized bone matrix in bone repair: history and use. *Adv. Drug Deliv. Rev.* **2012,** *64* (12), 1063-1077.

65. Elsalanty, M. E.; Genecov, D. G., Bone grafts in craniofacial surgery. *Craniomaxillofac. Trauma Reconstr.* **2009,** *2* (3), 125-134.

66. Brink, O., The choice between allograft or demineralized bone matrix is not unambiguous in trauma surgery. *Injury* **2021,** *52*, S23-S28.

67. Shehadi, J. A.; Elzein, S. M., Review of commercially available demineralized bone matrix products for spinal fusions: a selection paradigm. *Surg. Neurol. Int.* **2017,** *8*, 203-203.

68. Krishnan, V.; Lakshmi, T., Bioglass: a novel biocompatible innovation. *J. Adv. Pharm. Technol. Res.* **2013,** *4* (2), 78-83.

69. Andersson, Ö. H.; Karlsson, K. H.; Kangasniemi, K., Calcium phosphate formation at the surface of bioactive glass in vivo. *J. Non-Cryst. Solids* **1990,** *119* (3), 290-296.

70. Hench, L. L.; Wilson, J. J. S., Surface-active biomaterials. *Science* **1984,** *226* (4675), 630-636.

71. Wallace, K. E.; Hill, R. G.; Pembroke, J. T.; Brown, C. J.; Hatton, P. V., Influence of sodium oxide content on bioactive glass properties. *J. Mater. Sci. Mater. Med.* **1999,** *10* (12), 697-701.

72. Froum, S. J.; Weinberg, M. A.; Tarnow, D. J. J. o. p., Comparison of bioactive glass synthetic bone graft particles and open debridement in the treatment of human periodontal defects. a clinical study. *J. Periodontol.* **1998,** *69*, 698-709.

73. Ginebra, M.-P.; Espanol, M.; Maazouz, Y.; Bergez, V.; Pastorino, D., Bioceramics and bone healing. *EFORT Open Rev.* **2018,** *3* (5), 173-183.

74. Carrow, J. K.; Di Luca, A.; Dolatshahi-Pirouz, A.; Moroni, L.; Gaharwar, A. K., 3D-printed bioactive scaffolds from nanosilicates and PEOT/PBT for bone tissue engineering. *Regen. Biomater.* **2019,** *6* (1), 29-37.

75. Carrow, J. K.; Cross, L. M.; Reese, R. W.; Jaiswal, M. K.; Gregory, C. A.; Kaunas, R.; Singh, I.; Gaharwar, A. K., Widespread changes in transcriptome profile of human mesenchymal stem cells induced by two-dimensional nanosilicates. *Proc. Natl. Acad. Sci. USA* **2018,** *115* (17), E3905-e3913.

76. Gaharwar, A. K.; Mihaila, S. M.; Swami, A.; Patel, A.; Sant, S.; Reis, R. L.; Marques, A. P.; Gomes, M. E.; Khademhosseini, A., Bioactive silicate nanoplatelets for osteogenic differentiation of human mesenchymal stem cells. *Adv. Mater.* **2013,** *25* (24), 3329-36.

77. Mohamad Yunos, D.; Bretcanu, O.; Boccaccini, A. R., Polymer-bioceramic composites for tissue engineering scaffolds. *J. Mater. Sci.* **2008,** *43* (13), 4433-4442.

78. Crespy, D.; Bozonnet, M.; Meier, M., 100 Years of bakelite, the material of a 1000 uses. *Angew. Chem. Int. Ed.* **2008,** *47* (18), 3322-3328.

79. Heath, D. E.; Cooper, S. L., The development of polymeric biomaterials inspired by the extracellular matrix. *J. Biomater. Sci. Poly. Ed.* **2017,** *28* (10-12), 1051-1069.

80. Kohane, D. S.; Langer, R., Polymeric biomaterials in tissue engineering. *Pediatr. Res.* **2008,** *63* (5), 487-491.

81. Liechty, W. B.; Kryscio, D. R.; Slaughter, B. V.; Peppas, N. A., Polymers for drug delivery systems. *Annu. Rev. Chem. Biomol. Eng.* **2010,** *1*, 149-173.

82. Ghassemi, T.; Shahroodi, A.; Ebrahimzadeh, M. H.; Mousavian, A.; Movaffagh, J.; Moradi, A., Current concepts in scaffolding for bone tissue engineering. *Arch. Bone Jt. Surg.* **2018,** *6* (2), 90-99.

83. Collins, M. N.; Ren, G.; Young, K.; Pina, S.; Reis, R. L.; Oliveira, J. M., Scaffold fabrication technologies and structure/function properties in bone tissue engineering. *Adv. Funct. Mater.* **2021,** *31* (21), 2010609.

84. Lee, H.; Dellatore, S. M.; Miller, W. M.; Messersmith, P. B., Mussel-inspired surface chemistry for multifunctional coatings. *Science* **2007,** *318* (5849), 426-430.

85. Murari, G.; Bock, N.; Zhou, H.; Yang, L.; Liew, T.; Fox, K.; Tran, P. A., Effects of polydopamine coatings on nucleation modes of surface mineralization from simulated body fluid. *Sci. Rep.* **2020,** *10* (1), 14982.

86. Aronsson, B. O.; Lausmaa, J.; Kasemo, B., Glow discharge plasma treatment for surface cleaning and modification of metallic biomaterials. *J. Biomed. Mater. Res.* **1997,** *35* (1), 49-73.

87. Ortiz-Ortega, E.; Hosseini, S.; Martinez-Chapa, S. O.; Madou, M. J., Aging of plasma-activated carbon surfaces: challenges and opportunities. *Appl. Surface Sci.* **2021,** *565*, 150362.

88. Tanahashi, M.; Yao, T.; Kokubo, T.; Minoda, M.; Miyamoto, T.; Nakamura, T.; Yamamura, T., Apatite coated on organic polymers by biomimetic process: Improvement in its adhesion to substrate by glow-discharge treatment. *J. Biomed. Mater. Res.* **1995,** *29* (3), 349-357.

89. Baino, F.; Yamaguchi, S., The use of simulated body fluid (SBF) for assessing materials bioactivity in the context of tissue engineering: review and challenges. *Biomimetics* **2020,** *5* (4), 57.

90. Chen, X.; Nouri, A.; Li, Y.; Lin, J.; Hodgson, P. D.; Wen, C., Effect of surface roughness of Ti, Zr, and TiZr on apatite precipitation from simulated body fluid. *Biotechnol. Bioeng.* **2008,** *101* (2), 378-87.

91. Dumas, J. E.; Zienkiewicz, K.; Tanner, S. A.; Prieto, E. M.; Bhattacharyya, S.; Guelcher, S. A., Synthesis and characterization of an injectable allograft bone/polymer composite bone void filler with tunable mechanical properties. *Tissue Eng. Part A* **2010,** *16* (8), 2505-2518.

92. Wang, T.; Yang, X.; Qi, X.; Jiang, C., Osteoinduction and proliferation of bone-marrow stromal cells in three-dimensional poly (ε-caprolactone)/ hydroxyapatite/collagen scaffolds. *Journal of Translational Medicine* **2015,** *13* (1), 152.

93. Wei, G.; Ma, P. X., Structure and properties of nano-hydroxyapatite/polymer composite scaffolds for bone tissue engineering. *Biomaterials* **2004,** *25* (19), 4749-4757.

94. Nguyen, T. T.; Hoang, T.; Can, V. M.; Ho, A. S.; Nguyen, S. H.; Nguyen, T. T. T.; Pham, T. N.; Nguyen, T. P.; Nguyen, T. L. H.; Thi, M. T. D., In vitro and in vivo tests of PLA/d-HAp nanocomposite. *Adv. Nat. Sci. Nanosci. Nanotechnol.* **2017,** *8* (4), 045013.

95. Zhang, R.; Ma, P. X., Poly(α-hydroxyl acids)/hydroxyapatite porous composites for bone-tissue engineering. preparation and morphology. *J. Biomed. Mater. Res.* **1999,** *44* (4), 446-455.

96. Daculsi, G.; Goyenvalle, E.; Cognet, R.; Aguado, E.; Suokas, E. O., Osteoconductive properties of poly(96L/4D-lactide)/beta-tricalcium phosphate in long term animal model. *Biomaterials* **2011,** *32* (12), 3166-3177.

97. Ahmadipour, M.; Mohammadi, H.; Pang, A. L.; Arjmand, M.; Ayode Otitoju, T.; U. Okoye, P.; Rajitha, B., A review: silicate ceramic-polymer composite scaffold for bone tissue engineering. *Int. J. Poly. Mater. Poly. Biomater.* **2020**, 1-16.

98. Xu, Y.; Luong, D.; Walker, J. M.; Dean, D.; Becker, M. L., Modification of poly(propylene fumarate)–bioglass composites with peptide conjugates to enhance bioactivity. *Biomacromolecules* **2017,** *18* (10), 3168-3177.

99. Baino, F.; Novajra, G.; Vitale-Brovarone, C., Bioceramics and scaffolds: a winning combination for tissue engineering. *Front. Bioeng. Biotechnol.* **2015,** *3* (202).

100. Bretcanu, O.; Misra, S.; Roy, I.; Renghini, C.; Fiori, F.; Boccaccini, A. R.; Salih, V., In vitro biocompatibility of 45S5 Bioglass®-derived glass–ceramic scaffolds coated with poly(3-hydroxybutyrate). *J. Tissue Eng. Regen. Med.* **2009,** *3* (2), 139-148.

101. Nail, L. N.; Zhang, D.; Reinhard, J. L.; Grunlan, M. A., Fabrication of a bioactive, PCL-based "self-fitting" shape memory polymer scaffold. *JoVE* **2015,** (104), e52981.

102. Zhang, D.; George, O. J.; Petersen, K. M.; Jimenez-Vergara, A. C.; Hahn, M. S.; Grunlan, M. A., A bioactive “self-fitting” shape memory polymer scaffold with potential to treat cranio-maxillo facial bone defects. *Acta Biomater.* **2014,** *10* (11), 4597-4605.

103. Legrand, A. P.; Marinov, G.; Pavlov, S.; Guidoin, M.-F.; Famery, R.; Bresson, B.; Zhang, Z.; Guidoin, R., Degenerative mineralization in the fibrous capsule of silicone breast implants. *J. Mater. Sci. Mater. Med.* **2005,** *16* (5), 477-485.

104. Werner, L.; Kollarits, C. R.; Mamalis, N.; Olson, R. J., Surface calcification of a 3-piece silicone intraocular lens in a patient with asteroid hyalosis: A clinicopathologic case report. *Ophthalmology* **2005,** *112* (3), 447-452.

105. Beltran, F. O.; Houk, C. J.; Grunlan, M. A., Bioactive siloxane-containing shape-memory polymer (SMP) scaffolds with tunable degradation rates. *ACS Biomater. Sci. Eng.* **2021,** *7* (4), 1631-1639.

106. Kokubo, T., Bioactive glass ceramics: properties and applications. *Biomaterials* **1991,** *12* (2), 155-163.

107. Varma, H. K.; Sreenivasan, K.; Yokogawa, Y.; Hosumi, A., In vitro calcium phosphate growth over surface modified PMMA film. *Biomaterials* **2003,** *24* (2), 297-303.

108. Tas, A. C.; Bhaduri, S. B., Rapid coating of Ti6Al4V at room temperature with a calcium phosphate solution similar to 10× simulated body fluid. *J. Mater. Res.* **2004,** *19* (9), 2742-2749.

109. Reimer, L., Scanning electron microscopy: physics of image formation and microanalysis. *Measurement Sci. Technol.* **2000,** *11* (12), 1826-1826.

110. Ciobanu, G.; Carja, G.; Ciobanu, O.; Sandu, I.; Sandu, A., SEM and EDX studies of bioactive hydroxyapatite coatings on titanium implants. *Micron* **2009,** *40* (1), 143-146.

111. Kim, S.; Ryu, H.-S.; Shin, H.; Jung, H. S.; Hong, K. S., In situ observation of hydroxyapatite nanocrystal formation from amorphous calcium phosphate in calcium-rich solutions. *Mater. Chem. Phys.* **2005,** *91* (2), 500-506.

112. Abd Mutalib, M.; Rahman, M. A.; Othman, M. H. D.; Ismail, A. F.; Jaafar, J., Scanning electron microscopy (SEM) and energy-dispersive x-ray (EDX) spectroscopy. In *Membrane Characterization*, Elsevier: 2017; pp 161-179.

113. Baji, A.; Wong, S.-C.; Liu, T.; Li, T.; Srivatsan, T. S., Morphological and X-ray diffraction studies of crystalline hydroxyapatite-reinforced polycaprolactone. *J. Biomed. Mater. Res. Part B: Appl. Biomater.* **2007,** *81B* (2), 343-350.

114. Kotian, R.; Rao, P. P.; Madhyastha, P., X-ray diffraction analysis of hydroxyapatite-coated in different plasma gas atmosphere on Ti and Ti-6Al-4V. *Eur. J. Dent.* **2017,** *11* (4), 438-446.

115. Wang, H.; Yuan, L.; An, J., Crystallographic characteristics of hydroxylapatite in hard tissues of cololabis saira. *Crystals* **2017,** *7* (4).

116. Misra, D. N., Reaction of alizarin red s with hydroxyapatite: stoichiometry and surface effect. *Coll. Surfaces* **1992,** *66* (3), 181-187.

117. Shoji, K., [Alizarin red S staining of calcium compound crystals in synovial fluid]. *Nihon Seik. Gak. Zasshi* **1993,** *67* (4), 201-10.

118. Frassica, M. T.; Jones, S. K.; Diaz-Rodriguez, P.; Hahn, M. S.; Grunlan, M. A., Incorporation of a silicon-based polymer to PEG-DA templated hydrogel scaffolds for bioactivity and osteoinductivity. *Acta Biomater.* **2019,** *99*, 100-109.

119. Komiyama, S.; Miyasaka, R.; Kikukawa, K.; Hayman, R., Can nano-hydroxyapatite permeate the oral mucosa? a histological study using three-dimensional tissue models. *PloS One* **2019,** *14* (4), e0215681-e0215681.

120. Marion, N. W.; Mao, J. J., Mesenchymal stem cells and tissue engineering. *Methods in enzymology* **2006,** *420*, 339-361.

121. Mahmood, T.; Yang, P.-C., Western blot: technique, theory, and trouble shooting. *N. Am. J. Med. Sci.* **2012,** *4* (9), 429-434.

122. Grunlan, M. A.; Zhang, D.; Schoener, C. A.; Saunders, W. B. Shape memory polymer scaffolds for tissue defects, US Patent No. 9,925,297 B2. US 9,925,297 B2, March 24, 2018.

123. Engelberg, I.; Kohn, J., Physico-mechanical properties of degradable polymers used in medical applications: a comparative study. *Biomaterials* **1991,** *12* (3), 292-304.

124. Lebourg, M.; Antón, J. S.; Ribelles, J. L. G., Porous membranes of PLLA–PCL blend for tissue engineering applications. *Eur. Polym. J.* **2008,** *44* (7), 2207-2218.

125. Middleton, J. C.; Tipton, A. J., Synthetic biodegradable polymers as orthopedic devices. *Biomaterials* **2000,** *21* (23), 2335-2346.

126. Woodruff, M. A.; Hutmacher, D. W., The return of a forgotten polymer—polycaprolactone in the 21st century. *Prog. Polym. Sci.* **2010,** *35* (10), 1217-1256.

127. Woodard, L. N.; Grunlan, M. A., Hydrolytic degradation of PCL–PLLA semi-IPNs exhibiting rapid, tunable degradation. *ACS Biomater. Sci. Eng.* **2019,** *5* (2), 498-508.

128. Woodard, L. N.; Kmetz, K. T.; Roth, A. A.; Page, V. M.; Grunlan, M. A., Porous poly(ε-caprolactone)–poly(l-lactic acid) semi-interpenetrating networks as superior, defect-specific scaffolds with potential for cranial bone defect repair. *Biomacromolecules* **2017,** *18* (12), 4075-4083.

129. Pan, H.; Zheng, Q.; Guo, X.; Wu, Y.; Wu, B., Polydopamine-assisted BMP-2-derived peptides immobilization on biomimetic copolymer scaffold for enhanced bone induction in vitro and in vivo. *Colloids Surf. B: Biointerfaces* **2016,** *142*, 1-9.

130. Ku, S. H.; Ryu, J.; Hong, S. K.; Lee, H.; Park, C. B., General functionalization route for cell adhesion on non-wetting surfaces. *Biomaterials* **2010,** *31* (9), 2535-2541.

131. Zhou, Y.-Z.; Cao, Y.; Liu, W.; Chu, C. H.; Li, Q.-L., Polydopamine-induced tooth remineralization. *ACS Appl. Mater. Inter.* **2012,** *4* (12), 6901-6910.

132. Lynge, M.; van der Westen, R.; Postma, A.; Städler, B., Polydopamine—a nature-inspired polymer coating for biomedical science. *Nanoscale* **2011,** *3* (12), 4916-4928.

133. Kao, C.-T.; Lin, C.-C.; Chen, Y.-W.; Yeh, C.-H.; Fang, H.-Y.; Shie, M.-Y., Poly(dopamine) coating of 3D printed poly(lactic acid) scaffolds for bone tissue engineering. *Mater. Sci. Eng. C.* **2015,** *56*, 165-173.

134. Wu, N.; Yu, A.; Zhang, L.; Liu, W.; Gao, J.; Zhang, C.; Zheng, Y., Biocompatible nanoplatform based on mussel adhesive chemistry: effective assembly, dual mode sensing, and cellular imaging performance. *Adv. Mater. Interfaces* **2019,** *0* (0), 1900732.

135. Hong, S.; Na, Y. S.; Choi, S.; Song, I. T.; Kim, W. Y.; Lee, H., Non-covalent self-assembly and covalent polymerization co-contribute to polydopamine formation. *Adv. Funct. Mater.* **2012,** *22* (22), 4711-4717.

136. Arabiyat, A. S.; Pfau, M. R.; Grunlan, M. A.; Hahn, M. S., Intrinsic osteoinductivity of PCL-DA/PLLA semi-IPN shape memory polymer scaffolds. *J. Biomed. Mater. Res. A* **2021**.

137. US Department of Health and Human Services FDA; Center for Devices and Radiological, "Updated 510(k) sterility review guidance K90-1; guidance for industry and FDA. **2016**.

138. Mendes, G. C. C.; Brandão, T. R. S.; Silva, C. L. M., Ethylene oxide sterilization of medical devices: a review. *Am. J. Infect. Control* **2007,** *35* (9), 574-581.

139. Augustine, R.; Saha, A.; Jayachandran, V. P.; Thomas, S.; Kalarikkal, N., Dose-dependent effects of gamma irradiation on the materials properties and cell proliferation of

electrospun polycaprolactone tissue engineering scaffolds. *Int. J. of Polym. Mater.* **2015,** *64* (10), 526-533.

140. Bosworth, L. A.; Gibb, A.; Downes, S., Gamma irradiation of electrospun poly(ε-caprolactone) fibers affects material properties but not cell response. *J. Polym. Sci. B Polym. Phys.* **2012,** *50* (12), 870-876.

141. Cottam, E.; Hukins, D. W. L.; Lee, K.; Hewitt, C.; Jenkins, M. J., Effect of sterilisation by gamma irradiation on the ability of polycaprolactone (PCL) to act as a scaffold material. *Med. Eng. Phys.* **2009,** *31* (2), 221-226.

142. Gilding, D. K.; Reed, A. M., Biodegradable polymers for use in surgery—polyglycolic/poly(actic acid) homo- and copolymers: 1. *Polymer* **1979,** *20* (12), 1459-1464.

143. Gorna, K.; Gogolewski, S., The effect of gamma radiation on molecular stability and mechanical properties of biodegradable polyurethanes for medical applications. *Polym. Degrad. Stab.* **2003,** *79* (3), 465-474.

144. Nair, P. D.; Sreenivasan, K.; Jayabalan, M., Multiple gamma radiation sterilization of polyester fibres. *Biomaterials* **1988,** *9* (4), 335-338.

145. Volland, C.; Wolff, M.; Kissel, T., The influence of terminal gamma-sterilization on captopril containing poly(d,l-lactide-co-glycolide) microspheres. *J. Control Release* **1994,** *31* (3), 293-305.

146. Zada, M. H.; Kumar, A.; Elmalak, O.; Mechrez, G.; Domb, A. J., Effect of ethylene oxide and gamma (gamma-) sterilization on the properties of a PLCL polymer material in balloon implants. *ACS Omega* **2019,** *4* (25), 21319-21326.

147. Tsuji, H.; Echizen, Y.; Nishimura, Y., Photodegradation of biodegradable polyesters: a comprehensive study on poly(l-lactide) and poly(ε-caprolactone). *Polym. Degrad. Stab.* **2006,** *91* (5), 1128-1137.

148. Horakova, J.; Mikes, P.; Saman, A.; Jencova, V.; Klapstova, A.; Svarcova, T.; Ackermann, M.; Novotny, V.; Suchy, T.; Lukas, D., The effect of ethylene oxide sterilization on electrospun vascular grafts made from biodegradable polyesters. *Mater. Sci. Eng., C.* **2018,** *92*, 132-142.

149. Peniston, S. J.; Choi, S. J., Effect of sterilization on the physicochemical properties of molded poly(L-lactic acid). *J. Biomed. Mater. Res. B Appl. Biomater.* **2007,** *80* (1), 67-77.

150. Phillip Jr, E.; Murthy, N. S.; Bolikal, D.; Narayanan, P.; Kohn, J.; Lavelle, L.; Bodnar, S.; Pricer, K., Ethylene oxide's role as a reactive agent during sterilization: effects of polymer composition and device architecture. *J. Biomed. Mater. Res. B Appl. Biomater.* **2013,** *101B* (4), 532-540.

151. Thakur, R. A.; Florek, C. A.; Kohn, J.; Michniak, B. B., Electrospun nanofibrous polymeric scaffold with targeted drug release profiles for potential application as wound dressing. *Int. J. Pharm.* **2008,** *364* (1), 87-93.

152. Andrews, K. D.; Hunt, J. A.; Black, R. A., Effects of sterilisation method on surface topography and in-vitro cell behaviour of electrostatically spun scaffolds. *Biomaterials* **2007,** *28* (6), 1014-1026.

153. Duzyer, S.; Koral Koc, S.; Hockenberger, A.; Evke, E.; Kahveci, Z.; Uguz, A., Effects of different sterilization methods on polyester surfaces. *Tekst. Ve Konfeksiyon* **2013,** *23* (4), 319-324.

154. Ghobeira, R.; Philips, C.; De Naeyer, V.; Declercq, H.; Cools, P.; De Geyter, N.; Cornelissen, R.; Morent, R., Comparative study of the surface properties and cytocompatibility of plasma-treated poly-epsilon-caprolactone nanofibers subjected to different sterilization methods. *J. Biomed. Nanotechnol.* **2017,** *13* (6), 699-716.

155. Holy, C. E.; Cheng, C.; Davies, J. E.; Shoichet, M. S., Optimizing the sterilization of PLGA scaffolds for use in tissue engineering. *Biomaterials* **2000,** *22* (1), 25-31.

156. Kim, H. L.; Lee, J. H.; Lee, M. H.; Kim, H. H.; Kim, J.; Han, I.; Park, B. J.; Kim, J. K.; Han, D. W.; Kim, S. H.; Lee, S. J.; Park, J. C., Direct-current treatment as a safe sterilization method for electrospun biodegradable polymer. *Tissue Eng. Regen. Med.* **2011,** *8* (3), 320-325.

157. Kroeze, R. J.; Helder, M. N.; Roos, W. H.; Wuite, G. J. L.; Bank, R. A.; Smit, T. H., The effect of ethylene oxide, glow discharge and electron beam on the surface characteristics of poly(l-lactide-co-caprolactone) and the corresponding cellular response of adipose stem cells. *Acta Biomater.* **2010,** *6* (6), 2060-2065.

158. Shearer, H.; Ellis, M. J.; Perera, S. P.; Chaudhuri, J. B., Effects of common sterilization methods on the structure and properties of poly(D,L lactic-co-glycolic acid) scaffolds. *Tissue Eng.* **2006,** *12* (10), 2717-2727.

159. Ghobeira, R.; Philips, C.; Declercq, H.; Cools, P.; De Geyter, N.; Cornelissen, R.; Morent, R., Effects of different sterilization methods on the physico-chemical and bioresponsive properties of plasma-treated polycaprolactone films. *Biomed. Mater.* **2017,** *12* (1), 015017.

160. Kord Forooshani, P.; Polega, E.; Thomson, K.; Bhuiyan, M. S. A.; Pinnaratip, R.; Trought, M.; Kendrick, C.; Gao, Y.; Perrine, K. A.; Pan, L.; Lee, B. P., Antibacterial

properties of mussel-inspired polydopamine coatings prepared by a simple two-step shaking-assisted method. *Front. Chem.* **2019,** *7* (631).

161. Kaihara, S.; Matsumura, S.; Mikos, A. G.; Fisher, J. P., Synthesis of poly(L-lactide) and polyglycolide by ring-opening polymerization. *Nat. Protoc.* **2007,** *2*, 2767.

162. Pfau, M. R.; McKinzey, K. G.; Roth, A. A.; Graul, L. M.; Maitland, D. J.; Grunlan, M. A., Shape memory polymer (SMP) scaffolds with improved self-fitting properties. *J. Mater. Chem. B* **2021,** *9* (18), 3826-3837.

163. Pitt, C. G.; Chasalow, F. I.; Hibionada, Y. M.; Klimas, D. M.; Schindler, A., Aliphatic polyesters. The degradation of poly(ϵ-caprolactone) in vivo. *J. Appl. Polym. Sci.* **1981,** *26* (11), 3779-3787.

164. Fukushima, K.; Tabuani, D.; Dottori, M.; Armentano, I.; Kenny, J. M.; Camino, G., Effect of temperature and nanoparticle type on hydrolytic degradation of poly(lactic acid) nanocomposites. *Polym. Degrad. Stab.* **2011,** *96* (12), 2120-2129.

165. Kokubo, T.; Takadama, H., How useful is SBF in predicting in vivo bone bioactivity? *Biomaterials* **2006,** *27* (15), 2907-2915.

166. Madbouly, S. A.; Kratz, K.; Klein, F.; Lüetzow, K.; Lendlein, A., Thermomechanical behaviour of biodegradable shape-memory polymer foams. *MRS Proceedings* **2009,** *1190*, 1190-NN04-04.

167. Hearon, K.; Singhal, P.; Horn, J.; Small, W. t.; Olsovsky, C.; Maitland, K. C.; Wilson, T. S.; Maitland, D. J., Porous shape memory polymers. *Polym. Rev.* **2013,** *53* (1), 41-75.

168. Tobushi, H.; Hara, H.; Yamada, E.; Hayashi, S., Thermomechanical properties in a thin film of shape memory polymer of polyurethane series. *Smart Mater. Struct.* **1996,** *5* (4), 483-491.

169. Barclay, T. G.; Hegab, H. M.; Clarke, S. R.; Ginic-Markovic, M., Versatile surface modification using polydopamine and related polycatecholamines: chemistry, structure, and applications. *Adv. Mater. Interfaces* **2017,** *4* (19), 1601192.

170. Fredi, G.; Simon, F.; Sychev, D.; Melnyk, I.; Janke, A.; Scheffler, C.; Zimmerer, C., Bioinspired polydopamine coating as an adhesion enhancer between paraffin microcapsules and an epoxy matrix. *ACS Omega* **2020,** *5* (31), 19639-19653.

171. Wu, C.; Fan, W.; Chang, J.; Xiao, Y., Mussel-inspired porous SiO2 scaffolds with improved mineralization and cytocompatibility for drug delivery and bone tissue engineering. *J. Mater. Chem.* **2011,** *21* (45), 18300-18307.

172. Xi, Z.-Y.; Xu, Y.-Y.; Zhu, L.-P.; Wang, Y.; Zhu, B.-K., A facile method of surface modification for hydrophobic polymer membranes based on the adhesive behavior of poly(DOPA) and poly(dopamine). *J. Membr. Sci.* **2009,** *327* (1), 244-253.

173. Pfau, M. R.; McKinzey, K. G.; Roth, A. A.; Grunlan, M. A., PCL-based shape memory polymer semi-IPNs: the role of miscibility in tuning the degradation rate. *Biomacromolecules* **2020,** *21* (6), 2493-2501.

174. F. v. Burkersroda, F.; Schedl, L.; Göpferich, A., Why degradable polymers undergo surface erosion or bulk erosion. *Biomaterials* **2002,** *23* (21), 4221-31.

175. Abdulghani, S.; Mitchell, G. R., Biomaterials for in situ tissue regeneration: a review. *Biomolecules* **2019,** *9* (11), 750.

176. Dias, J. R.; Ribeiro, N.; Baptista-Silva, S.; Costa-Pinto, A. R.; Alves, N.; Oliveira, A. L., In situ enabling approaches for tissue regeneration: Current challenges and new developments. *Front. Bioeng. Biotechnol.* **2020,** *8* (85).

177. Khader, B. A.; Towler, M. R., Materials and techniques used in cranioplasty fixation: a review. *Mater. Sci. Eng. C* **2016,** *66*, 315-322.

178. Lendlein, A.; Kelch, S., Shape-memory polymers. *Angew. Chem. Int. Ed.* **2002,** *41* (12), 2034-2057.

179. Luo, X.; Mather, P. T., Preparation and characterization of shape memory elastomeric composites. *Macromolecules* **2009,** *42* (19), 7251-7253.

180. Xie, T., Recent advances in polymer shape memory. *Polymer* **2011,** *52* (22), 4985-5000.

181. Small, I. V. W.; Singhal, P.; Wilson, T. S.; Maitland, D. J., Biomedical applications of thermally activated shape memory polymers. *J. Mater. Chem.* **2010,** *20* (17), 3356-3366.

182. Bružauskaitė, I.; Bironaitė, D.; Bagdonas, E.; Bernotienė, E., Scaffolds and cells for tissue regeneration: different scaffold pore sizes-different cell effects. *Cytotechnology* **2016,** *68* (3), 355-369.

183. Hutmacher, D. W., Scaffolds in tissue engineering bone and cartilage. *Biomaterials* **2000,** *21* (24), 2529-2543.

184. Roseti, L.; Parisi, V.; Petretta, M.; Cavallo, C.; Desando, G.; Bartolotti, I.; Grigolo, B., Scaffolds for bone tissue engineering: state of the art and new perspectives. *Mater. Sci. Eng. C* **2017,** *78*, 1246-1262.

185. Yu, X.; Tang, X.; Gohil, S. V.; Laurencin, C. T., Biomaterials for Bone Regenerative Engineering. *Adv. Healthcare Mater.* **2015,** *4* (9), 1268-1285.

186. Erndt-Marino, J. D.; Munoz-Pinto, D. J.; Samavedi, S.; Jimenez-Vergara, A. C.; Diaz-Rodriguez, P.; Woodard, L.; Zhang, D.; Grunlan, M. A.; Hahn, M. S., Evaluation of the osteoinductive capacity of polydopamine-coated poly(ε-caprolactone) diacrylate shape memory foams. *ACS Biomater. Sci. Eng.* **2015,** *1* (12), 1220-1230.

187. Hou, Q.; De Bank, P. A.; Shakesheff, K. M., Injectable scaffolds for tissue regeneration. *J. Mater. Chem.* **2004,** *14* (13), 1915-1923.

188. Moore, W. R.; Graves, S. E.; Bain, G. I., Synthetic bone graft substitutes. *ANZ J. Surg.* **2001,** *71* (6), 354-361.

189. Serbetci, K.; Korkusuz, F.; Hasirci, N., Thermal and mechanical properties of hydroxyapatite impregnated acrylic bone cements. *Polym. Testing* **2004,** *23* (2), 145-155.

190. Slaughter, B. V.; Khurshid, S. S.; Fisher, O. Z.; Khademhosseini, A.; Peppas, N. A., Hydrogels in regenerative medicine. *Adv. Mater.* **2009,** *21* (32-33), 3307-3329.

191. Van der Stok, J.; Van Lieshout, E. M. M.; El-Massoudi, Y.; Van Kralingen, G. H.; Patka, P., Bone substitutes in the Netherlands – A systematic literature review. *Acta Biomater.* **2011,** *7* (2), 739-750.

192. Hou, Y.; Schoener, C. A.; Regan, K. R.; Munoz-Pinto, D.; Hahn, M. S.; Grunlan, M. A., Photo-cross-linked PDMSstar-PEG hydrogels: synthesis, characterization, and potential application for tissue engineering scaffolds. *Biomacromolecules* **2010,** *11* (3), 648-656.

193. Munoz-Pinto, D. J.; McMahon, R. E.; Kanzelberger, M. A.; Jimenez-Vergara, A. C.; Grunlan, M. A.; Hahn, M. S., Inorganic–organic hybrid scaffolds for osteochondral regeneration. *J. Biomed. Mater. Res* **2010,** *94A* (1), 112-121.

194. Bailey, B. M.; Fei, R.; Munoz-Pinto, D.; Hahn, M. S.; Grunlan, M. A., PDMSstar–PEG hydrogels prepared via solvent-induced phase separation (SIPS) and their potential utility as tissue engineering scaffolds. *Acta Biomater.* **2012,** *8* (12), 4324-4333.

195. Munoz-Pinto, D. J.; Jimenez-Vergara, A. C.; Hou, Y.; Hayenga, H. N.; Rivas, A.; Grunlan, M.; Hahn, M. S., Osteogenic potential of poly(ethylene glycol)–poly(dimethylsiloxane) hybrid hydrogels. *Tissue Eng. Part A* **2012,** *18* (15-16), 1710-1719.

196. Zhang, D.; Petersen, K. M.; Grunlan, M. A., Inorganic–organic shape memory polymer (SMP) foams with highly tunable properties. *ACS Appl. Mater. Inter.* **2013,** *5* (1), 186-191.

197. Schoener, C. A.; Weyand, C. B.; Murthy, R.; Grunlan, M. A., Shape memory polymers with silicon-containing segments. *J. Mater. Chem.* **2010,** *20* (9), 1787-1793.

198. Madbouly SA, K. K., Klein F, Lüzow K, Lendlein A., In *A. Mater Res Soc Symp Proc*, 2009.

199. George, K. A.; Chirila, T. V.; Wentrup-Byrne, E., Effects of crosslink density on hydrolytic degradation of poly(l-lactide)-based networks. *Polym. Degrad. Stab.* **2012,** *97* (6), 964-971.

200. Malana, M. A.; Bukhari, J.-u.-D.; Zohra, R., Synthesis, swelling behavior, and network parameters of novel chemically crosslinked poly (acrylamide-co-methacrylate-co-acrylic acid) hydrogels. *Des. Monomers Polym.* **2014,** *17* (3), 266-274.

201. Ostafinska, A.; Fortelny, I.; Nevoralova, M.; Hodan, J.; Kredatusova, J.; Slouf, M., Synergistic effects in mechanical properties of PLA/PCL blends with optimized composition, processing, and morphology. *RSC Adv.* **2015,** *5* (120), 98971-98982.

202. Urquijo, J.; Guerrica-Echevarría, G.; Eguiazábal, J. I., Melt processed PLA/PCL blends: effect of processing method on phase structure, morphology, and mechanical properties. *J. Appl. Polym.* **2015,** *132* (41).

203. Wang, F.; Altschuh, P.; Ratke, L.; Zhang, H.; Selzer, M.; Nestler, B., Progress report on phase separation in polymer solutions. *Adv. Mater.* **2019,** *31* (26), 1806733.

204. Lebourg, M.; Antón, J. S.; Ribelles, J. L. G., Hybrid structure in PCL-HAp scaffold resulting from biomimetic apatite growth. *J. Mater. Sci. Mater. Med.* **2010,** *21* (1), 33-44.

205. Tripathi, G.; Basu, B., A porous hydroxyapatite scaffold for bone tissue engineering: physico-mechanical and biological evaluations. *Ceram. Int.* **2012,** *38* (1), 341-349.

206. Jang, D.-W.; Franco, R. A.; Sarkar, S. K.; Lee, B.-T., Fabrication of porous hydroxyapatite scaffolds as artificial bone preform and its biocompatibility evaluation. *ASAIO J.* **2014,** *60* (2), 216-223.

207. Dey, S.; Pal, S. In *Evaluation of collagen-hydroxyapatite scaffold for bone tissue engineering*, 13th Int. Conf. Bioinform. Biomed. Eng., **2009**; pp 1267-1270.

208. Bružauskaitė, I.; Bironaitė, D.; Bagdonas, E.; Bernotienė, E., Scaffolds and cells for tissue regeneration: different scaffold pore sizes-different cell effects. *Cytotechnology* **2016,** *68* (3), 355-69.

209. Roseti, L.; Parisi, V.; Petretta, M.; Cavallo, C.; Desando, G.; Bartolotti, I.; Grigolo, B., Scaffolds for Bone Tissue Engineering: State of the art and new perspectives. *Mater Sci Eng C Mater Biol Appl* **2017,** *78,* 1246-1262.

210. Lu, X.; Kolzow, J.; Chen, R. R.; Du, J., Effect of solution condition on hydroxyapatite formation in evaluating bioactivity of B(2)O(3) containing 45S5 bioactive glasses. *Bioact. Mater.* **2019,** *4*, 207-214.

211. Ciarelli, T. E.; Fyhrie, D. P.; Parfitt, A. M., Effects of vertebral bone fragility and bone formation rate on the mineralization levels of cancellous bone from white females. *Bone* **2003,** *32* (3), 311-315.

212. Tsuchiya, A.; Sotome, S.; Asou, Y.; Kikuchi, M.; Koyama, Y.; Ogawa, T.; Tanaka, J.; Shinomiya, K., Effects of pore size and implant volume of porous hydroxyapatite/collagen (HAp/Col) on bone formation in a rabbit bone defect model. *J. Med. Dent. Sci.* **2008,** *55* (1), 91-99.

213. Van der Stok, J.; Van Lieshout, E. M.; El-Massoudi, Y.; Van Kralingen, G. H.; Patka, P., Bone substitutes in the Netherlands - a systematic literature review. *Acta Biomater.* **2011,** *7* (2), 739-50.

214. Dankert, F.; Erlemeier, L.; Ritter, C.; von Hänisch, C., On the molecular architectures of siloxane coordination compounds: (re-)investigating the coordination of the cyclodimethylsiloxanes Dn (n = 5–8) towards alkali metal ions. *Inorg. Chem. Front.* **2020,** *7* (11), 2138-2153.

215. Dankert, F.; von Hänisch, C., Insights into the coordination ability of siloxanes employing partially silicon based crown ethers: a comparative analysis of s-block metal complexes. *Inorg.* **2019,** *58* (5), 3518-3526.

216. Ning, C. Q.; Mehta, J.; El-Ghannam, A., Effects of silica on the bioactivity of calcium phosphate composites in vitro. *J. Mater. Sci. Mater. Med.* **2005,** *16* (4), 355-360.

217. Chen, Q. Z.; Thompson, I. D.; Boccaccini, A. R. J. B., 45S5 Bioglass®-derived glass–ceramic scaffolds for bone tissue engineering. *Biomaterials* **2006,** *27* (11), 2414-2425.

218. Ródenas-Rochina, J.; Ribelles, J. L. G.; Lebourg, M., Comparative study of PCL-HAp and PCL-bioglass composite scaffolds for bone tissue engineering. *J. Mater. Sci. Mater. Med.* **2013,** *24* (5), 1293-1308.

219. Mukhopadhyay, R., When PDMS isn't the best. *Anal. Chem.* **2007**.

220. Ruben, B.; Elisa, M.; Leandro, L.; Victor, M.; Gloria, G.; Marina, S.; Mian K, S.; Pandiyan, R.; Nadhira, L., Oxygen plasma treatments of polydimethylsiloxane surfaces: effect of the atomic oxygen on capillary flow in the microchannels. *Micro & Nano Letters* **2017,** *12* (10), 754-757.

221. Blaker, J.; Maquet, V.; Boccaccini, A.; Jérôme, R.; Bismarck, A., Wetting of bioactive glass surfaces by poly(α-hydroxyacid) melts: interaction between bioglass® and biodegradable polymers. *e-Polymers* **2005,** *5*.

222. Choong, C.; Yuan, S.; Thian, E. S.; Oyane, A.; Triffitt, J., Optimization of poly(ε-caprolactone) surface properties for apatite formation and improved osteogenic stimulation. *J. Biomed. Mater. Res. A* **2012,** *100A* (2), 353-361.

223. Erndt-Marino, J. D.; Munoz-Pinto, D. J.; Samavedi, S.; Jimenez-Vergara, A. C.; Diaz-Rodriguez, P.; Woodard, L.; Zhang, D.; Grunlan, M. A.; Hahn, M. S., Evaluation of the Osteoinductive Capacity of Polydopamine-Coated Poly(ε-caprolactone) Diacrylate Shape Memory Foams. *ACS Biomaterials Science & Engineering* **2015,** *1* (12), 1220-1230.

224. Frassica, M. T.; Jones, S. K.; Suriboot, J.; Arabiyat, A. S.; Ramirez, E. M.; Culibrk, R. A.; Hahn, M. S.; Grunlan, M. A., Enhanced osteogenic potential of phosphonated-siloxane hydrogel scaffolds. *Biomacromolecules* **2020,** *21* (12), 5189-5199.

225. Erndt-Marino, J.; Trinkle, E.; Hahn, M. S., Hyperosmolar potassium (K+) treatment suppresses osteoarthritic chondrocyte catabolic and inflammatory protein production in a 3-dimensional in vitro model. *Cartilage* **2017,** *10* (2), 186-195.

226. Erndt-Marino, J. D.; Hahn, M. S., Probing the response of human osteoblasts following exposure to sympathetic neuron-like PC-12 cells in a 3D coculture model. *J. Biomed. Mater. Res. A* **2017,** *105* (4), 984-990.

227. Arabiyat, A. S.; Diaz-Rodriguez, P.; Erndt-Marino, J. D.; Totsingan, F.; Mekala, S.; Gross, R. A.; Hahn, M. S., Effect of poly(sophorolipid) functionalization on human mesenchymal stem cell osteogenesis and immunomodulation. *ACS Appl. Bio. Materials* **2019,** *2* (1), 118-126.

228. Gregory, C. A.; Grady Gunn, W.; Peister, A.; Prockop, D. J., An alizarin red-based assay of mineralization by adherent cells in culture: comparison with cetylpyridinium chloride extraction. *Anal. Biochem.* **2004,** *329* (1), 77-84.

APPENDIX A: SUPPORTING INFORMATION

Table A-1. Scaffold pore size.

***Series A* (100:0)**	**Diameter (µm)**
NC/NS	238 ± 27
NC/S	223 ± 31
C/NS	213 ± 35
C/S	235 ± 32
***Series B* (75:25)**	**Diameter (µm)**
NC/NS	222 ± 28
NC/S	213 ± 23
C/NS	199 ± 20
C/S	203 ± 26

Table A-2. Scaffold T_m and % crystallinity.

***Series A* (100:0)**	**PCL T_m (°C)**	**PCL crystallinity (%)**	**PLLA T_m (°C)**	**PLLA crystallinity (%)**
NC/NS	55.2 ± 1.1	42.3 ± 2.1	--	--
NC/S	54.9 ± 0.6 #	45.8 ± 1.9 #	--	--
C/NS	53.7 ± 1.2 #	44.5 ± 1.2 #	--	--
C/S	55.7 ± 1.2 #	42.8 ± 0.9 #	--	--
***Series B* (75:25)**	**PCL T_m (°C)**	**PCL crystallinity (%)**	**PLLA T_m (°C)**	**PLLA crystallinity (%)**
NC/NS	52.6 ± 3.1	42.1 ± 1.2	161.6 ± 5.4	34.8 ± 8.1
NC/S	53.1 ± 2.8 #	44.4 ± 0.9 #	159.7 ± 3.2 #	37.1 ± 7.4 #
C/NS	54.4 ± 0.7 #	41.2 ± 1.4 #	164.1 ± 2.2 #	33.6 ± 5.5 #
C/S	52.4 ± 3.3 #	42.3 ± 1.7 #	163.3 ± 1.3 #	35.1 ± 3.7 #

#$p > 0.05$; no significant difference from any T_m or % crystallinity values

Table A-3. Film sol content.

***Series A* (100:0)**	**Sol Content (%)**
NC/NS	11.4 ± 2.3
NC/S	10.4 ± 2.1
C/NS	11.3 ± 3.3
C/S	10.9 ± 1.9
***Series B* (75:25)**	**Sol Content (%)**
NC/NS	12.3 ± 2.3
NC/S	11.4 ± 1.1
C/NS	11.8 ± 1.4
C/S	11.7 ± 1.6

Table A-4. Scaffold compressive modulus (*E*) values.

***Series A* (100:0)**	**Modulus (MPa)**
NC/NS	11.1 ± 2.5
NC/S	13.7 ± 1.9
C/NS	13.6 ± 2.4
C/S	12.9 ± 1.9
***Series B* (75:25)**	**Modulus (MPa)**
NC/NS	20.3 ± 2.3
NC/S	20.9 ± 2.6
C/NS	20.8 ± 4.3
C/S	19.7 ± 2.5

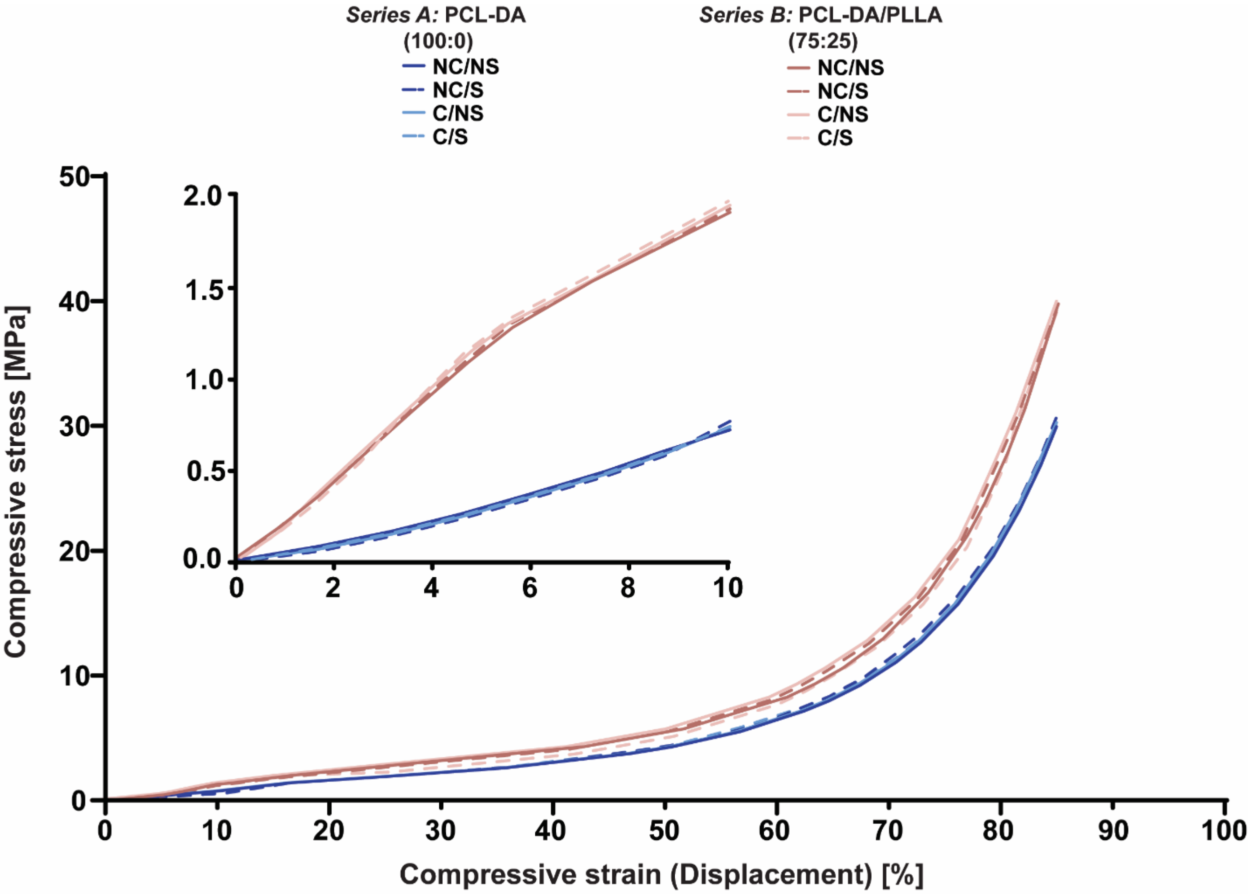

Figure A-1. Strain vs. stain curves for calculation of compressive modulus at t = 0.

Table A-5. Film contact angle (θ_{static}) values.

***Series A* (100:0)**	**Contact Angle (°)**
NC/NS	50.2 ± 0.9
NC/S	60.6 ± 3.7
C/NS	19.1 ± 3.8
C/S	29.9 ± 2.5
***Series B* (75:25)**	**Contact Angle (°)**
NC/NS	54.1 ± 6.9
NC/S	57.8 ± 1.5
C/NS	35.8 ± 2.6
C/S	38.2 ± 5.4

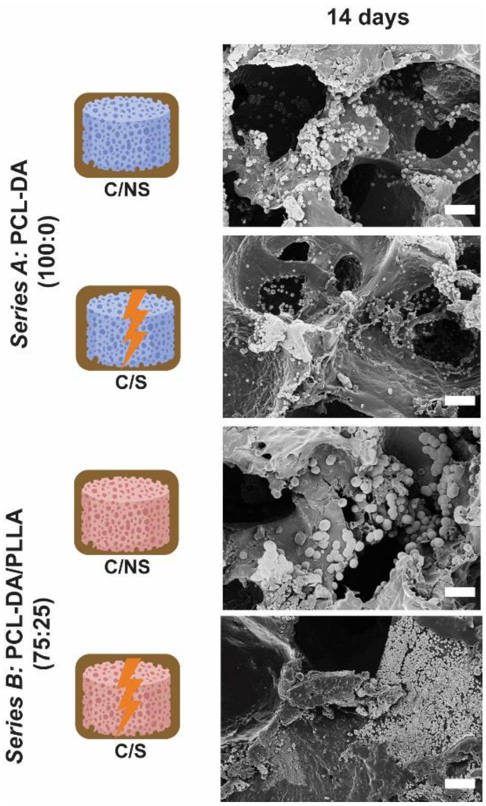

Figure A-2. SEM images of scaffold cross-sections after soaking 14 days in 1X SBF. Scale bars = 150 µm.

Table A-6. Scaffold mass remaining following accelerated conditions (0.2 M NaOH, 37 ºC, 60 rpm) at 168 hr.

***Series A* (100:0)**	**Mass Remaining (%)**
NC/NS	70.4 ± 1.1
NC/S	71.8 ± 1.9
C/NS	79.7 ± 2.2
C/S	75.2 ± 4.9
***Series B* (75:25)**	**Mass Remaining (%)**
NC/NS	5.8 ± 0.3
NC/S	3.1 ± 2.2
C/NS	19.4 ± 1.4
C/S	17.5 ± 0.6

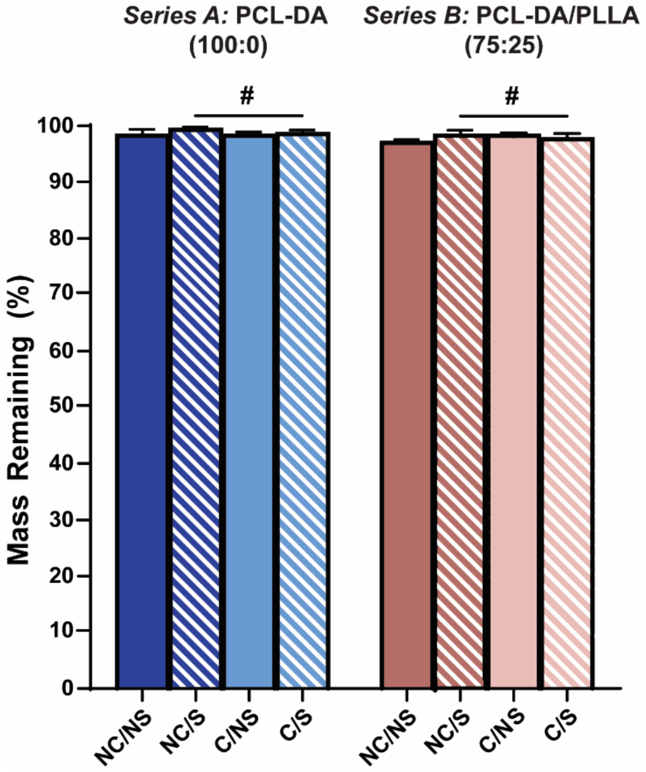

Figure A-3. Scaffold mass remaining following non-accelerated conditions (pH ~7.4 PBS, 37 ºC, 60 rpm) at 28 days. #*p* > 0.05

Table A-7. Scaffold mass remaining following non-accelerated conditions (pH ~7.4 PBS, 37 ºC, 60 rpm) at 28 days.

***Series A* (100:0)**	**Mass Remaining (%)**
NC/NS	97.1 ± 0.8
NC/S	97.5 ± 0.3
C/NS	96.8 ± 0.2
C/S	97.5 ± 0.3
***Series B* (75:25)**	**Mass Remaining (%)**
NC/NS	95.2 ± 0.4
NC/S	96.5 ± 0.6
C/NS	96.4 ± 0.4
C/S	95.9 ± 0.6

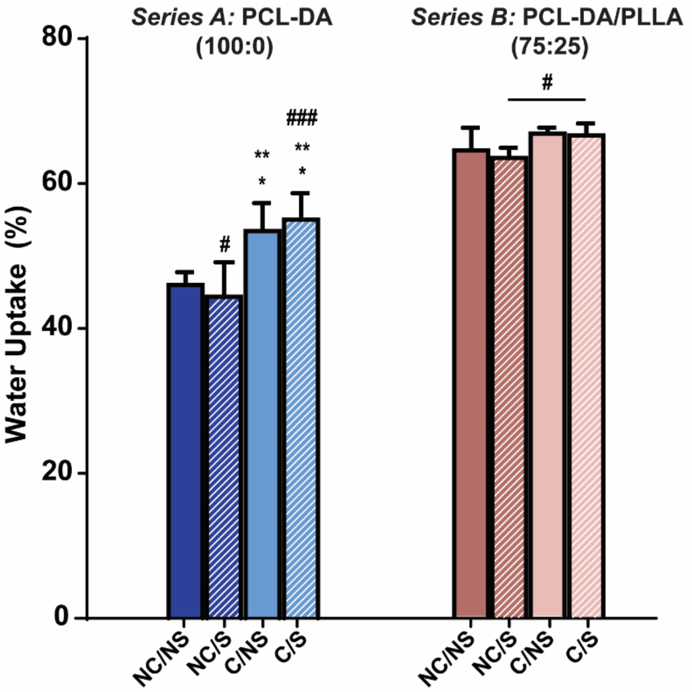

Figure A-4. Scaffold % water uptake following non-accelerated conditions at 28 days. *$p < 0.05$ vs corresponding ***NC/NS***, **$p < 0.05$ vs corresponding ***NC/S,*** ###$p > 0.05$ vs corresponding ***C/NS***, #$p > 0.05$ vs ***NC/NS*** (***Series A***), and #$p > 0.05$ (***Series B***).

Table A-8. Scaffold water uptake following non-accelerated conditions (pH ~7.4 PBS, 37 ºC, 60 rpm) at 28 days.

***Series A* (100:0)**	**PBS** ***t* = 28 days**
NC/NS	46.0 ± 1.8
NC/S	44.3 ± 4.8
C/NS	53.4 ± 3.9
C/S	55.0 ± 3.7
***Series B* (75:25)**	**PBS** ***t* = 28 days**
NC/NS	64.4 ± 3.1
NC/S	63.4 ± 1.4
C/NS	66.6 ± 0.8
C/S	66.5 ± 1.7

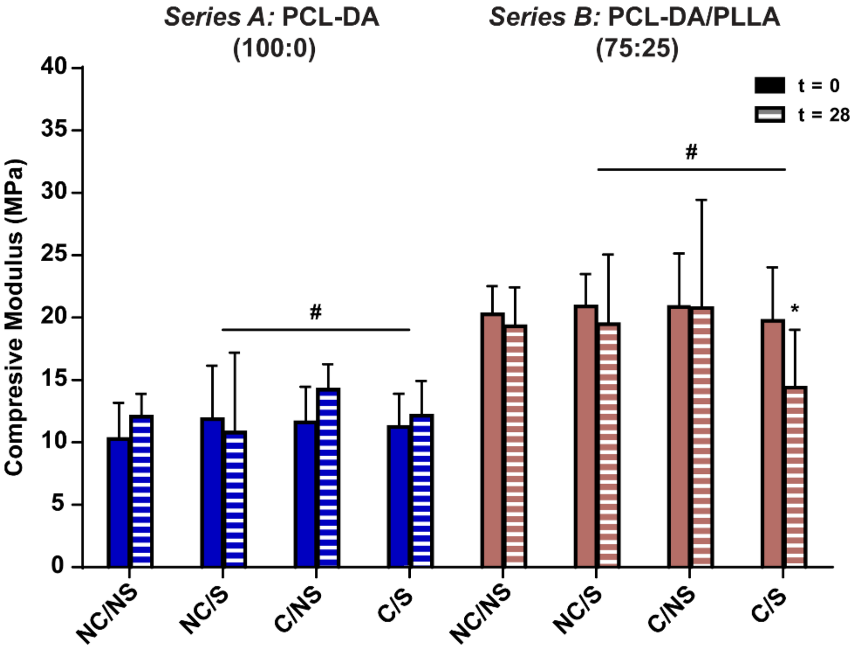

Figure A-5. Scaffold compressive modulus at $t = 0$ and following $t = 28$ days in PBS. *$p < 0.05$ vs corresponding ***NC/NS*** at same time point (i.e., $t = 0$ or $t = 28$ days), #$p > 0.05$.

Table A-9. Scaffold compressive modulus at $t = 0$ and following $t = 28$ days in PBS.

Series A **(100:0)**	**Modulus (MPa)** $t = 0$	**Modulus (MPa)** $t = 28$ **days**
NC/NS	11.1 ± 2.5	13.5 ± 0.9
NC/S	13.7 ± 1.9	11.5 ± 5.3
C/NS	13.6 ± 2.4	14.6 ± 1.7
C/S	12.9 ± 1.9	13.7 ± 1.5
Series B **(75:25)**	**Modulus (MPa)** $t = 0$	**Modulus (MPa)** $t = 28$ **days**
NC/NS	20.3 ± 2.3	19.5 ± 2.5
NC/S	20.9 ± 2.6	19.4 ± 4.8
C/NS	20.8 ± 4.3	20.6 ± 7.8
C/S	19.7 ± 2.5	14.8 ± 2.1

Table A-10. Sol Content Data

Matrix Composition	Sol Content (%)
PCL-DA **100:0**	11.1 ± 1.1
PCL-DA/*linear*-PDMS-DMA **90:10L**	12.1 ± 0.8
PCL-DA/*linear*-PDMS-DMA **75:25L**	10.6 ± 0.3
PCL-DA/*linear*-PDMS-DMA **60:40L**	10.1 ± 1.1
PCL-DA/*star*-PDMS-TMA **90:10S**	12.7 ± 0.9
PCL-DA/*star*-PDMS-TMA **75:25S**	10.7 ± 1.3
PCL-DA/*star*-PDMS-TMA **60:40S**	10.6 ± 1.4
***Triblock* 65:35**	12.2 ± 0.6

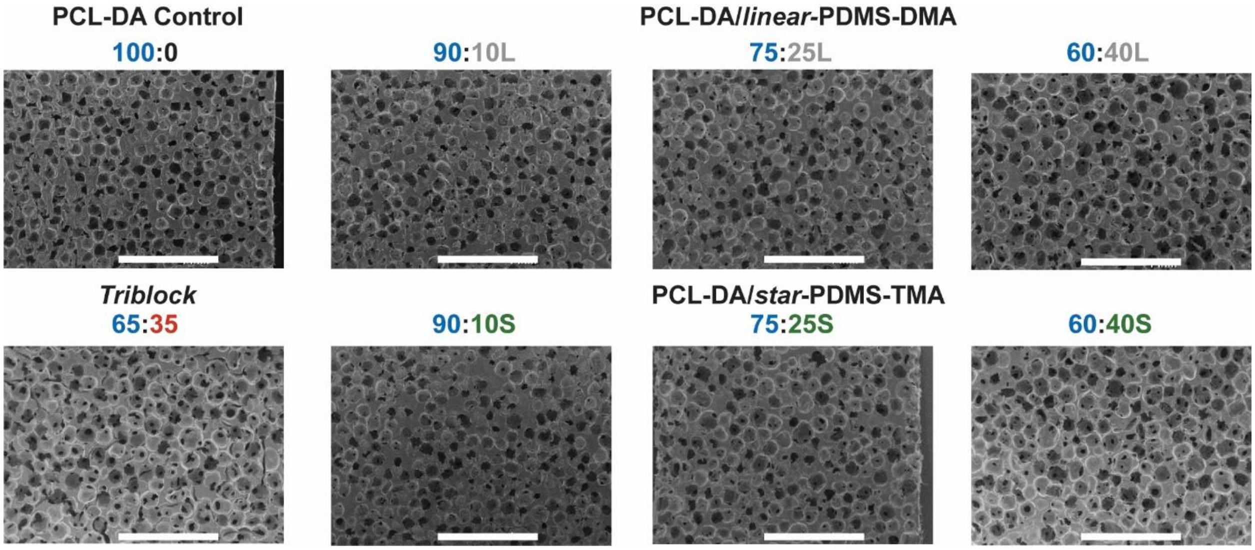

Figure A-6. SEM images of scaffold cross-sections. Scale bar = 1 mm.

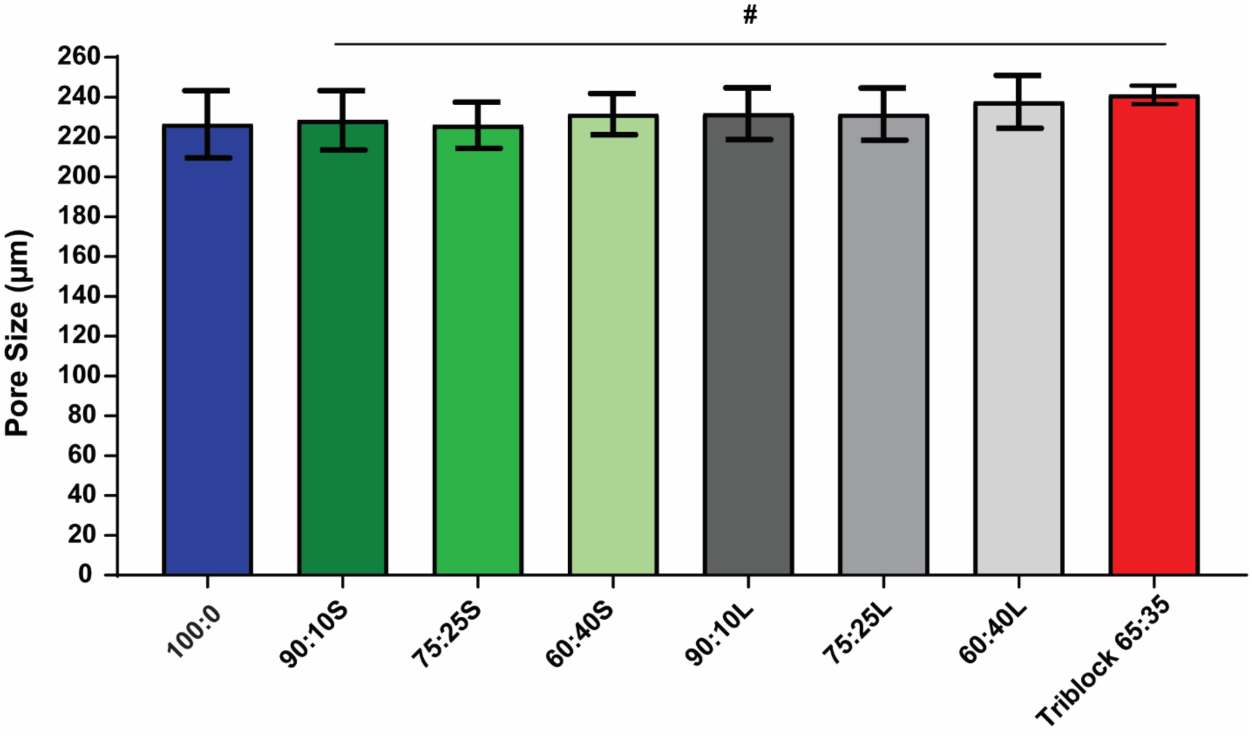

Figure A-7. Scaffold pores size. #$p > 0.05$ vs PCL-DA control (100:0).

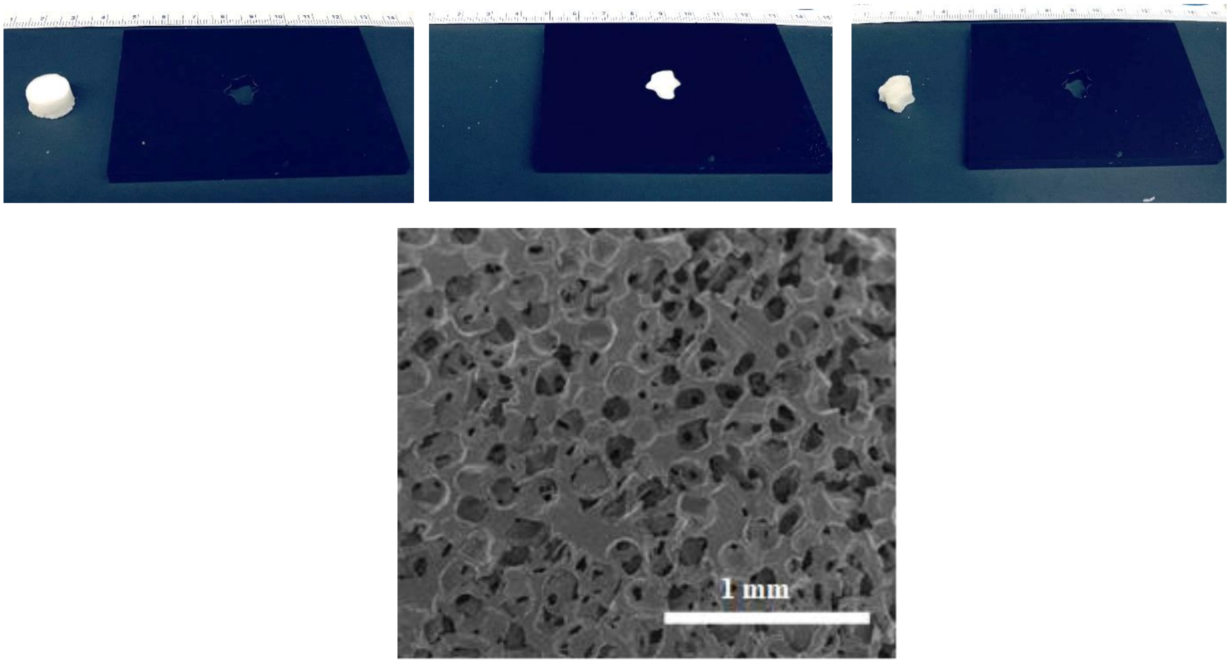

Figure A-8. (top row) Photo series of a 75:25L scaffold before fitting, after fitting, and following removal from irregular model defect. (bottom row) Following removal from model defect, SEM image 75:25L scaffold's perimeter (i.e. previously in contact with model defect).

Table A-11. Shape memory data: cycle 0 and cycle 1.

	Cycle 0		**Cycle 1**	
Matrix Composition	**R_f (%)**	**R_r (%)**	**R_f (%)**	**R_r (%)**
PCL-DA 100:0	96.7 ± 2.4	65.2 ± 2.1	100.9 ± 1.0	97.47 ± 0.4
PCL-DA/*linear*-PDMS-DMA 90:10L	93.8 ± 0.8	64.3 ± 2.2	100.8 ± 0.8	94.3 ± 2.2
PCL-DA/*linear*-PDMS-DMA 75:25L	88.3 ± 1.2	58.1 ± 4.7	101.4 ± 2.9	98.7 ± 0.8
PCL-DA/*linear*-PDMS-DMA 60:40L	89.2 ± 2.6	51.3 ± 5.6	101.1 ± 0.5	96.3 ± 0.5
PCL-DA/*star*-PDMS-TMA 90:10S	101.1 ± 4.7	62.2 ± 3.9	103.5 ± 1.1	98.9 ± 0.4
PCL-DA/*star*-PDMS-TMA 75:25S	94.2 ± 7.3	55.3 ± 6.3	102.6 ± 2.1	97.1 ± 0.9
PCL-DA/*star*-PDMS-TMA 60:40S	94.4 ± 2.8	53.4 ± 7.2	101.9 ± 2.2	91.1 ± 1.4
***Triblock* 65:35**	99.4 ± 1.1	48.8 ± 10.2	99.4 ± 1.1	92.6 ± 0.7

Table A-12. Scaffold specimen mass remaining (%) during accelerated degradation study.

Matrix Composition	24 hours	48 hours	72 hours	96 hours
PCL-DA **100:0**	92.4 ± 3.2	90.1 ± 0.7	74.9 ± 1.4	65.2 ± 1.2
PCL-DA/*linear*-PDMS-DMA **90:10L**	78.6 ± 3.4	63.5 ± 4.5	24.4 ± 2.1	13.2 ± 4.3
PCL-DA/*linear*-PDMS-DMA **75:25L**	70.1 ± 2.8	37.6 ± 2.1	12.5 ± 2.4	0
PCL-DA/*linear*-PDMS-DMA **60:40L**	66.7 ± 3.2	30.9 ± 4.2	9.63 ± 1.2	0
PCL-DA/*star*-PDMS-TMA **90:10S**	79.4 ± 2.3	51.3 ± 2.5	42.5 ± 2.8	34.5 ± 4.4
PCL-DA/*star*-PDMS-TMA **75:25S**	76.6 ± 6.9	50.1 ± 2.3	34.6 ± 4.4	24.1 ± 3.2
PCL-DA/*star*-PDMS-TMA **60:40S**	66.8 ± 2.2	41.2 ± 4.6	27.7 ± 3.2	19.4 ± 0.6
***Triblock* 65:35**	61.1 ± 1.7	26.7 ± 2.3	7.89 ± 1.2	0

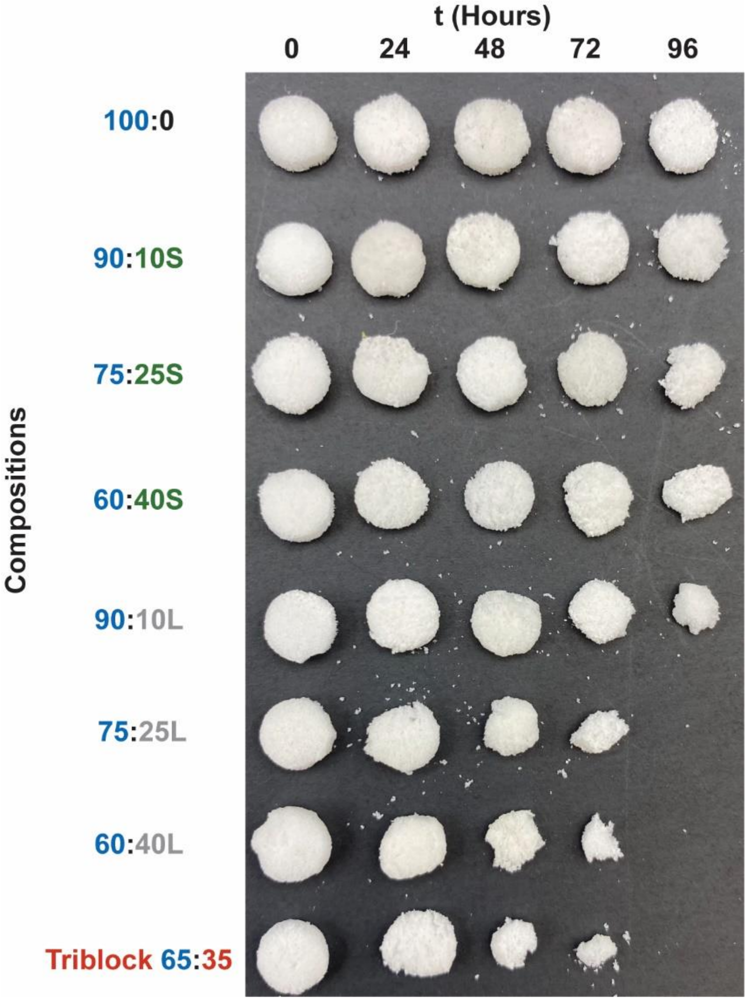

Figure A-9. Photo-series of scaffold specimens during accelerated degradation study.

Table A-13. Scaffold specimen mass remaining (%) during non-accelerated degradation study.

Matrix Composition	3 months	6 months	9 months	12 months	15 months	18 months	21 months	24 months
PCL-DA 100:0	85.9 ± 4.1	84.3 ± 0.8	83.9 ± 1.1	88.7 ± 0.6	85.6 ± 1.2	84.8 ± 0.8	81.3 ± 3.1	76.5 ± 1.2
PCL-DA/*linear*-PDMS-DMA 90:10L	82.3 ± 2.6	80.1 ± 1.4	75.2 ± 0.7	74.4 ± 1.3	69.5 ± 2.9	63.2 ± 4.2	59.8 ± 0.3	53.4 ± 1.1
PCL-DA/*linear*-PDMS-DMA 75:25L	75.8 ± 0.8	70.2 ± 0.4	67.7 ± 2.1	64.2 ± 2.2	63.9 ± 0.9	61.1 ± 0.3	53.2 ± 0.7	45.6 ± 1.2
PCL-DA/*linear*-PDMS-DMA 60:40L	71.2 ± 4.3	66.4 ± 3.1	67.1 ± 1.8	65.9 ± 0.8	65.2 ± 0.7	55.2 ± 0.8	46.8 ± 1.2	32.6 ± 2.3
PCL-DA/*star*-PDMS-TMA 90:10S	85.6 ± 1.6	78.4 ± 2.3	75.4 ± 3.2	73.2 ± 6.8	68.7 ± 0.5	66.1 ± 0.9	62.4 ± 1.6	57.8 ± 3.6
PCL-DA/*star*-PDMS-TMA 75:25S	81.5 ± 3.7	77.6 ± 4.2	74.8 ± 5.6	74.6 ± 6.5	67.8 ± 4.8	62.3 ± 3.4	58.4 ± 0.7	52.6 ± 1.0
PCL-DA/*star*-PDMS-TMA 60:40S	75.5 ± 5.1	72.7 ± 4.9	72.3 ± 5.2	72.3 ± 3.3	64.8 ± 2.7	59.7 ± 4.2	55.8 ± 0.9	41.1 ± 5.1
***Triblock* 65:35**	68.4 ± 5.2	63.4 ± 1.1	61.2 ± 1.3	59.8 ± 1.2	55.4 ± 3.1	49.5 ± 1.2	39.5 ± 1.1	16.3 ± 9.9

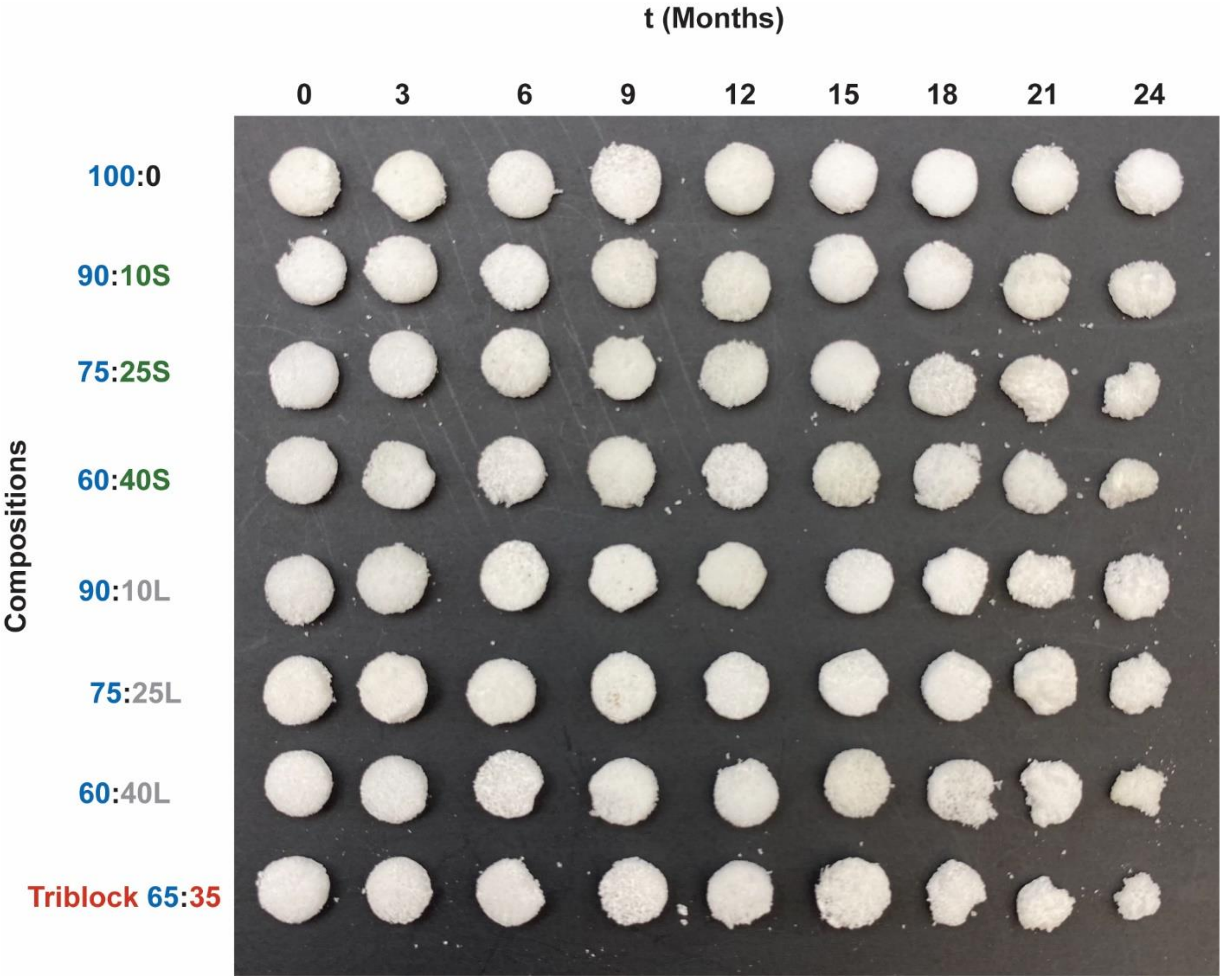

Figure A-10. Photo-series of scaffold specimens during non-accelerated degradation study.

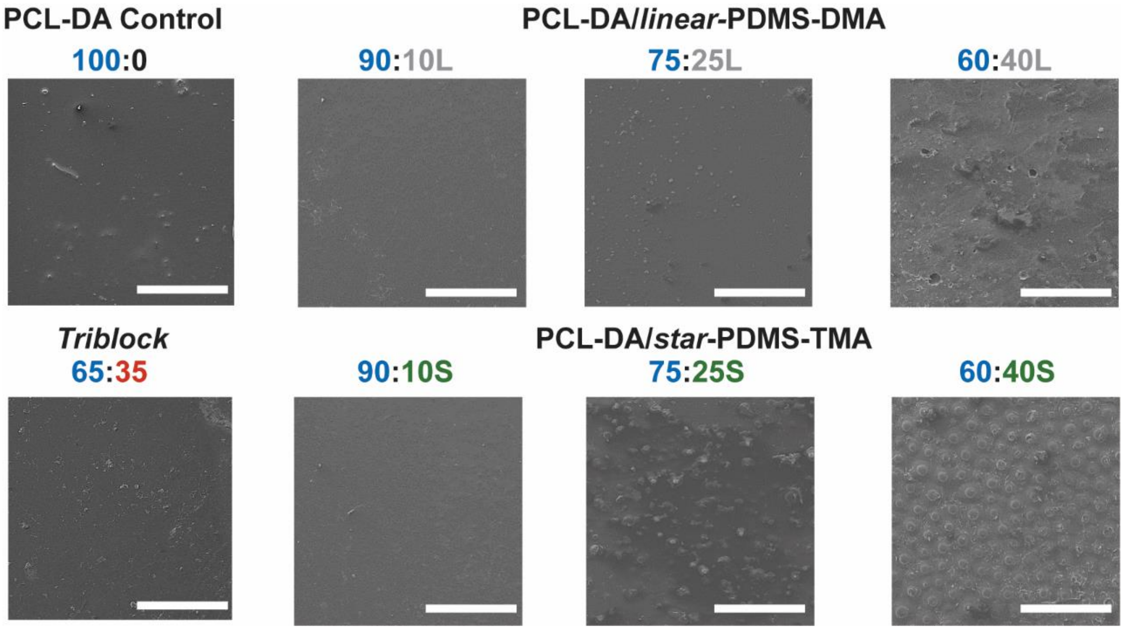

Figure A-11. SEM imaging of non-porous film surfaces. Scale bar = 500 µm.

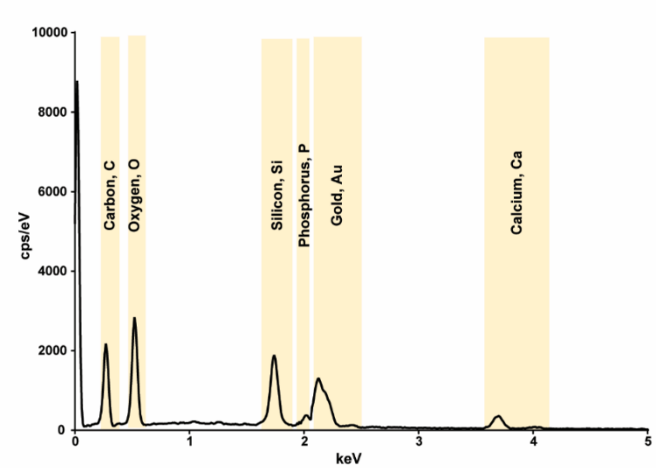

Element	Weight Fraction (%)
C	25.9
O	22.8
Si	9.1
P	3.2
Ca	6.9
Au	31.9

Element	Moles
P	0.103
Ca	0.172
Ca:P	1.67

Figure A-12. EDS spectrum shows elemental composition on material/growth's surface (C, O, and Si from polymer network; Au from the coating material; Ca and P from mineralization). Following, wt % of the elements in the spectrum are calculated and by converting the Ca and P wt % to molar amounts, a ratio of Ca:P can be determined.

Table A-14. Compressive modulus values of scaffolds (pre- and post-mineralization in SBF).

Matrix Composition	**Modulus pre-SBF (MPa)**	**Modulus post-SBF (MPa)**
PCL-DA **100:0**	8.21 ± 1.4	7.91 ± 1.3
PCL-DA/*linear*-PDMS-DMA **90:10L**	6.31 ± 1.7	10.6 ± 2.1
PCL-DA/*linear*-PDMS-DMA **75:25L**	4.91 ± 0.9	9.85 ± 1.2
PCL-DA/*linear*-PDMS-DMA **60:40L**	3.78 ± 1.2	6.99 ± 1.9
PCL-DA/*star*-PDMS-TMA **90:10S**	5.69 ± 0.8	8.98 ± 2.1
PCL-DA/*star*-PDMS-TMA **75:25S**	4.41 ± 1.1	7.62 ± 0.4
PCL-DA/*star*-PDMS-TMA **60:40S**	3.63 ± 0.7	6.77 ± 0.7
***Triblock* 65:35**	2.32 ± 0.9	4.83 ± 1.2

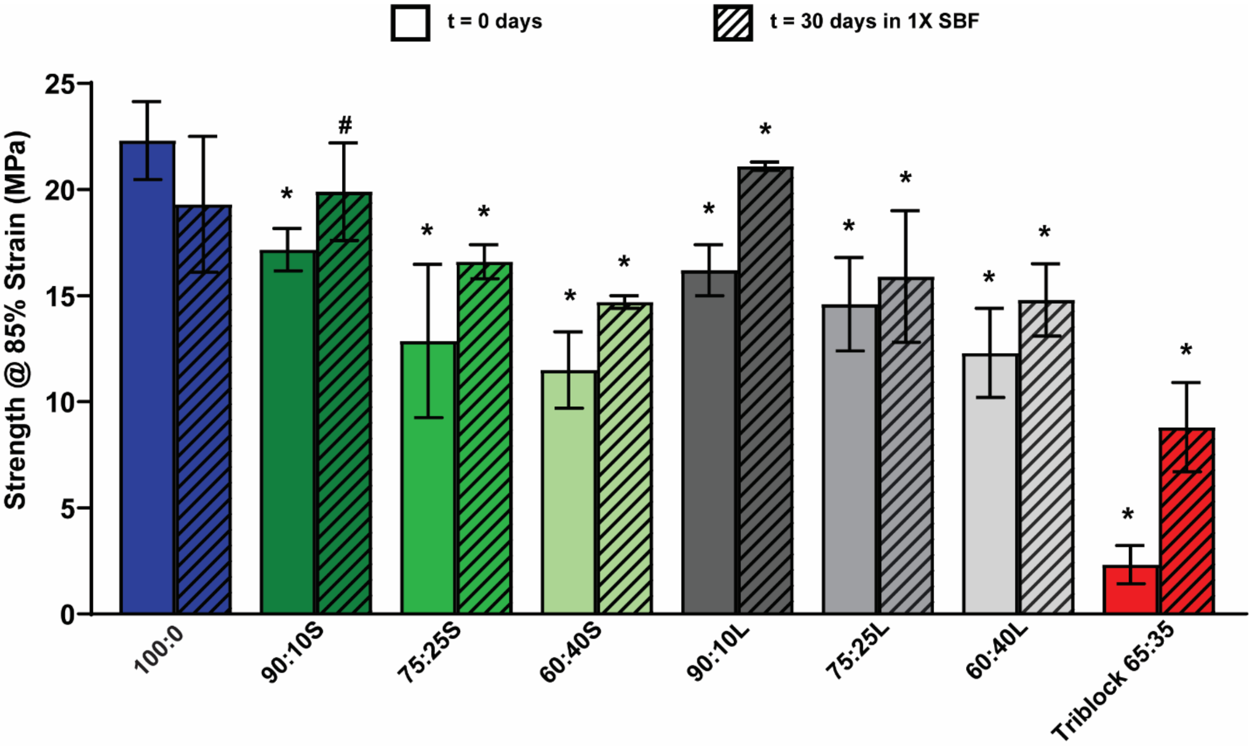

Figure A-13. Compressive strength @ 85% strain. *$p < 0.05$ vs PCL-DA control under similar conditions ($t = 0$ or 30). #$p > 0.05$ vs PCL-DA control under similar conditions ($t = 0$ or 30).

Table A-15. Compressive strength (@ 85% strain) values of scaffolds (pre- and post-mineralization in SBF).

Matrix Composition	Strength pre-SBF (MPa)	Strength post-SBF (MPa)
PCL-DA **100:0**	22.3 ± 2.9	19.3 ± 3.2
PCL-DA/*linear*-PDMS-DMA **90:10L**	16.2 ± 1.2	21.1 ± 0.2
PCL-DA/*linear*-PDMS-DMA **75:25L**	14.6 ± 2.2	15.9 ± 3.1
PCL-DA/*linear*-PDMS-DMA **60:40L**	12.3 ± 2.1	14.8 ± 1.7
PCL-DA/*star*-PDMS-TMA **90:10S**	17.1 ± 0.9	19.9 ± 2.3
PCL-DA/*star*-PDMS-TMA **75:25S**	13.2 ± 3.1	16.6 ± 0.8
PCL-DA/*star*-PDMS-TMA **60:40S**	11.5 ± 1.7	14.7 ± 0.3
***Triblock* 65:35**	2.32 ± 0.9	8.8 ± 2.1

Table A-16. Sol Content Data

Matrix Composition	**Sol Content (%) Films**	**Sol Content (%) Scaffolds**
PCL-DA 100:0	10.4 ± 0.9	3.2 ± 0.5
PCL-DA/*linear*-PDMS-DMA 90:10L	10.7 ± 1.1	3.7 ± 0.2
PCL-DA/*linear*-PDMS-DMA 75:25L	11.1 ± 0.7	2.1 ± 0.8
PCL-DA/*linear*-PDMS-DMA 60:40L	9.9 ± 0.7	2.8 ± 0.6
PCL-DA/PMHS-DMA 90:10	9.8 ± 1.2	3.1 ± 0.9
PCL-DA/PMHS-DMA 75:25	11.3 ± 0.4	3.1 ± 0.4
PCL-DA/PMHS-DMA 60:40	9.4 ± 1.5	2.4 ± 1.1

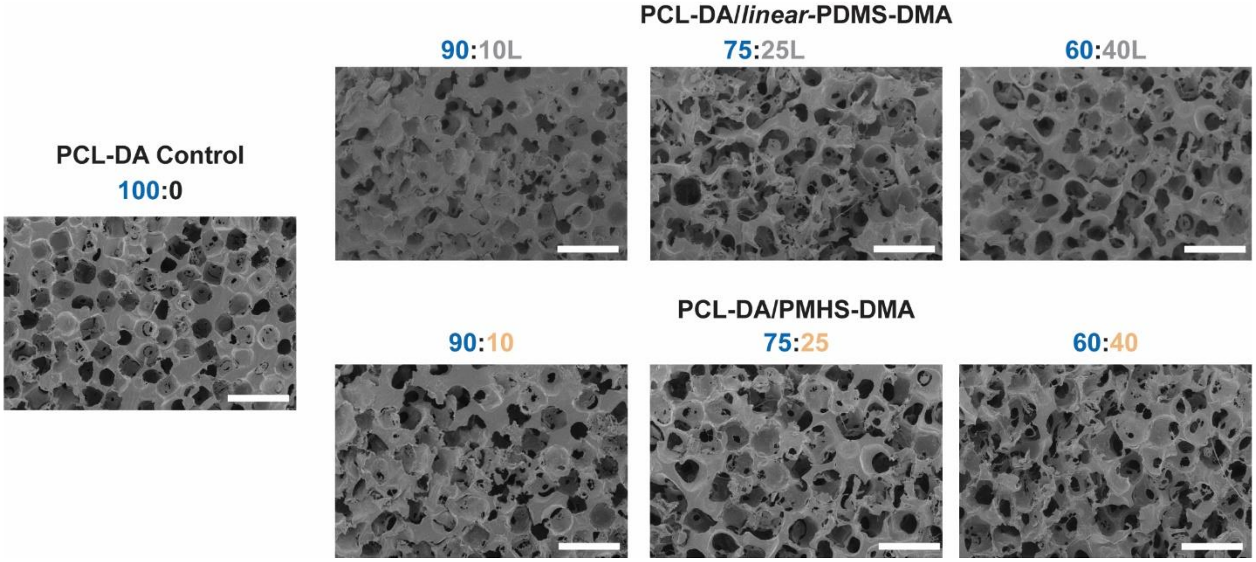

Figure A-14. SEM images of scaffold cross-sections. Scale bar = 500 µm.

Table A-17. Pore Size Data

Matrix Composition	Pore Size (µm)
PCL-DA **100:0**	224.5 ± 14.6
PCL-DA/*linear*-PDMS-DMA **90:10L**	220.1 ± 15.4 #
PCL-DA/*linear*-PDMS-DMA **75:25L**	216.7 ± 22.1 #
PCL-DA/*linear*-PDMS-DMA **60:40L**	228.8 ± 12.7 #
PCL-DA/PMHS-DMA **90:10**	227.9 ± 18.8 #
PCL-DA/PMHS-DMA **75:25**	214.1 ± 20.1 #
PCL-DA/PMHS-DMA **60:40**	222.1 ± 12.1 #

#*p* > 0.05 vs PCL-DA Control

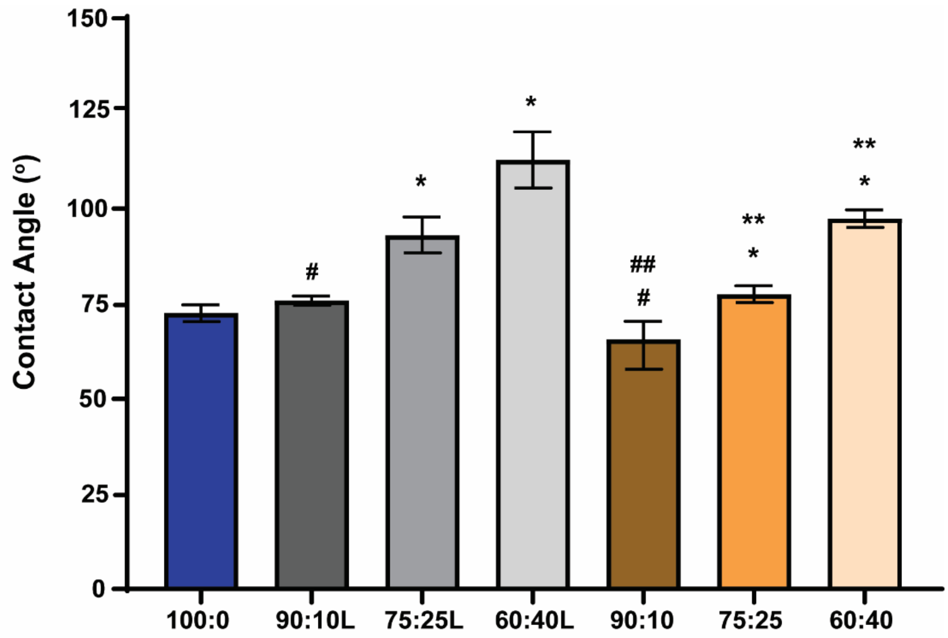

Figure A-15. θ_{static} at 2 mins of SMP films. *$p < 0.05$ vs PCL-DA control (100:0), **$p < 0.05$ vs corresponding PCL-DA/*linear*-PDMS-DMA (i.e. 90:10 vs 90:10L), #$p > 0.05$ vs vs PCL-DA control (100:0), ##$p > 0.05$ vs corresponding PCL-DA/*linear*-PDMS-DMA

Table A-18. Porosity Data

Matrix Composition	Porosity (%)
PCL-DA 100:0	64.5 ± 7.4
PCL-DA/*linear*-PDMS-DMA 90:10L	62.2 ± 5.1 #
PCL-DA/*linear*-PDMS-DMA 75:25L	65.1 ± 9.2 #
PCL-DA/*linear*-PDMS-DMA 60:40L	60.8 ± 5.3 #
PCL-DA/PMHS-DMA 90:10	59.9 ± 3.8 #
PCL-DA/PMHS-DMA 75:25	63.3 ± 2.1 #
PCL-DA/PMHS-DMA 60:40	62.3 ± 4.3 #

#$p > 0.05$ vs PCL-DA Control

Table A-19. Shape memory data: cycle 0 and cycle 1.

	Cycle 0		**Cycle 1**	
Matrix Composition	R_f (%)	R_r (%)	R_f (%)	R_r (%)
PCL-DA 100:0	94.1 ± 1.9	58.2 ± 7.2	101.1 ± 1.2	99.3 ± 1.1
PCL-DA/*linear*-PDMS-DMA 90:10L	92.1 ± 2.2	60.2 ± 5.6	99.7 ± 1.2	94.3 ± 2.2
PCL-DA/*linear*-PDMS-DMA 75:25L	85.5 ± 2.1	57.9 ± 6.8	100.1 ± 0.2	98.4 ± 3.4
PCL-DA/*linear*-PDMS-DMA 60:40L	88.1 ± 2.2	54.8 ± 6.9	99.2 ± 1.2	95.7 ± 1.2
PCL-DA/PMHS-DMA 90:10	94.4 ± 3.2	60.4 ± 7.2	99.7 ± 0.8	96.1 ± 1.1
PCL-DA/PMHS-DMA 75:25	91.1 ± 4.4	55.7 ± 8.9	97.4 ± 1.2	96.8 ± 0.5
PCL-DA/PMHS-DMA 60:40	95.8 ± 6.8	50.7 ± 2.1	98.2 ± 1.5	95.3 ± 1.3

Table A-20. Scaffold specimen mass remaining (%) during accelerated degradation study.

Matrix Composition	24 hours	48 hours	72 hours	96 hours
PCL-DA **100:0**	94.4 ± 0.1	91.4 ± 1.4	89.3 ± 1.3	88.1 ± 3.8
PCL-DA/*linear*-PDMS-DMA **90:10L**	91.4 ± 0.7	88.9 ± 1.3	86.3 ± 0.5	79.7 ± 2.1
PCL-DA/*linear*-PDMS-DMA **75:25L**	85.4 ± 2.4	83.3 ± 2.2	73.6 ± 3.3	68.3 ± 4.2
PCL-DA/*linear*-PDMS-DMA **60:40L**	81.3 ± 3.1	75.1 ± 4.0	70.2 ± 3.2	66.1 ± 3.5
PCL-DA/PMHS-DMA **90:10**	85.6 ± 2.9	79.4 ± 3.9	73.3 ± 5.3	47.9 ± 1.4
PCL-DA/PMHS-DMA **75:25**	73.2 ± 1.3	66.1 ± 3.9	54.1 ± 3.6	38.9 ± 0.1
PCL-DA/PMHS-DMA **60:40**	64.8 ± 2.3	59.4 ± 2.2	48.7 ± 5.9	9.8 ± 0.9

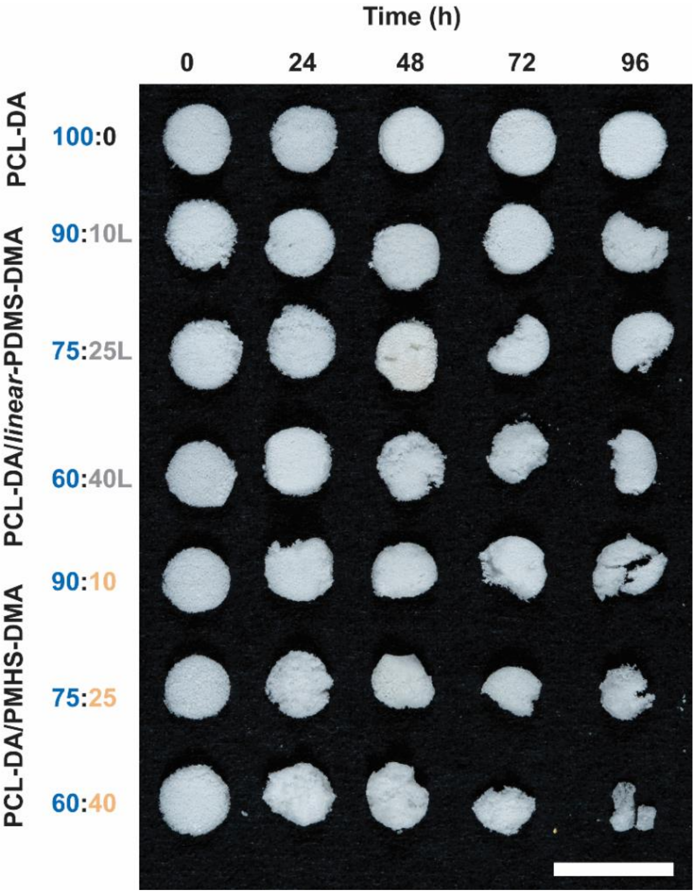

Figure A-16. Photo-series of scaffold specimens during accelerated degradation study. Scale bar = 1 cm.

Table A-21. Scaffold specimen mass remaining (%) during non-accelerated degradation study.

Matrix Composition	2 weeks	4 weeks	6 weeks	8 weeks	10 weeks	12 weeks
PCL-DA **100:0**	98.0 ± 0.4	95.8 ± 0.7	94.6 ± 0.5	94.3 ± 0.6	87.9 ± 1.8	85.1 ± 2.9
PCL-DA/*linear*-PDMS-DMA **75:25L**	93.9 ± 0.2	92.8 ± 0.3	90.7 ± 0.3	85.2 ± 0.5	79.9 ± 1.4	75.1 ± 1.5
PCL-DA/PMHS-DMA **90:10**	96.5 ± 0.5	95.4 ± 0.4	91.4 ± 0.7	89.4 ± 0.5	76.3 ± 0.9	71.8 ± 1.2
PCL-DA/PMHS-DMA **75:25**	92.3 ± 0.3	91.5 ± 0.7	87.7 ± 1.8	81.3 ± 1.0	68.9 ± 1.8	66.0 ± 0.8
PCL-DA/PMHS-DMA **60:40**	88.5 ± 1.1	87.5 ± 0.6	82.3 ± 1.6	74.1 ± 0.8	64.2 ± 2.1	60.7 ± 1.6

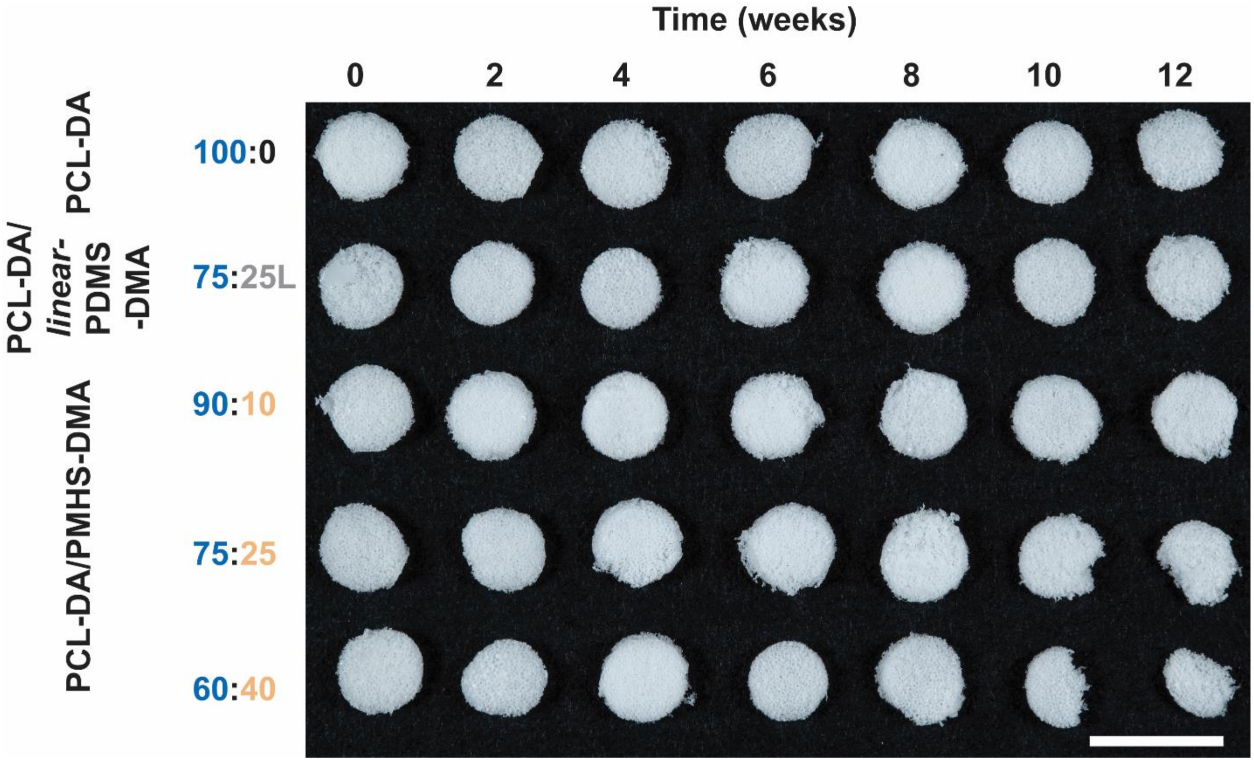

Figure A-17. Photo-series of scaffold specimens during non-accelerated degradation study. Scale bar = 1 cm.

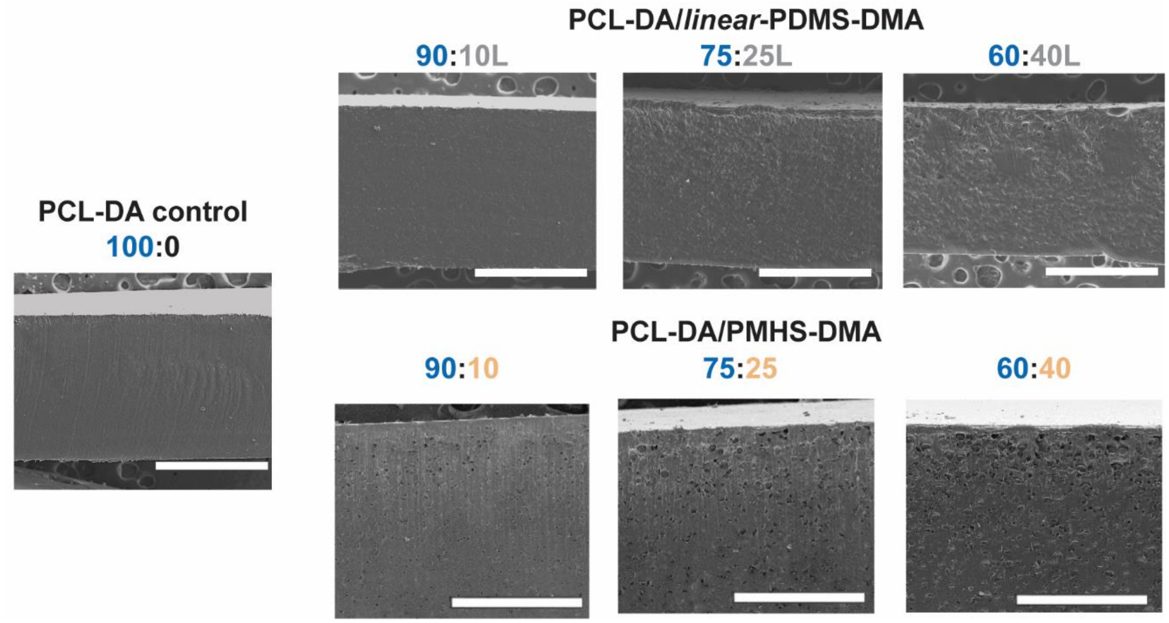

Figure A-18. SEM images of scaffold cross-sections. Scale bar = 500 µm.

Table A-22. Compressive modulus values of scaffolds (pre- and post-mineralization in SBF).

Matrix Composition	Modulus pre-SBF (MPa)	Modulus post-SBF (MPa)
PCL-DA 100:0	8.1 ± 1.1	7.7 ± 1.2
PCL-DA/*linear*-PDMS-DMA 90:10L	6.3 ± 1.3	10.2 ± 0.9
PCL-DA/*linear*-PDMS-DMA 75:25L	4.9 ± 0.2	8.8 ± 0.3
PCL-DA/*linear*-PDMS-DMA 60:40L	3.7 ± 0.6	6.9 ± 1.2
PCL-DA/PMHS-DMA 90:10	5.2 ± 0.2	10.6 ± 1.0
PCL-DA/PMHS-DMA 75:25	3.9 ± 0.4	9.1 ± 1.1
PCL-DA/PMHS-DMA 60:40	2.8 ± 1.2	7.8 ± 0.8

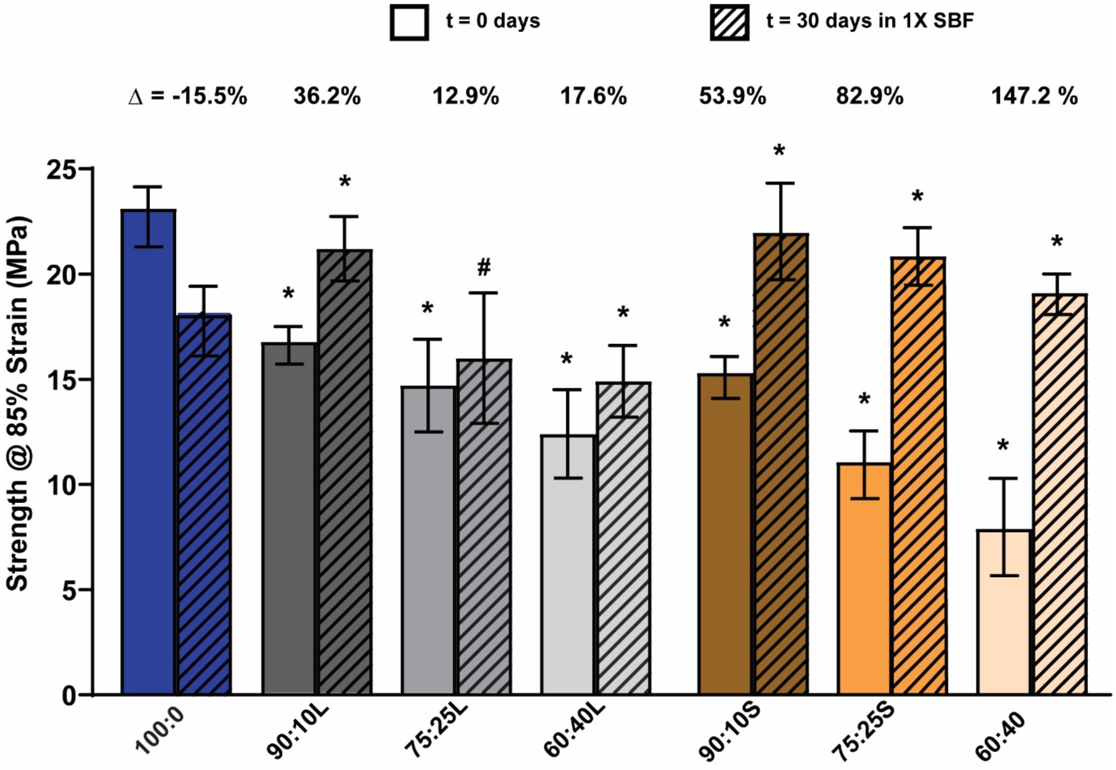

Figure A-19. Compressive strength @ 85% strain. *$p < 0.05$ vs PCL-DA control under similar conditions ($t = 0$ or 30). #$p > 0.05$ vs PCL-DA control under similar conditions ($t = 0$ or 30).

Table A-23. Compressive strength (@ 85% strain) values of scaffolds (pre- and post-mineralization in SBF).

Matrix Composition	Strength pre-SBF (MPa)	Strength post-SBF (MPa)
PCL-DA **100:0**	23.3 ± 2.9	17.6 ± 3.8
PCL-DA/*linear*-PDMS-DMA **90:10L**	16.3 ± 1.5	22.2 ± 3.5
PCL-DA/*linear*-PDMS-DMA **75:25L**	14.7 ± 2.8	16.6 ± 4.6
PCL-DA/*linear*-PDMS-DMA **60:40L**	12.5 ± 2.2	14.7 ± 2.4
PCL-DA/PMHS-DMA **90:10**	15.4 ± 1.3	23.7 ± 3.2
PCL-DA/PMHS-DMA **75:25**	11.7 ± 1.8	21.4 ± 2.3
PCL-DA/PMHS-DMA **60:40**	7.4 ± 3.1	18.3 ± 1.9

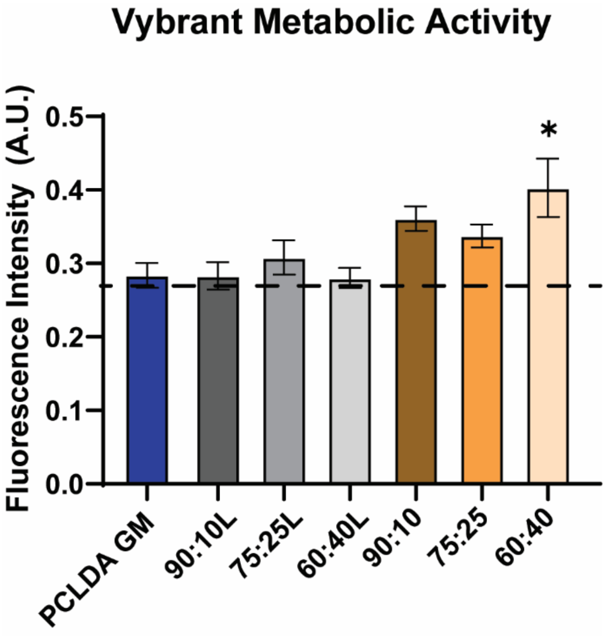

Figure A-20. Cell viability. Dashed line represents PCL-DA OM control. *$p < 0.05$ vs PCL-DA GM control.

Table A-24: Cell viability

Matrix Composition	Florescence Intensity (A.U)
PCL-DA GM	0.28 ± 0.03
PCL-DA/*linear*-PDMS-DMA 90:10L	0.28 ± 0.05
PCL-DA/*linear*-PDMS-DMA 75:25L	0.31 ± 0.06
PCL-DA/*linear*-PDMS-DMA 60:40L	0.28 ± 0.03
PCL-DA/PMHS-DMA 90:10	0.36 ± 0.04
PCL-DA/PMHS-DMA 75:25	0.34 ± 0.04
PCL-DA/PMHS-DMA 60:40	0.41 ± 0.09

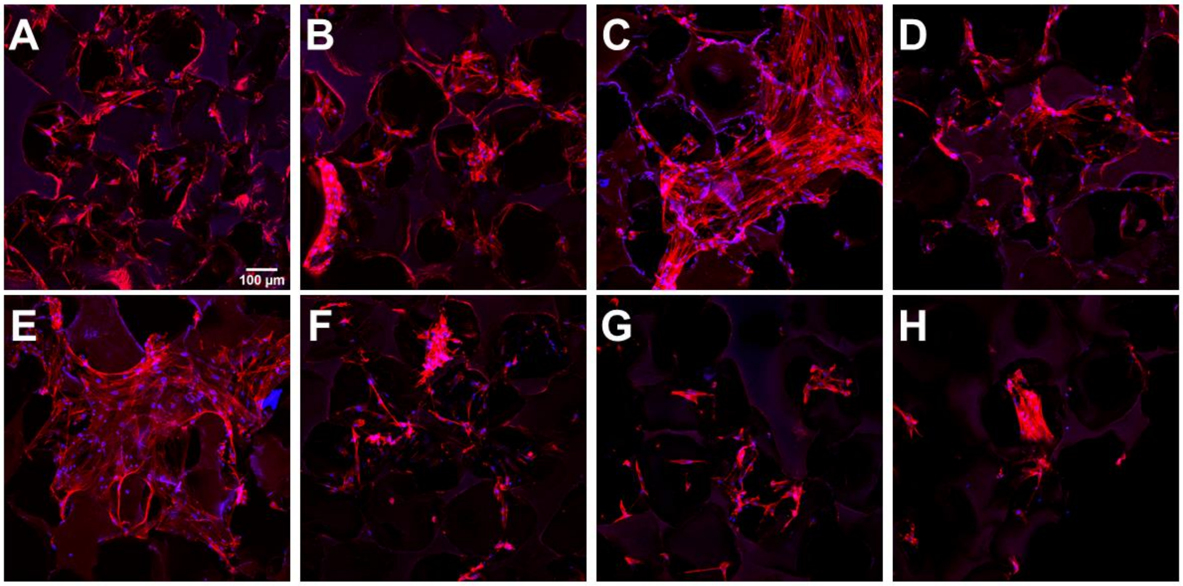

Figure A-21. Representative images of rhodamine phalloidin (red) and DAPI (blue) staining of hBMSCs in selected scaffold formulations – (A) PCL-DA GM; (B) PCL-DA OM; (C) PDMS 90:10; (D) PDMS 75:25; (E) PDMS 60:40; (F) PMHS 90:10; (G) PMHS 75:25; (H) PMHS 60:40.

Table A-25. Relative osteogenic markers of h-MCSs on scaffolds after *t* = 14 days.

Matrix Composition	BMP-4	COL1A1	OPN	SPARC	VEGF	RANKL
PCL-DA GM	1.00 ± 0.26	1.00 ± 0.04	1.00 ± 0.50	1.00 ± 0.06	1.00 ± 0.13	1.00 ± 0.17
PCL-DA/*linear*-PDMS-DMA 90:10L	1.04 ± 0.22	1.01 ± 0.24	1.08 ± 0.50	1.04 ± 0.13	1.24 ± 0.11	1.17 ± 0.31
PCL-DA/*linear*-PDMS-DMA 75:25L	1.50 ± 0.29	1.00 ± 0.40	1.50 ± 0.37	1.15 ± 0.30	1.40 ± 0.17	1.63 ± 0.71
PCL-DA/*linear*-PDMS-DMA 60:40L	1.45 ± 0.28	0.71 ± 0.04	1.99 ± 0.69	0.91 ± 0.11	1.40 ± 0.38	1.92 ± 0.50
PCL-DA/PMHS-DMA 90:10	1.36 ± 0.19	0.83 ± 0.18	1.81 ± 0.57	0.98 ± 0.11	1.33 ± 0.27	1.70 ± 0.38
PCL-DA/PMHS-DMA 75:25	1.27 ± 0.29	1.10 ± 0.31	1.66 ± 0.45	0.88 ± 0.21	1.06 ± 0.44	1.40 ± 0.67
PCL-DA/PMHS-DMA 60:40	1.24 ± 0.33	0.34 ± 0.11	2.05 ± 0.51	0.50 ± 0.15	0.70 ± 0.15	1.63 ± 0.55

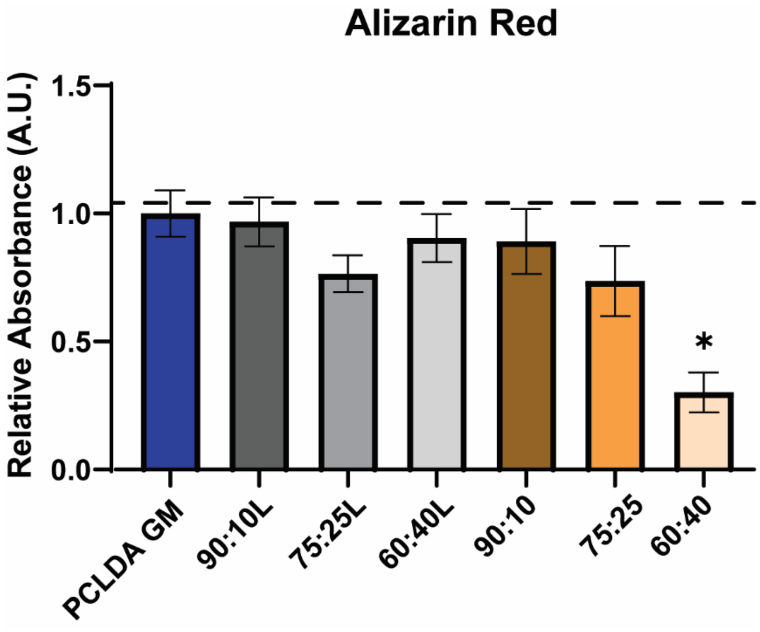

Figure A-22. Alizarin Red S staining for mineralization deposition analysis. Dashed line represents PCL-DA OM control. *$p < 0.05$ vs PCL-DA GM control.

Table A-26. Alizarin Red

Matrix Composition	Florescence Intensity (A.U)
PCL-DA GM	1.00 ± 0.18
PCL-DA/*linear*-PDMS-DMA 90:10L	0.97 ± 0.23
PCL-DA/*linear*-PDMS-DMA 75:25L	0.76 ± 0.17
PCL-DA/*linear*-PDMS-DMA 60:40L	0.90 ± 0.22
PCL-DA/PMHS-DMA 90:10	0.89 ± 0.311
PCL-DA/PMHS-DMA 75:25	0.74 ± 0.34
PCL-DA/PMHS-DMA 60:40	0.30 ± 0.19

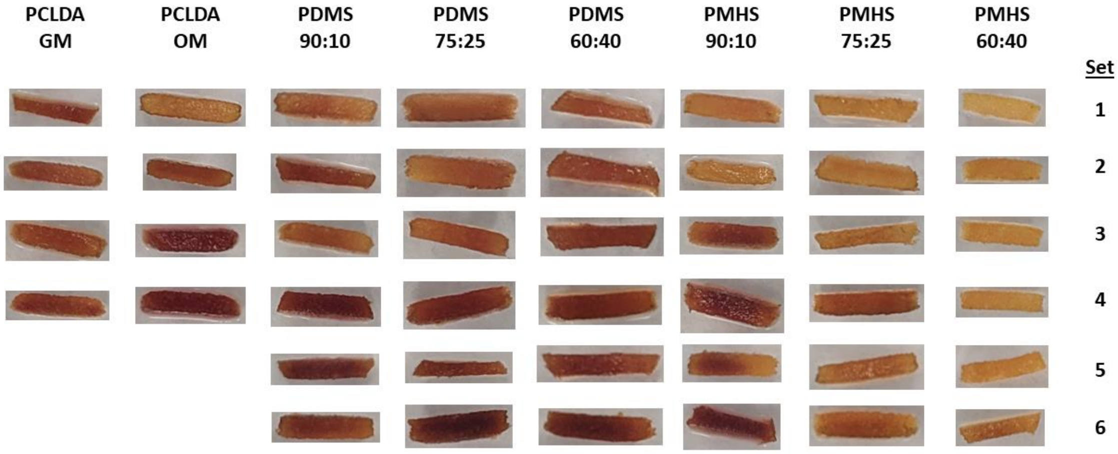

Figure A-23. Representative images of Alizarin Red S staining in selected scaffold formulations**.**

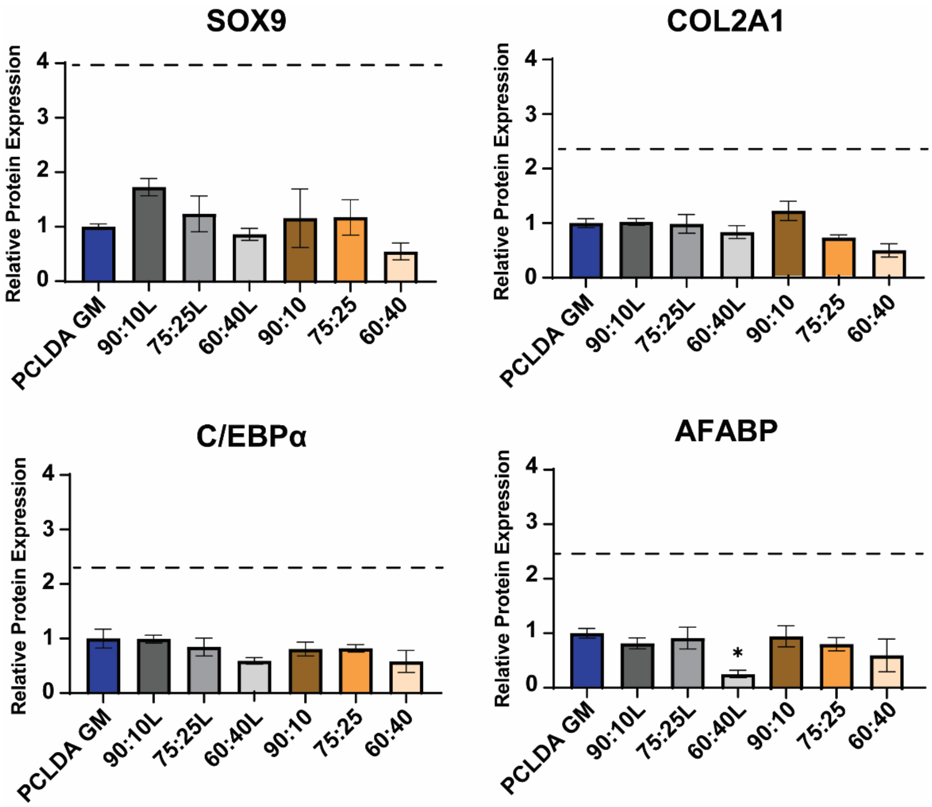

Figure A-24. Relative off-target response markers following a 14 day culture of h-MSCs normalized to PCL-DA GM. Dashed line represents PCL-DA OM control. *$p < 0.05$ vs PCL-DA GM control.

Table A-27. Relative off-target markers of h-MCSs on scaffolds after $t = 14$ days.

Matrix Composition	SOX9	COL2A1	C/EBP-α	AFABP
PCL-DA GM	1.00 ± 0.09	1.00 ± 0.14	1.00 ± 0.29	1.00 ± 0.18
PCL-DA/*linear*-PDMS-DMA 90:10L	1.73 ± 0.35	1.02 ± 0.15	0.99 ± 0.17	0.82 ± 0.22
PCL-DA/*linear*-PDMS-DMA 75:25L	1.24 ± 0.73	0.99 ± 0.42	0.84 ± 0.40	0.91 ± 0.44
PCL-DA/*linear*-PDMS-DMA 60:40L	0.86 ± 0.25	0.84 ± 0.29	0.56 ± 0.15	0.25 ± 0.15
PCL-DA/PMHS-DMA 90:10	1.17 ± 1.20	1.19 ± 0.43	0.81 ± 0.31	0.96 ± 0.43
PCL-DA/PMHS-DMA 75:25	1.19 ± 0.73	0.70 ± 0.12	0.82 ± 0.16	0.82 ± 0.27
PCL-DA/PMHS-DMA 60:40	0.56 ± 0.28	0.46 ± 0.21	0.58 ± 0.35	0.61 ± 0.42

APPENDIX B: ^{1}H NMR SPECTRA

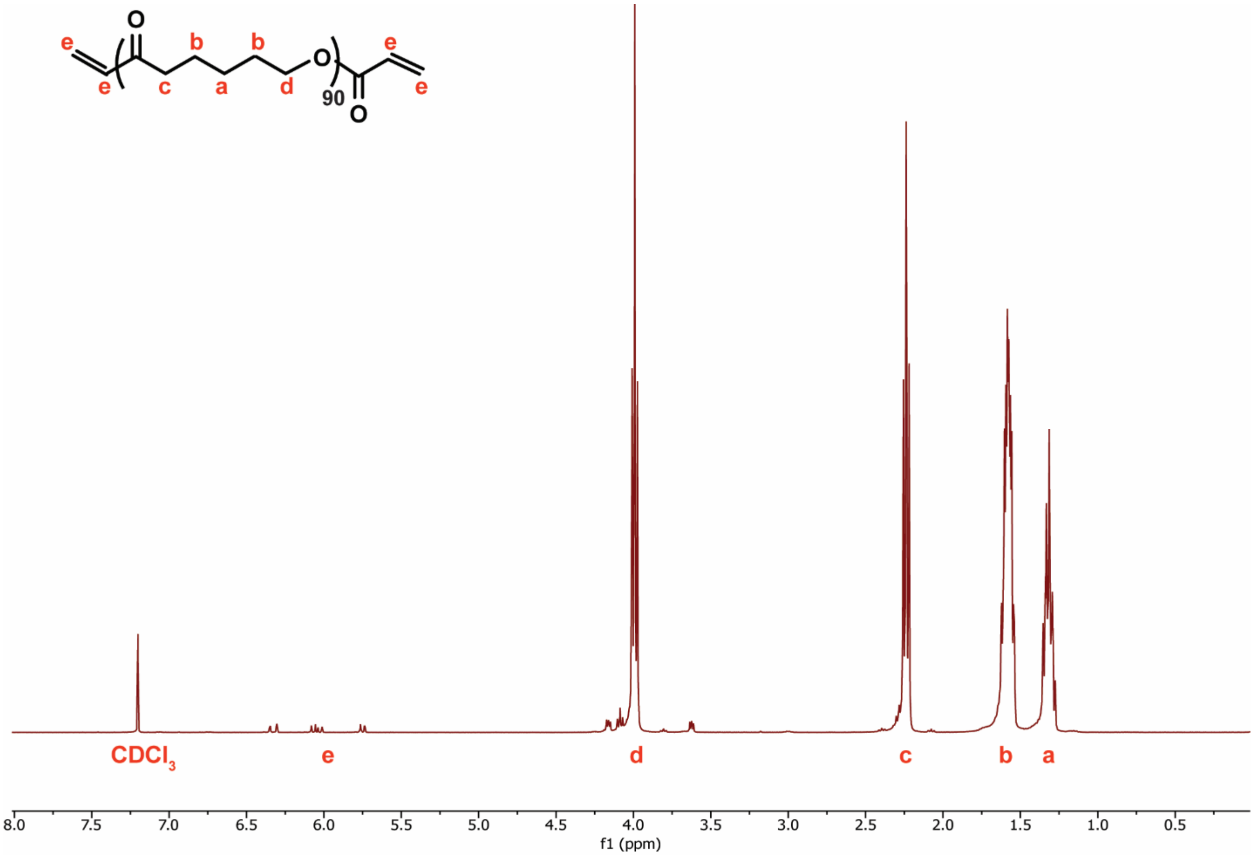

Figure B-1. NMR spectra for PCL-DA [n = 90; M_n = 10k g mol^{-1}]. ^{1}H-NMR (500 MHz; δ, ppm): 1.3 (s, 185H, -$\mathrm{CH_2}\mathit{CH_2}\mathrm{CH_2}$-), 1.6 (s, 24H, -$\mathit{CH_2}\mathrm{CH_2}\mathit{CH_2}$-), 2.3 (s, 181H, –-$\mathrm{CH_2}\mathit{CH_2}\mathrm{C{=}O}$), 4.0 (m, 182H, -$\mathrm{O}\mathit{CH_2}\mathrm{CH_2}$-), and 5.7-6.4 (m, 6H, -$\mathit{CH}{=}\mathit{CH_2}$).

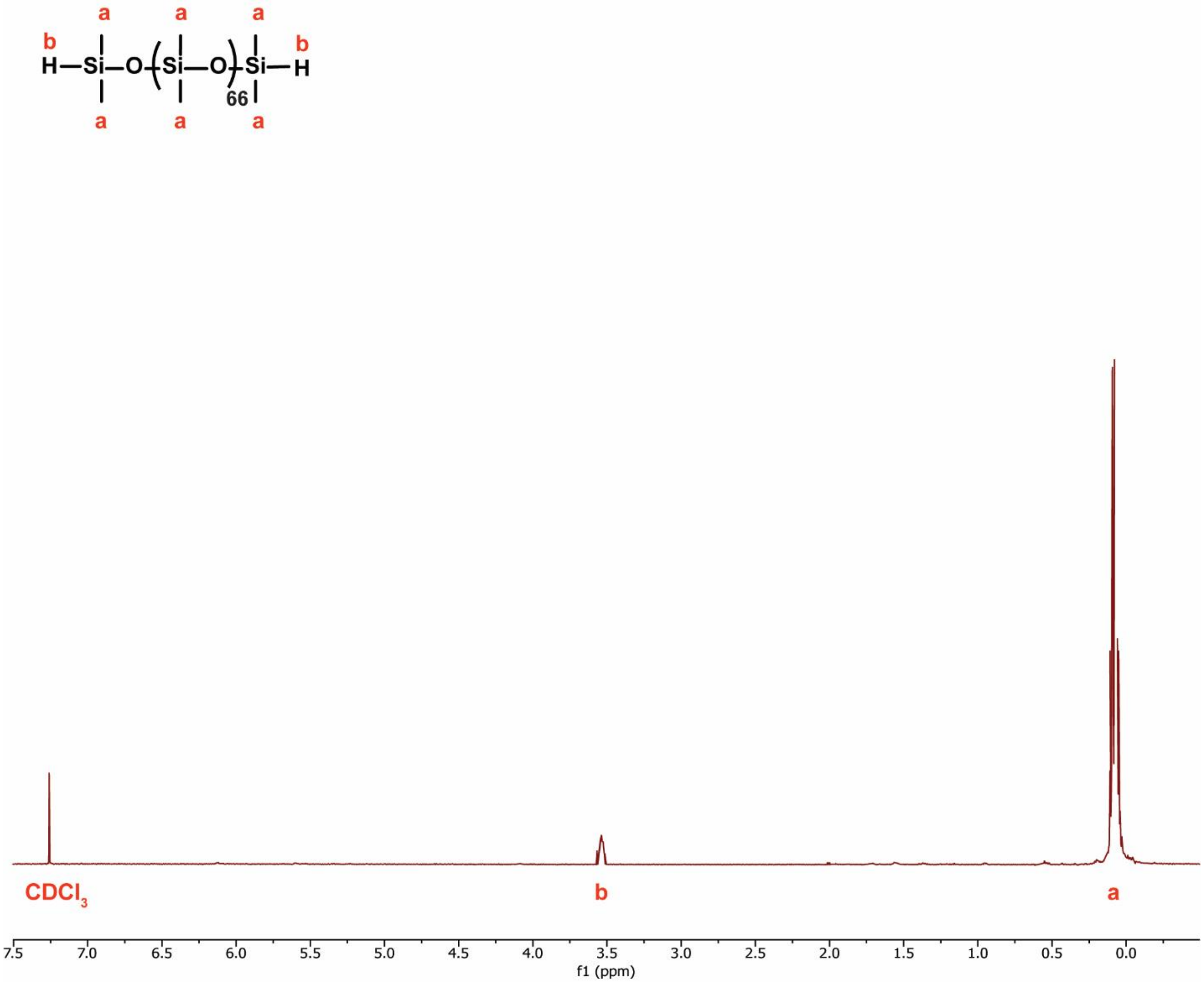

Figure B-2. NMR spectra for *linear*-PDMS-SiH [n = 66; M_n = ~4125 g mol^{-1}]. ^{1}H NMR: ^{1}H NMR (500 MHz; δ, ppm): 0.1 (bm, 411H, SiCH_3), 3.6 (m, 2H, SiH)

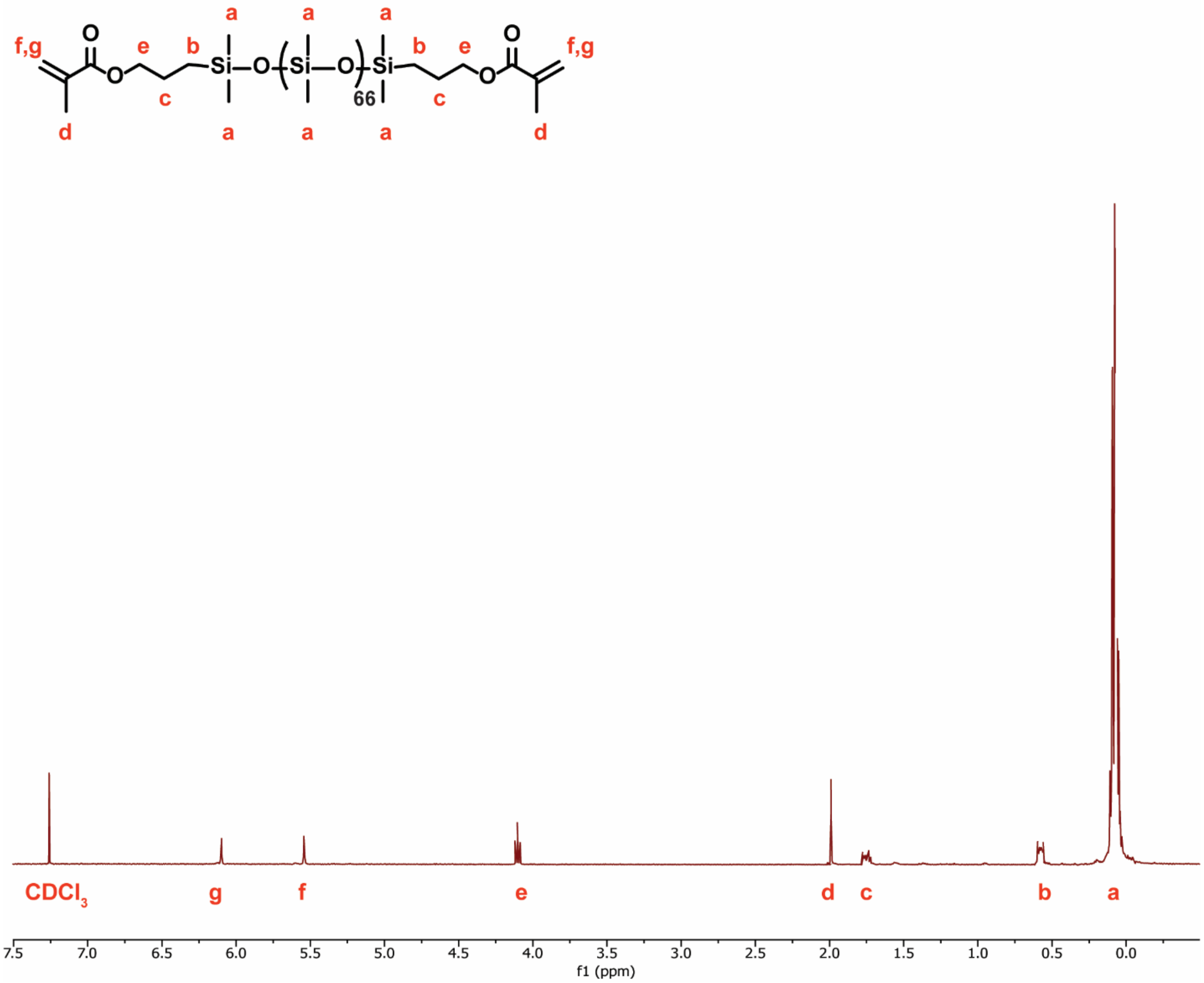

Figure B-3. NMR spectra for *linear*-PDMS-DMA [$n = 66$; M_n = ~4651 g mol^{-1}]. 1H NMR (500 MHz; δ, ppm): 0.1 (bm, 421H, SiCH_3), 0.6 (m, 4H, -Si$\mathit{CH}_2\mathrm{CH_2CH_2}$), 1.7 (m, 4H, -$\mathrm{SiCH_2}\mathit{CH}_2\mathrm{CH_2}$), 1.9 (m, 6H, -C($\mathrm{CH_2}$)($\mathit{CH}_3$), 4.2 (m, 6H, -$\mathrm{SiCH_2CH_2}\mathit{CH}_2$), 5.5 (m, 2H, -C($\mathit{CH}_2$)($\mathrm{CH_3}$)), and 6.27 (m, 2H, -C($\mathit{CH}_2$)($\mathrm{CH_3}$)).

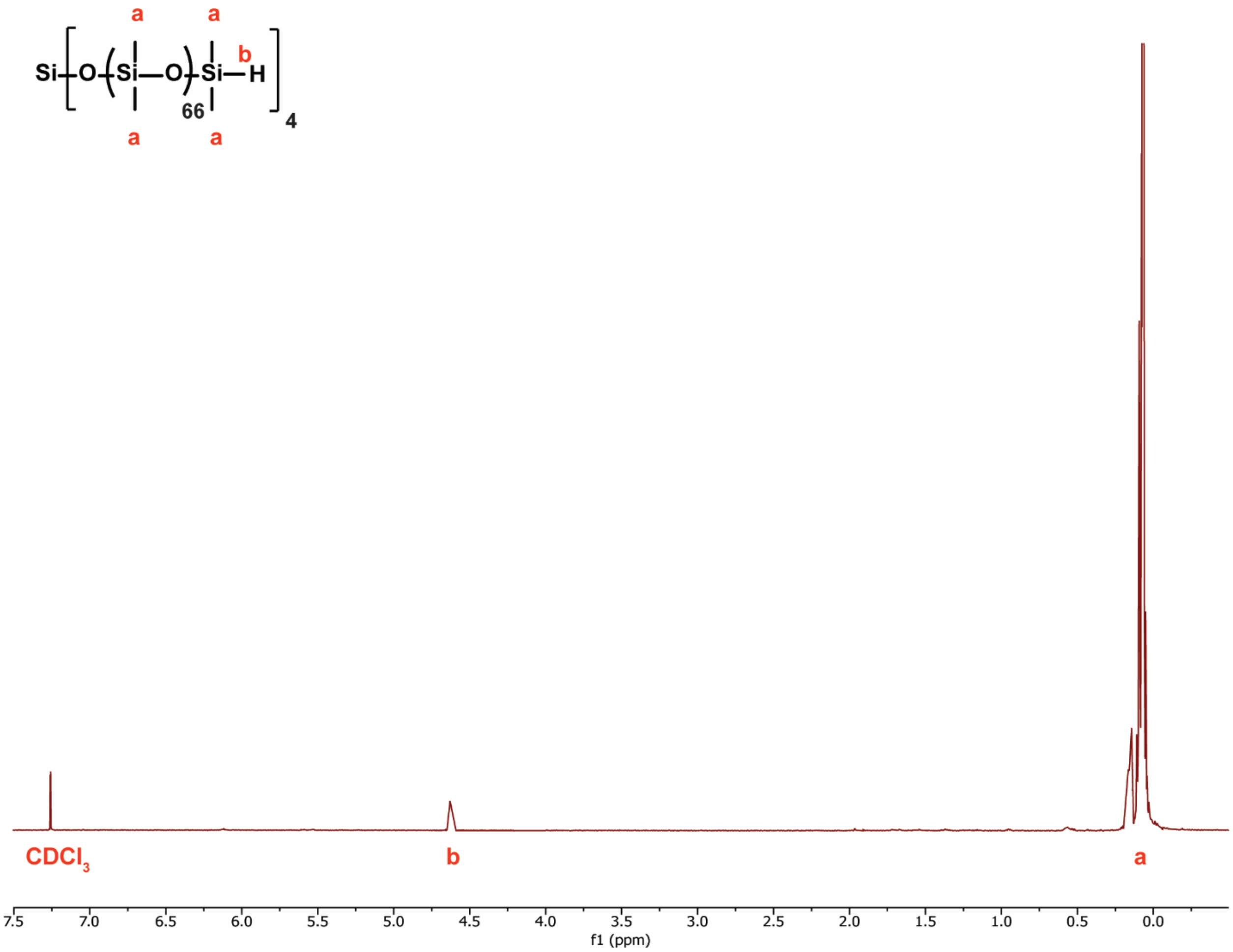

Figure B-3. NMR spectra for *star*-PDMS-SiH [n = 66; M_n = ~4334 g mol^{-1}]. ^{1}H NMR (500 MHz; δ, ppm): 0.04-0.3 (bm, 420H, SiCH_3), 4.7 (m, 4H, SiH)

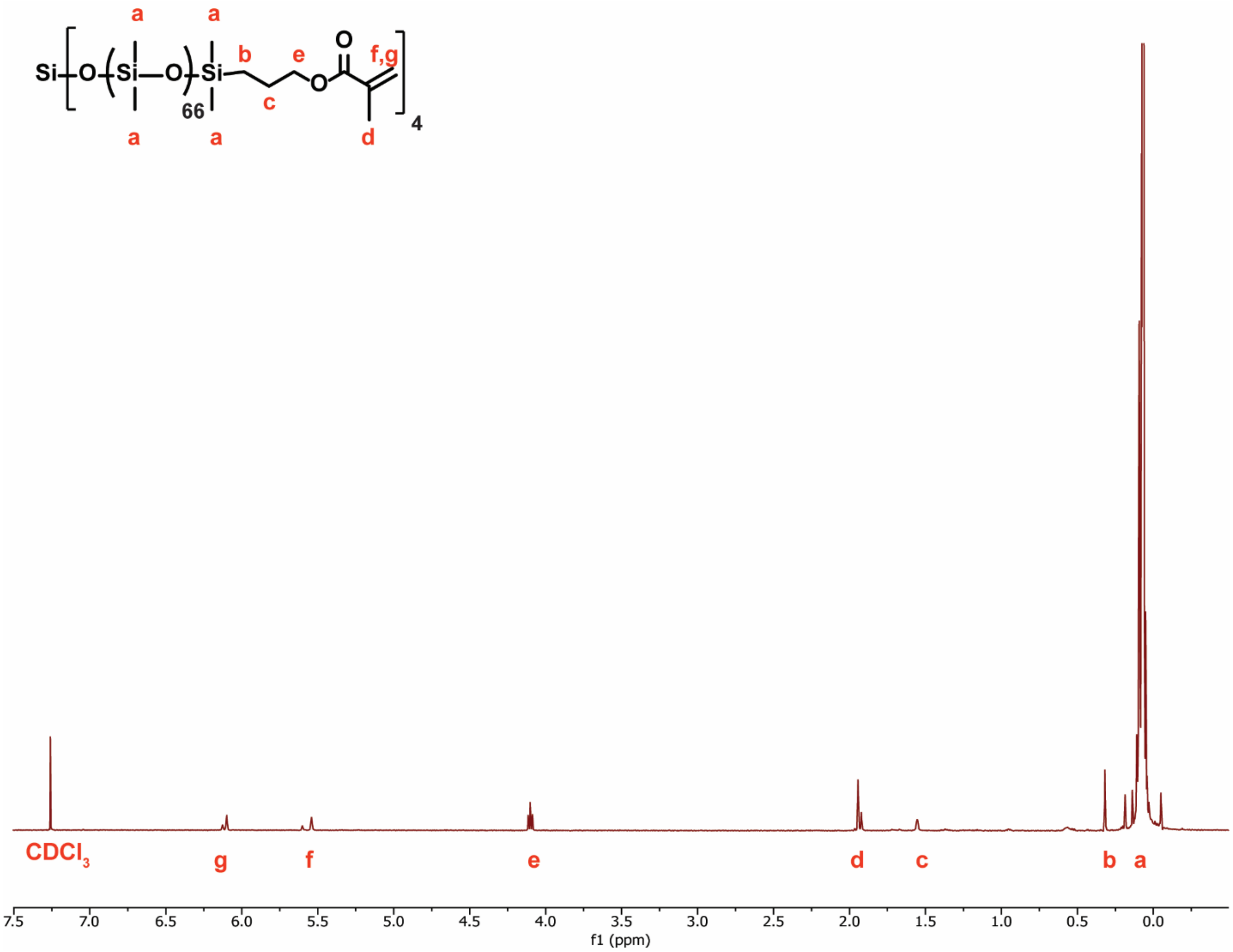

Figure B-4. NMR spectra for *star*-PDMS-TMA [n = 66; M_n = ~4827 g mol^{-1}]. ^{1}H NMR (500 MHz; δ, ppm): 0.02-0.17 (bm, 442H, Si$\mathit{CH_3}$), 0.3 (m, 8H, -Si$\mathit{CH_2}$CH$_2$CH$_2$), 1.6 (m, 8H, -SiCH$_2$$\mathit{CH_2}CH_2$), 1.9 (m, 12H, -C(CH$_2$)$\mathit{CH_3}$), 4.1 (m, 8H, -SiCH$_2CH_2$$\mathit{CH_2}$), 5.6 (m, 4H, -C($\mathit{CH_2}$)CH$_3$), and 6.2 (m, 4H, -C($\mathit{CH_2}$)CH$_3$).

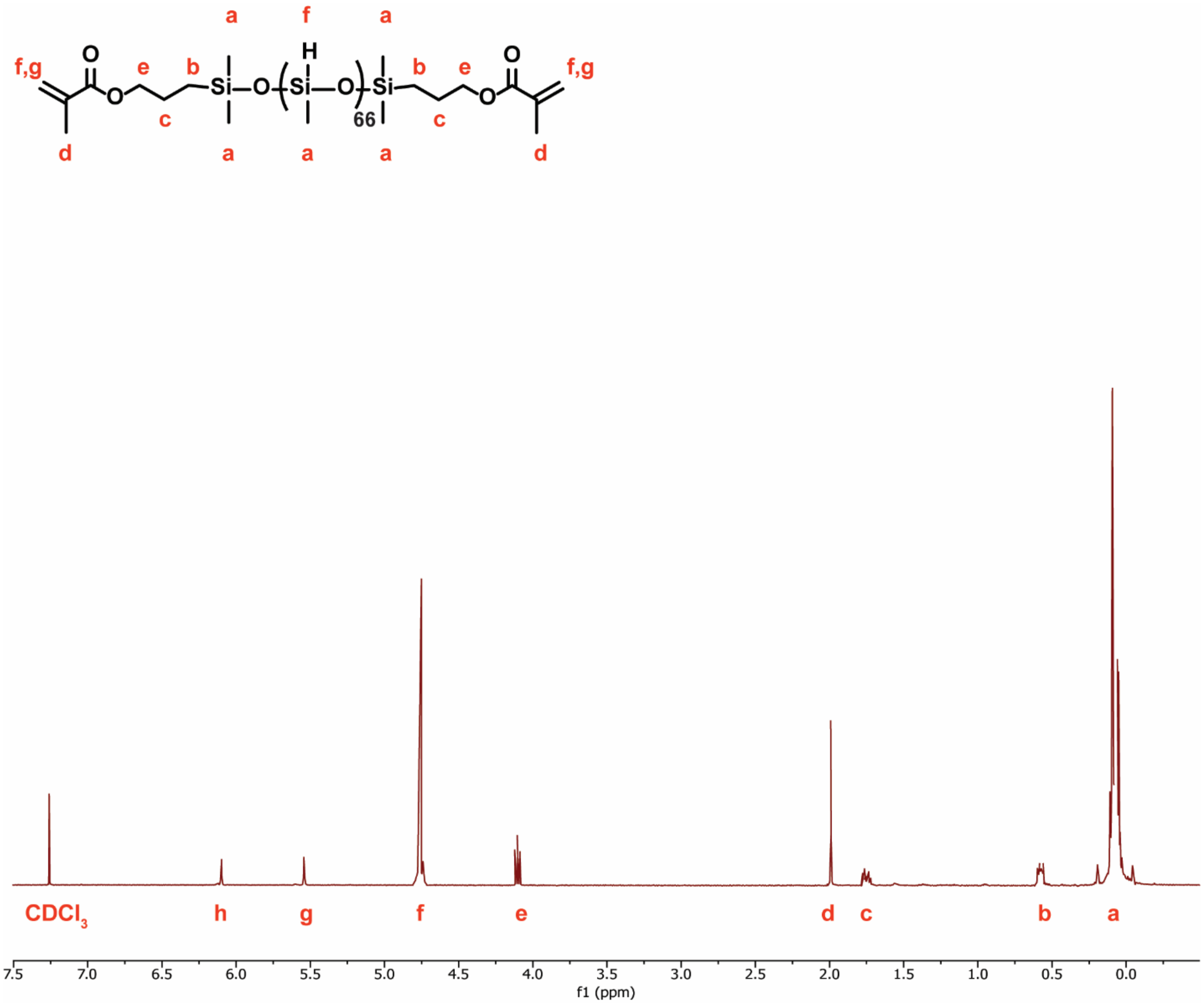

Figure B-5. NMR spectra for PMHS-DMA [n = 66; M_n = ~4587 g mol^{-1}]. ^{1}H NMR (MHz; δ, ppm): 0.14 (bm, 221H, $SiC\mathit{H_3}$), 0.6 (m, 4H, - $SiC\mathit{H_2}CH_2CH_2$), 1.7 (m, 4H, -$SiCH_2C\mathit{H_2}CH_2$), 2.0 (m, 6H, -$C(CH_2)(C\mathit{H_3})$), 4.1 (m, 4H, -$SiCH_2CH_2C\mathit{H_2}$), 4.7 (s, 67H, $Si\mathit{H}$), 5.5 (m, 2H, -$C(C\mathit{H_2})(CH_3)$, and 6.15 (m, 2H, -$C(C\mathit{H_2})(CH_3)$).